NATIONAL ADVISORY COMMITTEE FOR AERONAUTICS

TECHNICAL NOTE 4234

PRESSURE DISTRIBUTIONS AT TRANSONIC SPEEDS FOR PARABOLIC-ARC BODIES OF REVOLUTION HAVING FINENESS RATIOS OF 10, 12, AND 14

By Robert A. Taylor and John B. McDevitt

Ames Aeronautical Laboratory
Moffett Field, Calif.

Washington
March 1958

1T

NATIONAL ADVISORY COMMITTEE FOR AERONAUTICS

TECHNICAL NOTE 4234

PRESSURE DISTRIBUTIONS AT TRANSONIC SPEEDS FOR PARABOLIC-ARC BODIES OF REVOLUTION HAVING FINENESS RATIOS OF 10, 12, AND 14

By Robert A. Taylor and John B. McDevitt

SUMMARY

The measured static-pressure distributions at the model surfaces and in the surrounding flow field are presented for parabolic-arc bodies of revolution having fineness ratios of 10, 12, and 14. The data were obtained with the various bodies at zero angle of attack. The Mach number varied from 0.80 to 1.20, and Reynolds number varied from approximately 23.4×10^6 to 28.6×10^6 (based on the theoretical length of the model from nose to point of closure).

INTRODUCTION

The formulation of theoretical concepts with regard to transonic flow phenomena has advanced considerably in recent years. The validation, however, for any particular theoretical approach depends ultimately on a favorable comparison between theory and experiment. Experimental data also serve as an invaluable guide during the formulation of transonic flow theories.

In order to provide experimental data concerning the pressure distributions on and near bodies at transonic speeds, an experimental investigation has been initiated in the Ames 14-foot transonic wind tunnel. The present report describes the experimental pressure distributions at transonic speeds for parabolic-arc bodies of revolution having fineness ratios of 10, 12, and 14.

NOTATION

B blockage factor, the ratio of maximum body cross-sectional area to the tunnel cross-sectional area

C_D drag coefficient, $\frac{D}{q_\infty l^2}$

$C_{D_{bp}}$ base-pressure drag coefficient (see eq. (3))

C_{D_f} friction-drag coefficient

C_{D_p} pressure-drag coefficient, $C_{D_{sp}} + C_{D_{bp}}$

$C_{D_{sp}}$ surface-pressure drag coefficient (see eq. (2))

C_p pressure coefficient, $\frac{p - p_\infty}{q_\infty}$

D drag

d body diameter

f body fineness ratio, $\frac{l}{d_{max}}$

h tunnel half height

l body length, measured from nose to point of closure

M_∞ free-stream Mach number

p local static pressure

q_∞ free-stream dynamic pressure

Re Reynolds number based on body length

R body radius

$S(\xi)$ body cross-sectional area normalized by dividing by body length squared, $\pi H^2(\xi)$

u,v perturbation velocities normalized by dividing by the free-stream velocity

β $\sqrt{|M_\infty{}^2 - 1|}$

η,ξ,θ cylindrical coordinate system, see sketch (a), where η and ξ are radial and streamwise distances normalized by dividing by the body length

H	body radius normalized by dividing by the body length l, $\frac{R}{l}$
φ	perturbation velocity potential
$(\ )'$,$(\ )''$	first and second derivatives with respect to the normalized streamwise coordinate ξ

Subscripts

b	body base
max	maximum
∞	free-stream conditions

APPARATUS AND MODELS

Tunnel

This investigation was conducted in the Ames 14-foot transonic wind tunnel, which is a closed-return tunnel equipped with a perforated test section permitting continuous operation from subsonic to low supersonic speeds (fig. 1). Each wall of the test section contains 16 longitudinal slots with each slot containing a corrugated strip as indicated in figure 1. The ratio of accumulated slot widths (minus the accumulated widths of the corrugated inserts) to tunnel perimeter in a plane normal to the air stream is equal to 0.054 (usually referred to as the porosity factor).

Models

The bodies considered in this investigation are parabolic-arc bodies of revolution having fineness ratios of 10, 12, and 14. The fineness ratio is defined as the ratio of body length (from nose to point of closure) to maximum body diameter. The radii of the parabolic-arc bodies are given by the equation

$$H = 4H_{max}(\xi-\xi^2)$$

and the coordinate system used is indicated in sketch (a).

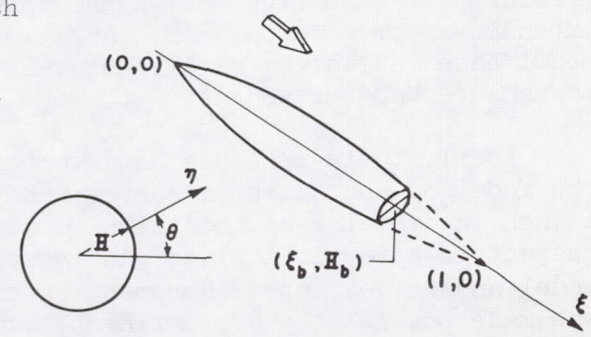

Sketch (a)

The maximum body diameter d_{max}, body length l, the ratio of l^2 to wetted area W, and blockage factor B are tabulated below.

Body fineness ratio, f	d_{max}, in.	l, in.	l^2/W	B
10	8	80	5.06	0.19
12	6	72	6.07	.10
14	6	84	7.07	.10

All of the bodies were truncated (at $\xi_b = 0.854$) to permit mounting on the sting (see fig. 2). The base areas in all cases were equal to 25 percent of the respective maximum cross-sectional areas.

The variations of normalized (with respect to body length) body radius H, and body slope H', are presented in figures 3(a) and 3(b). The variations of the normalized cross-sectional area, S, and the first and second derivatives are shown in figures 3(c), 3(d), and 3(e).

In addition to the three bodies described above, a larger body of fineness ratio 14 (maximum diameter of 8 in. and length equal to 112 in.) was also tested. The experimental data for this body were found to be seriously affected by tunnel-wall interference effects. These data are included in this report (see Appendix) since it is believed they might be useful in future studies involving wall interference effects.

Instrumentation

The axial force was measured by a strain-gage balance enclosed within the model. Multiple-tube manometers using tetrabromoethane (specific gravity = 2.96) were photographed to record the pressure data.

Body pressure data were obtained by the use of two rows of static-pressure orifices (located on the upper and lower surface of the models) extending from nose to base. Additional orifices were located at the model base and in the cavity between the body and sting support in order to measure base pressures.

Local static-pressure data were obtained in the flow field surrounding the model by the use of a survey tube, see figure 4. The survey tube was 1 inch in diameter and contained static-pressure orifices located 90° with respect to a vertical plane passing through the longitudinal axes of the model and survey tube. Movement of the survey tube during model testing was made possible by supporting the survey tube at the model support strut

normally used for changing model angle of attack. Arrangement was also provided for the vertical movement of the tension cable in order that the survey tube would always be horizontal.

TESTS AND PROCEDURE

The models were tested at zero angle of attack through a Mach number range from 0.80 to 1.20. Reynolds number varied from 23.4×10^6 to 28.6×10^6 (based on model length and average recorded temperatures); see figure 5. To promote transition near the model nose, No. 60 Carborundum grits were cemented over the first inch of each model.

The experimental data were not corrected for tunnel-wall interference effects. Considerations of the testing procedure and the data-reduction process indicate that the free-stream Mach numbers are repeatable within approximately ±0.002, the angle of attack is accurate within approximately ±0.1, and the pressure-coefficient data are repeatable within approximately ±0.005.

The force and pressure data were obtained simultaneously and reduced to standard coefficient form. The drag coefficient is defined by the following relationship

$$C_D = \frac{D}{q_\infty l^2} = C_{D_{sp}} + C_{D_{bp}} + C_{D_f} \tag{1}$$

where the component parts are defined as

$$C_{D_{sp}} = \int_0^{\xi_b} C_p S'(\xi)d\xi \tag{2}$$

$$C_{D_{bp}} = -C_{p_b} S_b \tag{3}$$

$$C_{D_f} = \frac{D_f}{q_\infty l^2} \tag{4}$$

and thus equation (1) can be expressed as

$$\frac{D}{q_\infty l^2} = \int_0^{\xi_b} C_p S'(\xi)d\xi - C_{p_b} S_b + \frac{D_f}{q_\infty l^2} \tag{5}$$

The drag may be calculated by the use of measured pressure distributions. The pressure drag of the body, $C_{D_{sp}}$, may be obtained by graphical integration of the variation of $C_p S'(\xi)$ with ξ. The base drag, $C_{D_{bp}}$, is

equal to the product of the base area and a measured pressure coefficient at the base (the base pressure coefficient is assumed to be constant across the base). The skin-friction coefficient, C_{D_f}, may be estimated from the theory of Van Driest for the turbulent flow over a flat plate (ref. 1).

TUNNEL-WALL INTERFERENCE

The experimental data in this report have not been corrected for tunnel-wall interference effects. The use of a perforated test section, of course, tends to alleviate wall interference effects but interference-free data cannot be expected at transonic speeds unless the model size relative to the tunnel size is extremely small. During the course of the present investigation, it was found that the experimental data for one of the bodies (see Appendix of this report) provided some information regarding the effect of model size on wall interference.

Tunnel-wall interference effects in general depend on model geometry, on the relative size of the model with respect to the tunnel size, and on the type of tunnel wall used. Wall interference effects at subsonic speeds are discussed in reference 2 where it is shown that the blockage correction is directly proportional to the ratio of model volume to h^3 where h is the tunnel radius. For bodies of revolution this ratio is proportional to the parameter $(l/h)^3/f^2$, where f is the fineness ratio and l, the body length.

At supersonic speeds the bow wave is reflected from the tunnel walls (although reduced considerably in strength for porous walls) and creates an interference if the wave impinges on the model. The range of slightly supersonic Mach numbers for which the reflected bow wave may be of appreciable strength and impinge on the model can be made small by keeping the ratio l/h small. This type of interference ends when the supersonic speed is increased to the point where the reflected wave is swept downstream of the body.

In reference 3 Berndt considers the transonic flows about geometrically similar bodies and finds that, for a given model and wind tunnel, if the interference effects are small and acceptable, then the length of a geometrically similar model must decrease as the slenderness is increased. In other words, if the interference is not to increase when a more slender body is tested, the quantity $f(l/h)$ should not be increased.

In the present tests the longest model tested (see Appendix) was also one of the most slender (fineness ratio 14) and the tunnel-wall interference was found to be excessive. It should be noted that simple considerations of tunnel blockage would not explain this result since the blockage

ratio B, defined as the ratio of model cross-sectional area to the tunnel cross-sectional area, was exactly the same as that for the fineness-ratio-10 model which had much smaller interference effects.

Sketch (b) has been prepared to illustrate the variations between f and l/h according to the relationships $f(l/h)$ = constant and $B = \frac{\pi}{16}\frac{(l/h)^2}{f^2}$. In this case, h is the half-height of the test section for the Ames 14-foot transonic wind tunnel. The open symbols represent the three bodies described in the main text of this report. The solid symbol represents the longest body of fineness ratio 14 (length equal to 112 in.) which was also tested and for which the experimental data at transonic speeds were found to be seriously affected by tunnel-wall interference.

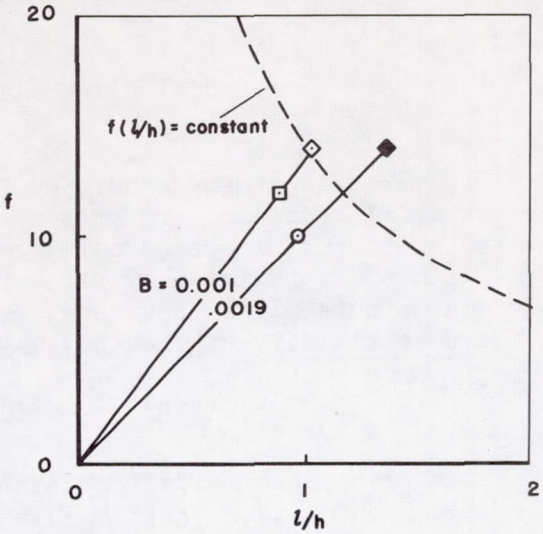

Sketch (b)

It is apparent that simple considerations of tunnel blockage are not adequate to explain wall interference effects at transonic speeds. For smooth bodies of revolution, the length of the model relative to the tunnel height appears to be important.

DATA PRESENTATION

The data presented in this report consist of axial forces, body pressures, and field pressures with the models at zero angle of attack. The force and pressure data are presented in separate sections. Additional surface-pressure data for parabolic-arc bodies having fineness ratios of 6 and $6\sqrt{2}$ may be obtained from reference 4.

Pressure Data

Surface-pressure distributions, accompanied by the flow field pressure surveys, are presented in figures 6 through 8. The data symbols for the body surface pressures in figure 6 are an average of the pressure readings on the upper and lower body surfaces (the upper and lower orifices were located at identical axial stations for this model). In figures 7 and 8 the circles represent the upper surface and the squares the lower surface. The triangular data points represent measured base pressures. It is believed that the data points near $\xi = 0.6$ at $M = 1.05$ for all three

models and near $\xi = 0.7$ at $M = 1.075$ for the fineness-ratio-10 and -14 models are influenced by the reflected bow wave. Although considerable scatter is evident in portions of the pressure data, smooth curves have been faired through the data points.

Radial Attenuation of Pressures

The variations of pressure coefficient with radial distance η for various axial locations are presented in figures 9 to 11. It is of considerable interest to compare the radial attenuation of pressure coefficient with that predicted by slender-body theory. According to slender-body concepts (see, for instance, refs. 5 to 7) the perturbation potential in the near vicinity of the body may be expressed in the form

$$4\pi\varphi(\xi,\eta) = 2S'(\xi)\ln \eta + g(\xi;\ M_\infty) \tag{6}$$

where the prime denotes differentiation with respect to the axial coordinate ξ. The function $g(\xi;\ M_\infty)$ is known for subsonic or supersonic flows but is difficult to determine at transonic speeds, although a recent theoretical approach by Oswatitsch (ref. 7) appears promising. In any event, the pressure coefficient is related to the velocity perturbations approximately as

$$C_p \approx -2u - v^2 \tag{7}$$

and if equation (6) is differentiated to obtain the perturbation velocities, the pressure coefficient of slender-body theory may be written as

$$C_p = -\frac{S''(\xi)\ln \eta}{\pi} - \frac{[S'(\xi)]^2}{4\pi^2\eta^2} - \frac{g'(\xi;\ M_\infty)}{2\pi} \tag{8}$$

or

$$C_p + F(\xi,\eta) = -\frac{g'(\xi;\ M_\infty)}{2\pi} \tag{9}$$

where

$$F(\xi,\eta) = \frac{S''(\xi)\ln \eta}{\pi} + \frac{[S'(\xi)]^2}{4\pi^2\eta^2}$$

For a given axial station ξ and Mach number M_∞ the left-hand side of equation (9) remains constant for all values of η for which the slender-body concept (eq. (8)) holds.

The experimental data of this report will now be examined in view of equation (9). In figures 12 to 14 variations of the experimentally determined quantity $C_p + F(\xi,\eta)$ with radial distance η are presented for various axial stations. It appears that the quantity $C_p + F(\xi,\eta)$ is essentially invariant throughout the radial distance for which experimental data were obtained (from body surface to a radial distance equal to four times the maximum body diameter).

An alternative method for comparing the experimental results with slender-body concepts is obtained by plotting the quantity $C_p + v^2$ versus $\ln \eta$. In this case C_p is known from experiment but v must be approximated by use of the slender-body result (obtained by differentiation of eq. (6) with respect to η). However, the slender-body result for v is exact, within the framework of small-disturbance theory, at the body surface and attenuates rapidly with η so that the slender-body result for v is either sufficiently accurate or negligible in comparison with C_p. In figure 15 the experimentally determined values for $C_p + [S'(\xi)]^2/4\pi^2\eta^2$ are plotted versus η with a logarithmic horizontal scale. In order for the experimental data to agree with slender-body concepts the data must fall along straight lines with slope equal to $-S''(\xi)/\pi$. Dashed lines having slopes equal to $-S''(\xi)/\pi$ are included in figure 15 for convenience in analyzing the data (the vertical locations of the dashed lines are not important).

The experimental data presented in figure 15 indicate a remarkably good agreement with slender-body concepts, especially for free-stream Mach numbers near 1. It is evident that the slender-body concept extends to larger values of η than that for which data were obtained for free-stream Mach numbers near 1. However, at the lowest Mach number tested ($M_\infty = 0.8$) good agreement with the slender-body concept appears to be confined to η values less than about four times the maximum body diameters.

Drag Data

The measured drag coefficients, adjusted to represent free-stream static pressure at the model base, and the measured base drag are presented in figure 16 for the various test Mach numbers. Also presented in figure 16 are the computed quantities $C_{D_f} + C_{D_{sp}}$; see equations (2) and (4). Typical variations of $C_pS'(\xi)$, required for the numerical evaluation of equation (2), are presented in figure 17.

Ames Aeronautical Laboratory
National Advisory Committee for Aeronautics
Moffett Field, Calif., Nov. 26, 1957

APPENDIX

ADDITIONAL PRESSURE DISTRIBUTIONS

As previously mentioned a large body of fineness ratio 14 (a theoretical length from nose to point of closure equal to 112 in.) was also tested but the experimental data were found to be seriously affected by tunnel-wall interference phenomena. However, it is believed that these data might be useful in future studies involving the evaluation of wall interference effects and consequently these data are included in figure 18.

REFERENCES

1. Lee, Dorothy B., and Faget, Maxime A.: Charts Adapted from Van Driest's Turbulent Flat-Plate Theory for Determining Values of Turbulent Aerodynamic Friction and Heat-Transfer Coefficients. NACA TN 3811, 1956.

2. Baldwin, Barrett S.,Jr., Turner, John B., and Knechtel, Earl D.: Wall Interference in Wind Tunnels With Slotted and Porous Boundaries at Subsonic Speeds. NACA TN 3176, 1954.

3. Berndt, Sune B.: Theoretical Aspects of the Calibration of Transonic Test Sections. Flygtekniska Försöksanstalten Report 74, 1957. (Supersedes FFA Rapp. AE-400)

4. Drougge, Georg: Some Measurements on Bodies of Revolution at Transonic Speeds. Int. Cong. Appl. Mech., Brussels, 1956.

5. Adams, Mac. C., and Sears, W. R.: Slender-Body Theory-Review and Extension. Jour. Aero. Sci., vol. 20, no. 2, Feb. 1953, pp. 85-98.

6. Heaslet, Max. A., and Spreiter, John R.: Three-Dimensional Transonic Flow Theory Applied to Slender Wings and Bodies. NACA TN 3717, 1956.

7. Oswatitsch, K., and Keune, F.: The Flow Around Bodies of Revolution at Mach Number 1. Proc. Conf. on High-Speed Aeronautics, Polytechnic Institute of Brooklyn, Brooklyn, N.Y., Jan. 20-22, 1955, pp. 113-131.

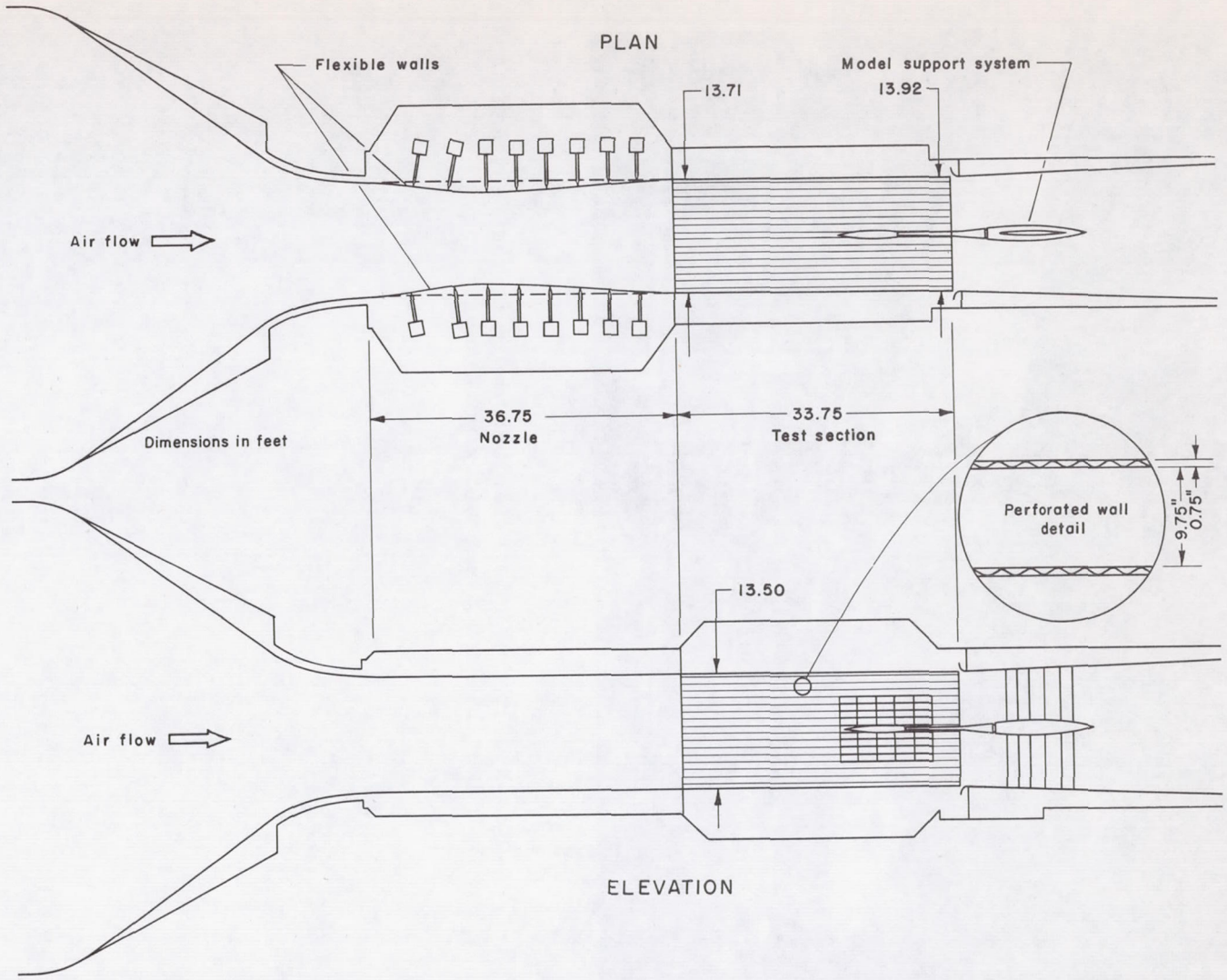

Figure 1.- General arrangement of the test section of the Ames 14-foot transonic wind tunnel.

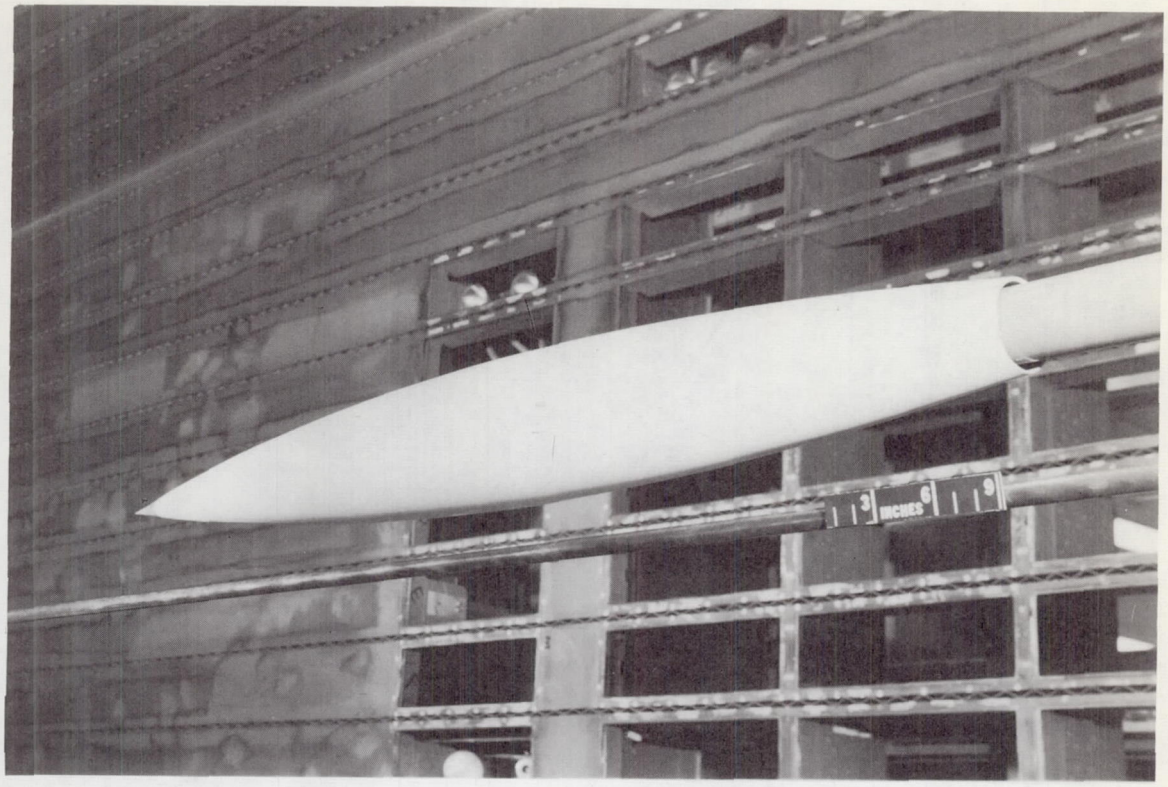

A-21864

Figure 2.- Photograph of the fineness-ratio-10 body in the test section of Ames 14-foot transonic wind tunnel.

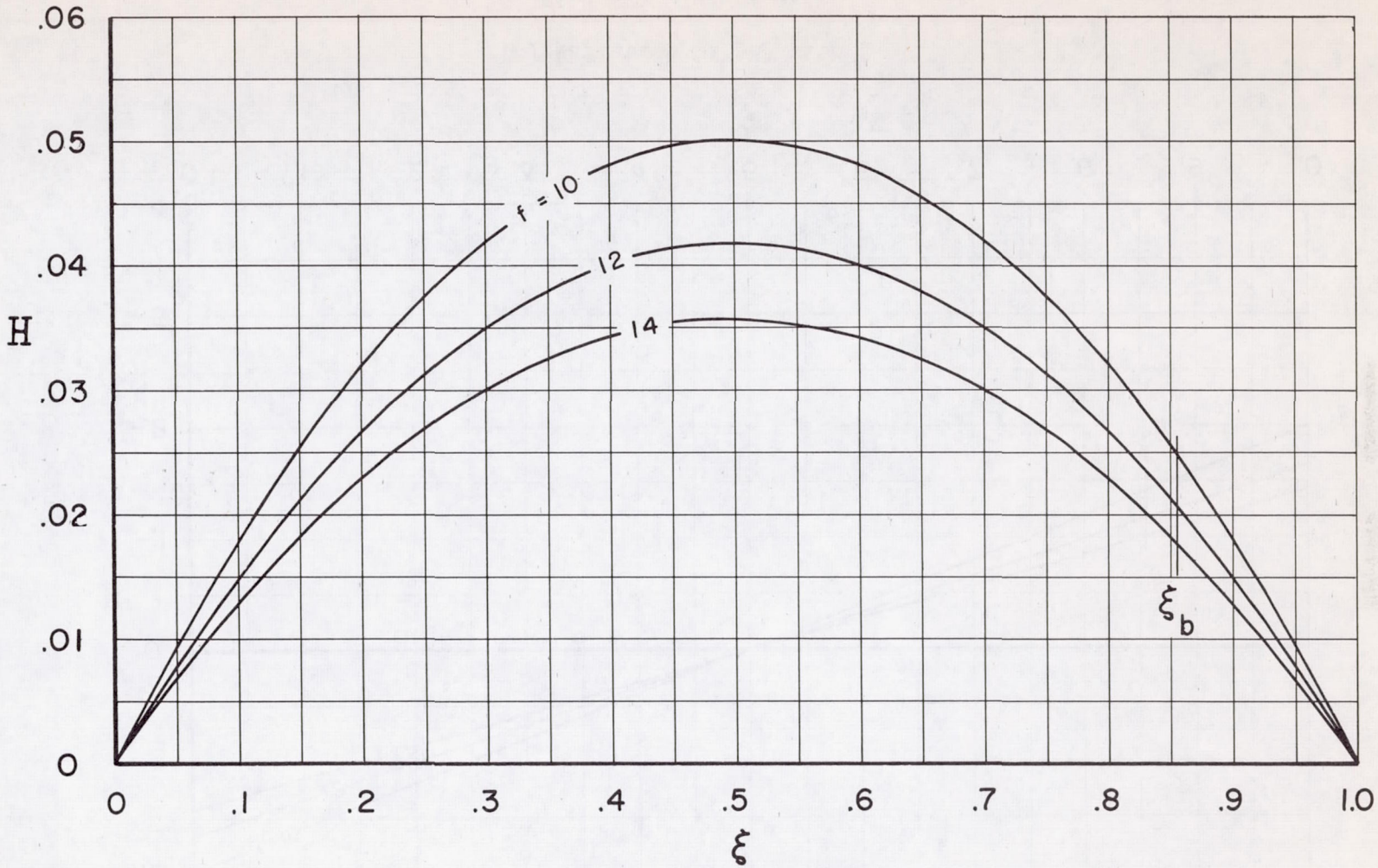

(a) Variation of H with ξ.

Figure 3.- Model geometry.

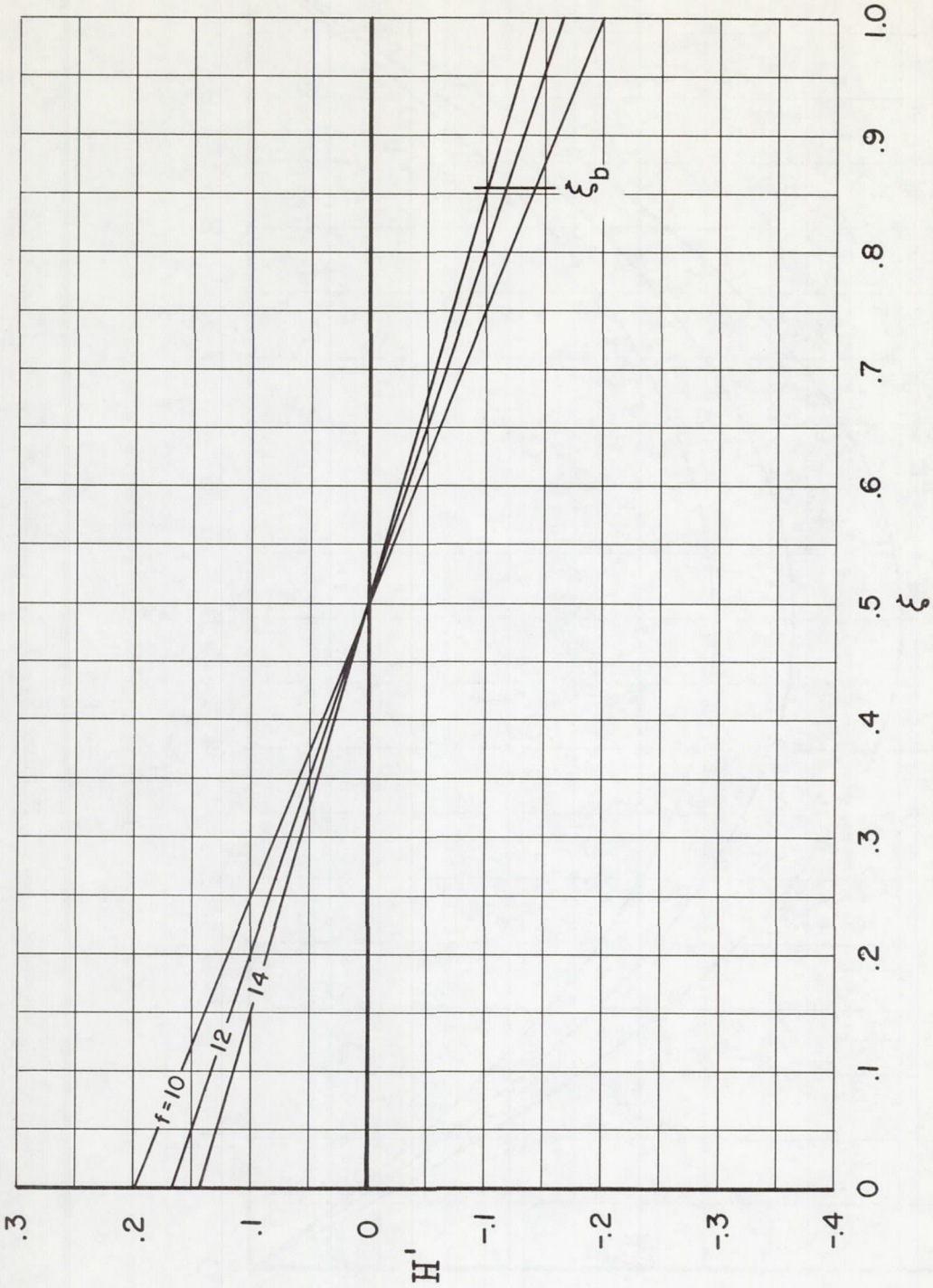

(b) Variation of H' with ξ.

Figure 3.- Continued.

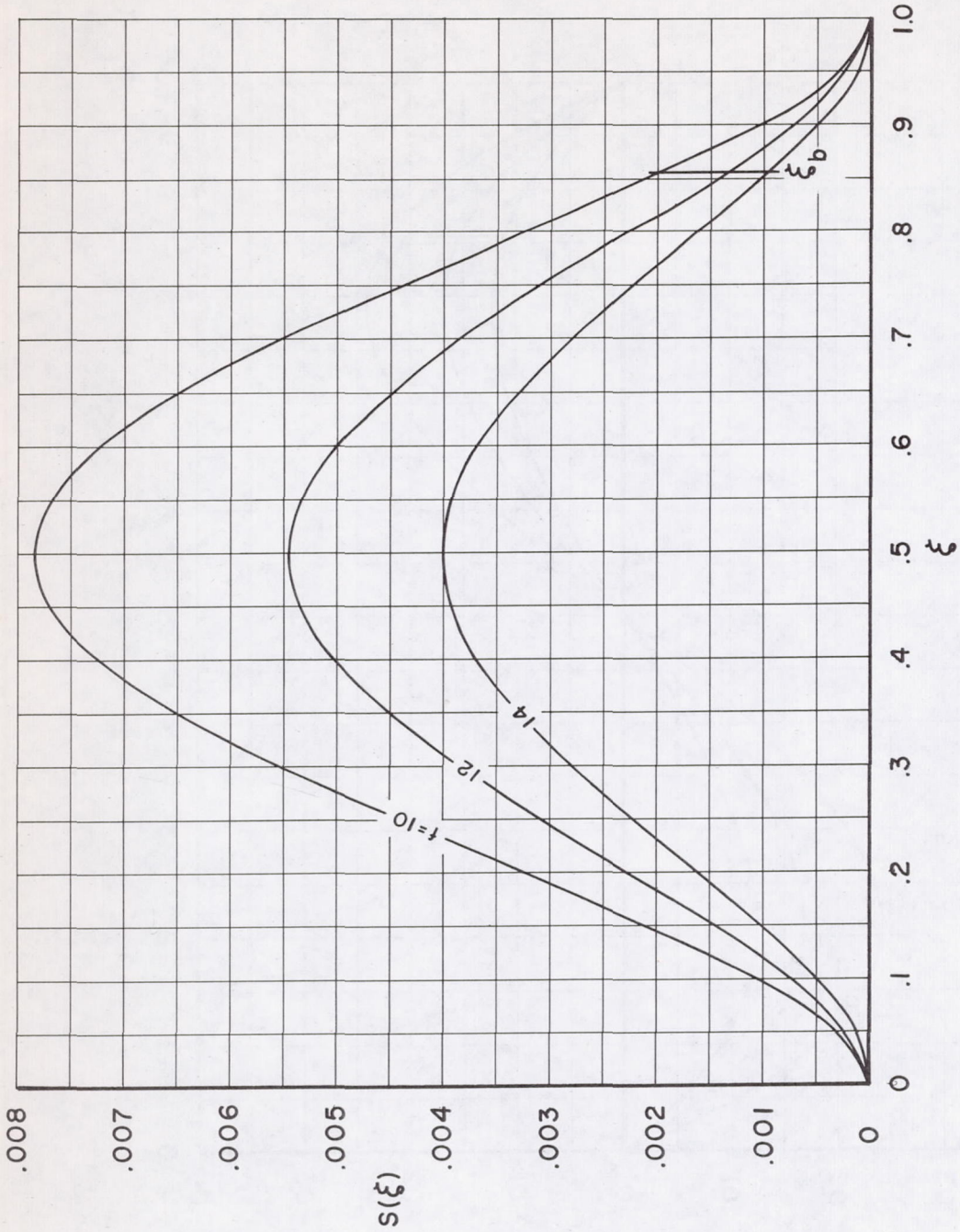

(c) Variation of S with ξ.

Figure 3.- Continued.

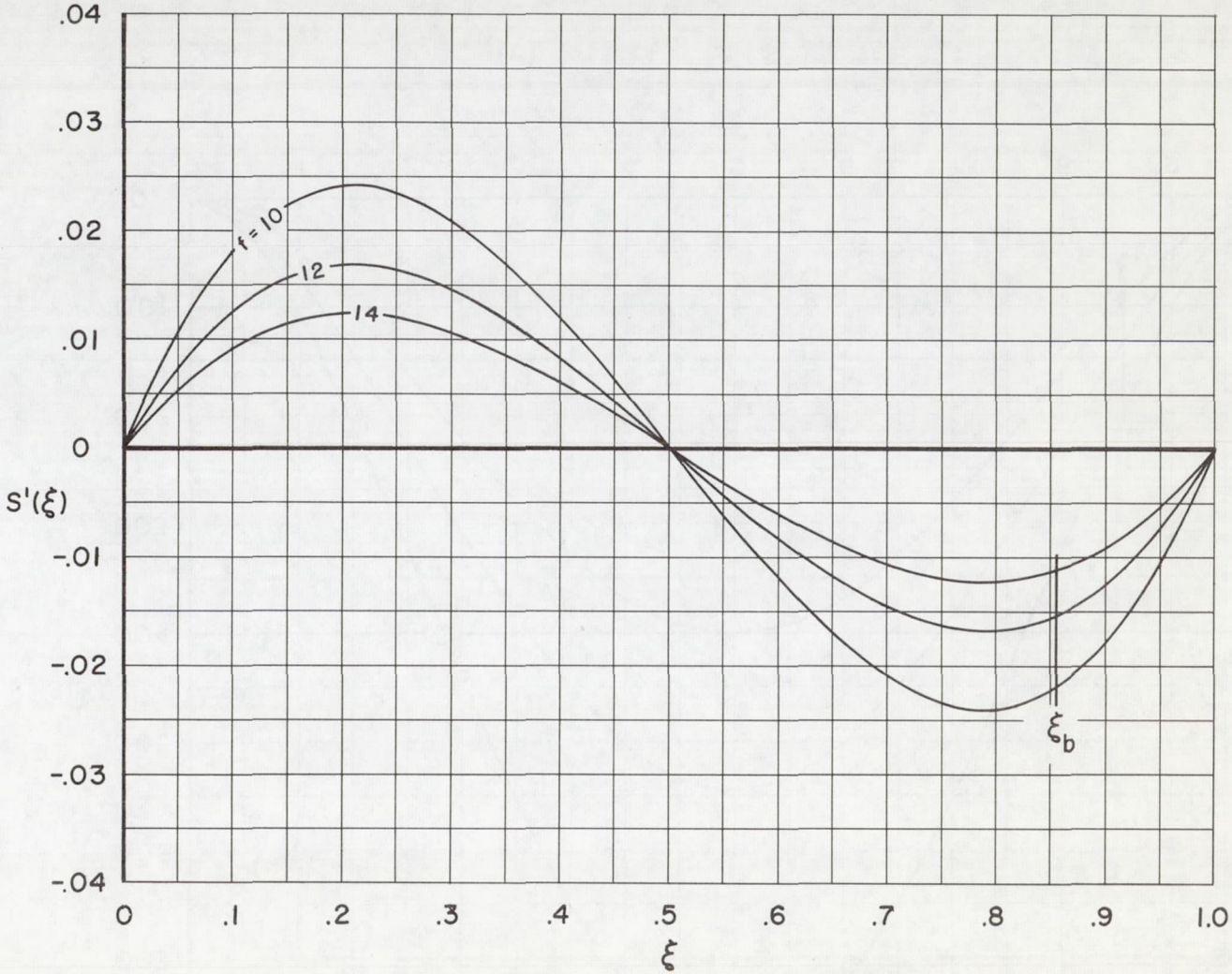

(d) Variation of S' with ξ.

Figure 3.- Continued.

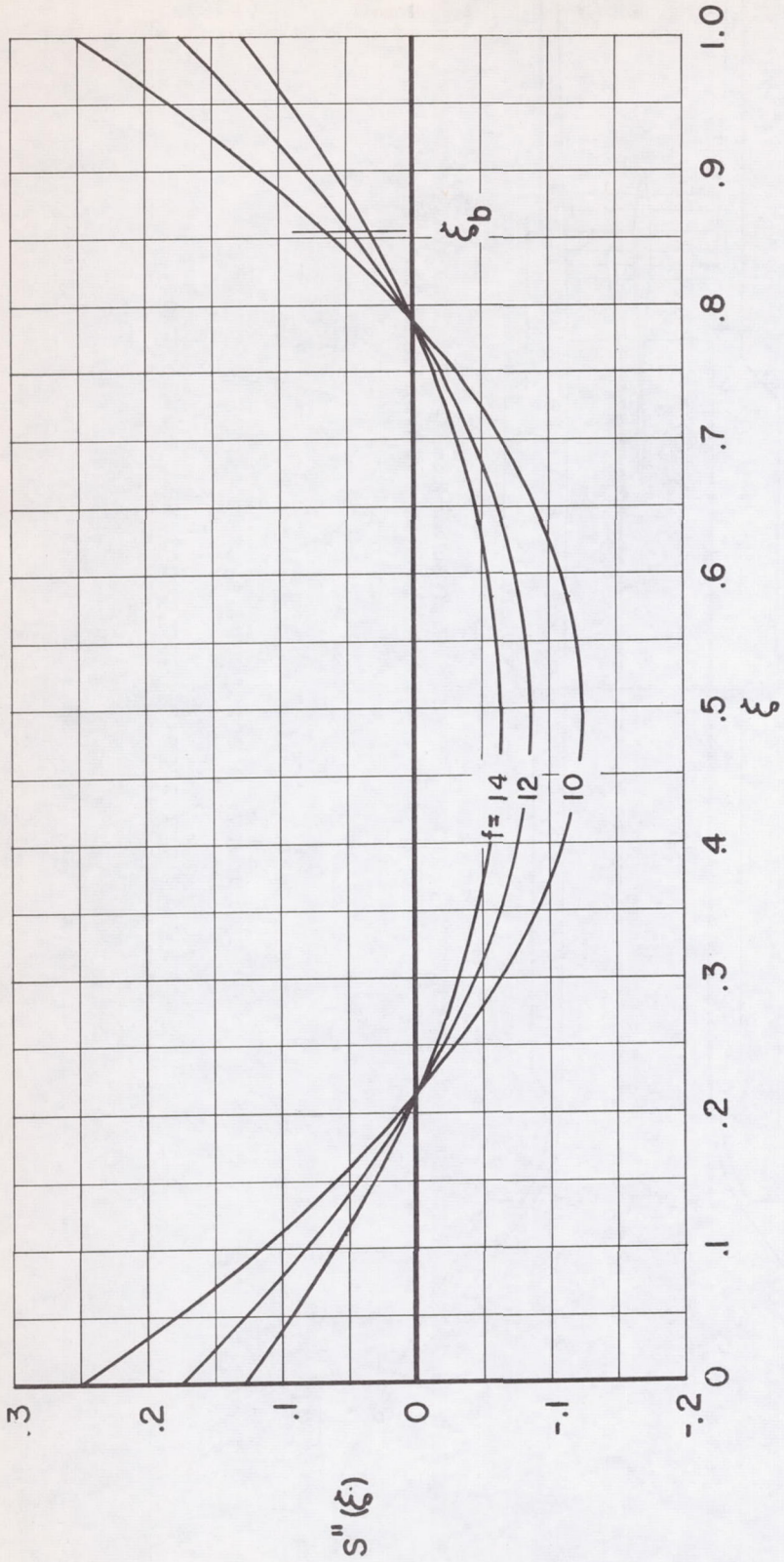

(e) Variation of S'' with ξ.

Figure 3.- Concluded.

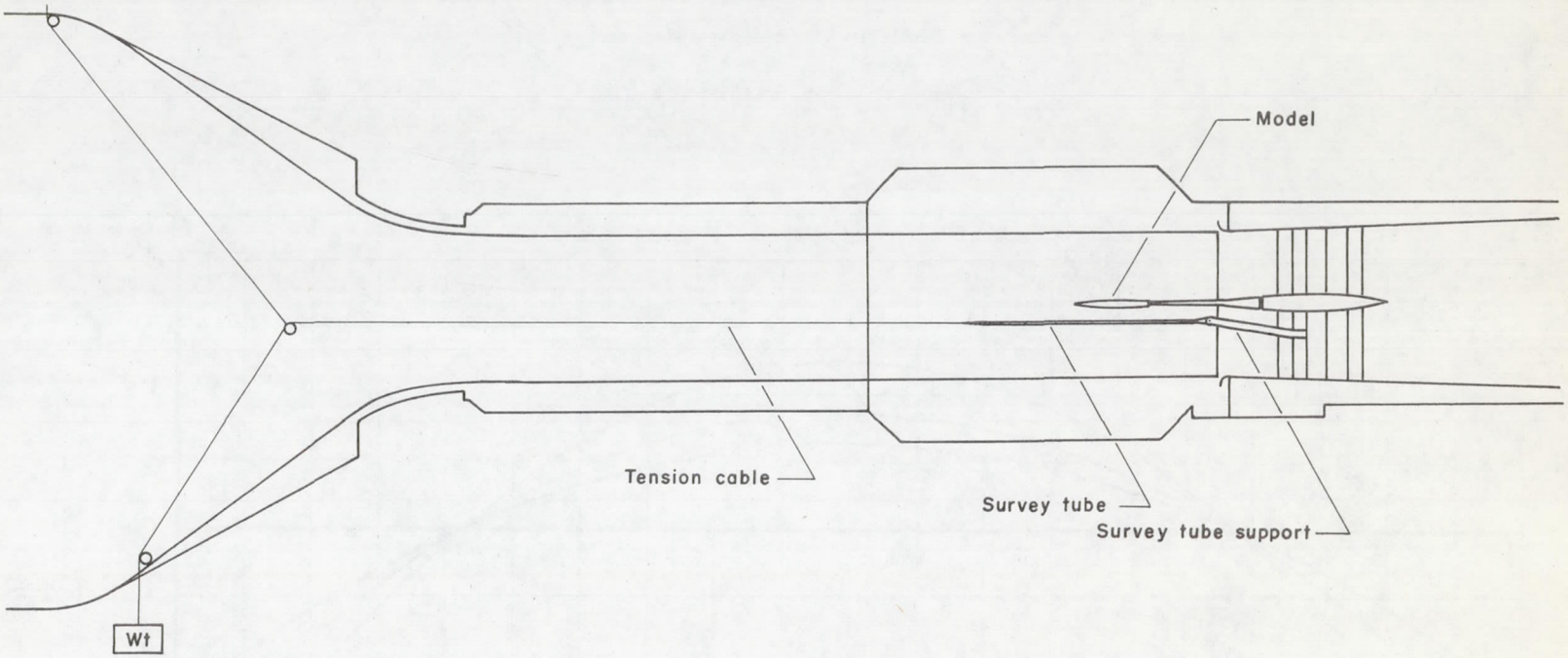

(a) Survey tube support system.

Figure 4.- Schematic drawings of the model and survey tube.

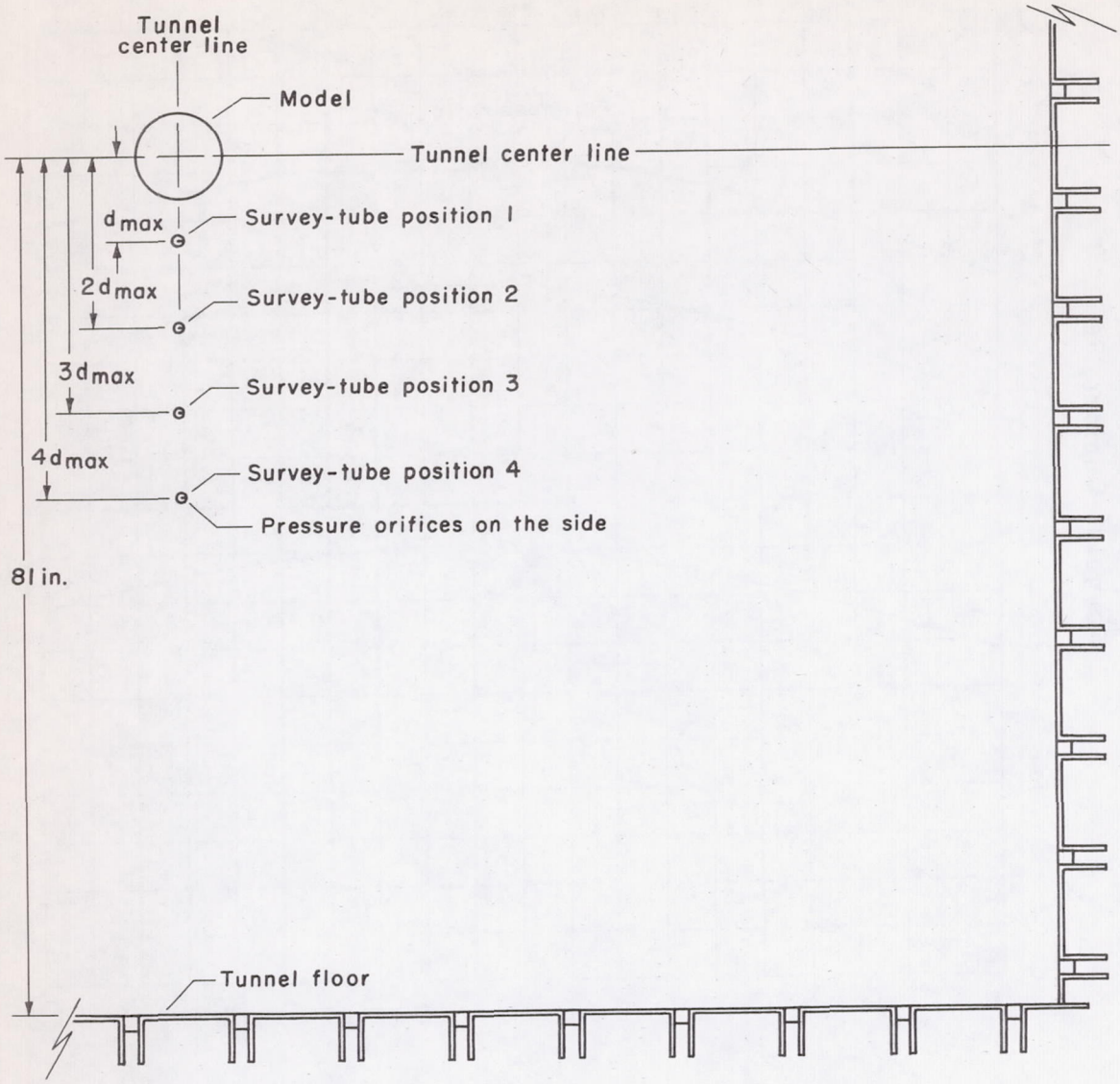

(b) Relative positions of the survey tube with respect to the model.

Figure 4.- Concluded.

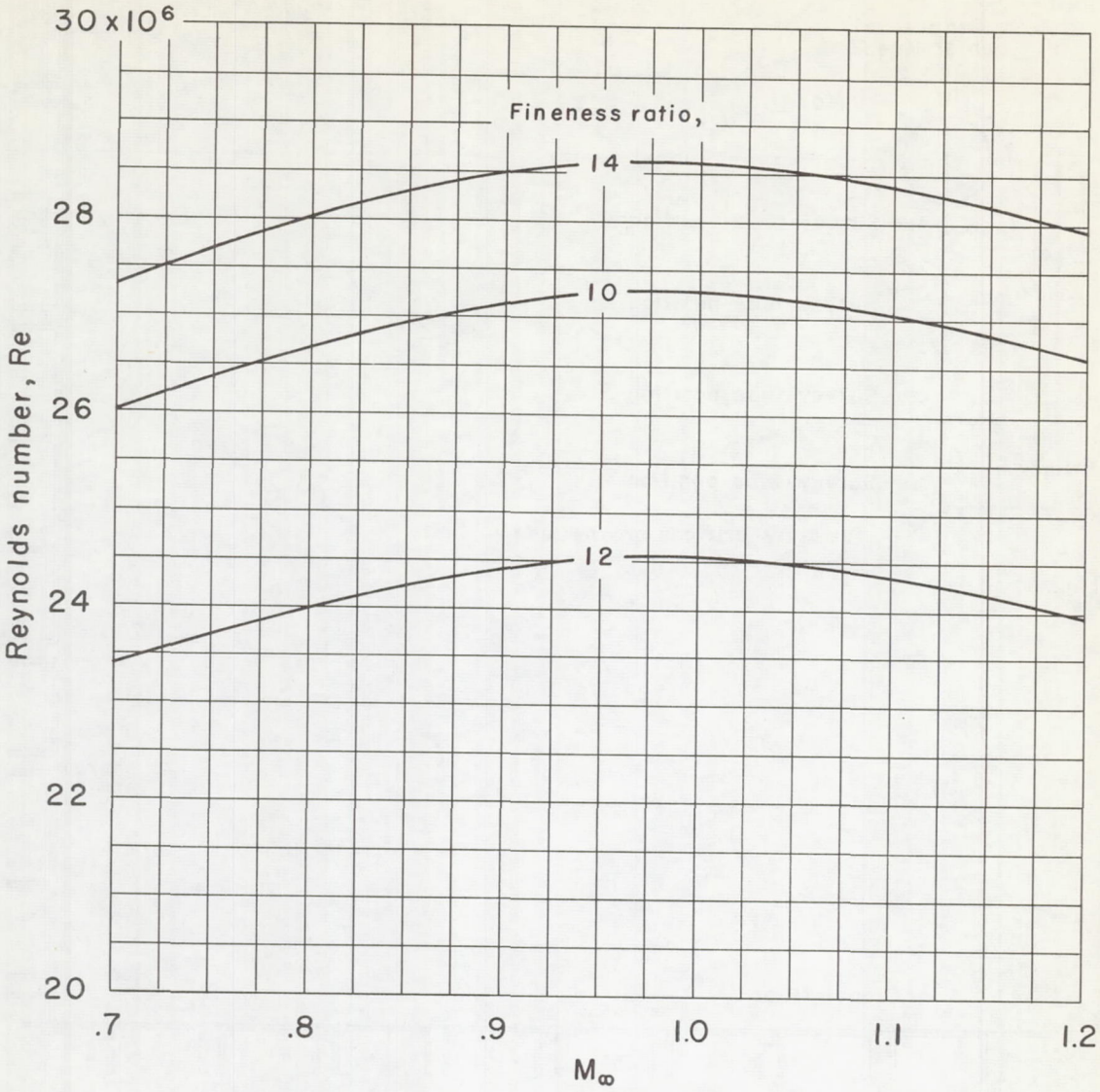

Figure 5.- Variation of Reynolds number with Mach number based on average temperatures.

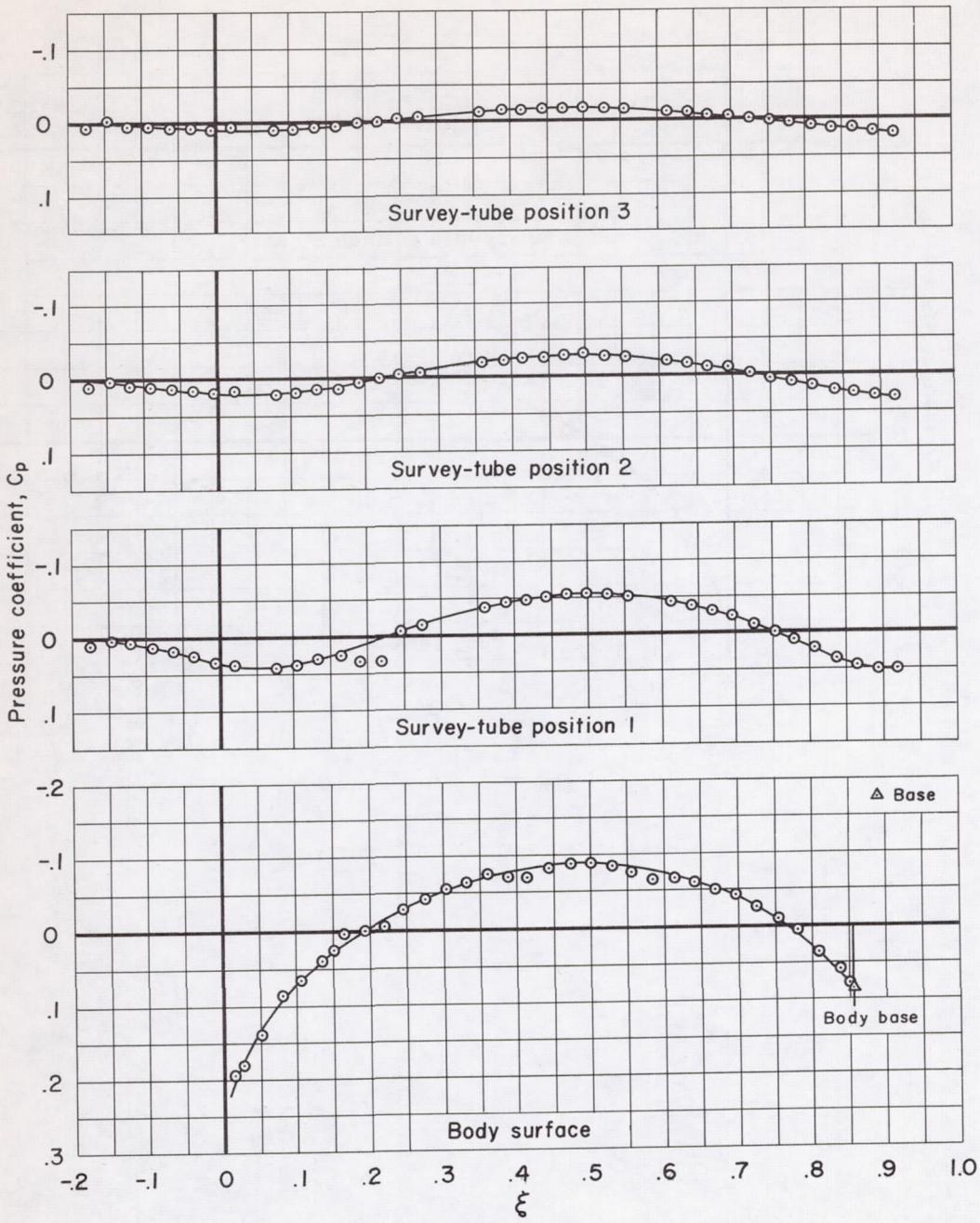

(a) $M_\infty = 0.80$, f = 10

Figure 6.- Measured pressure distributions for the body having a fineness ratio of 10.

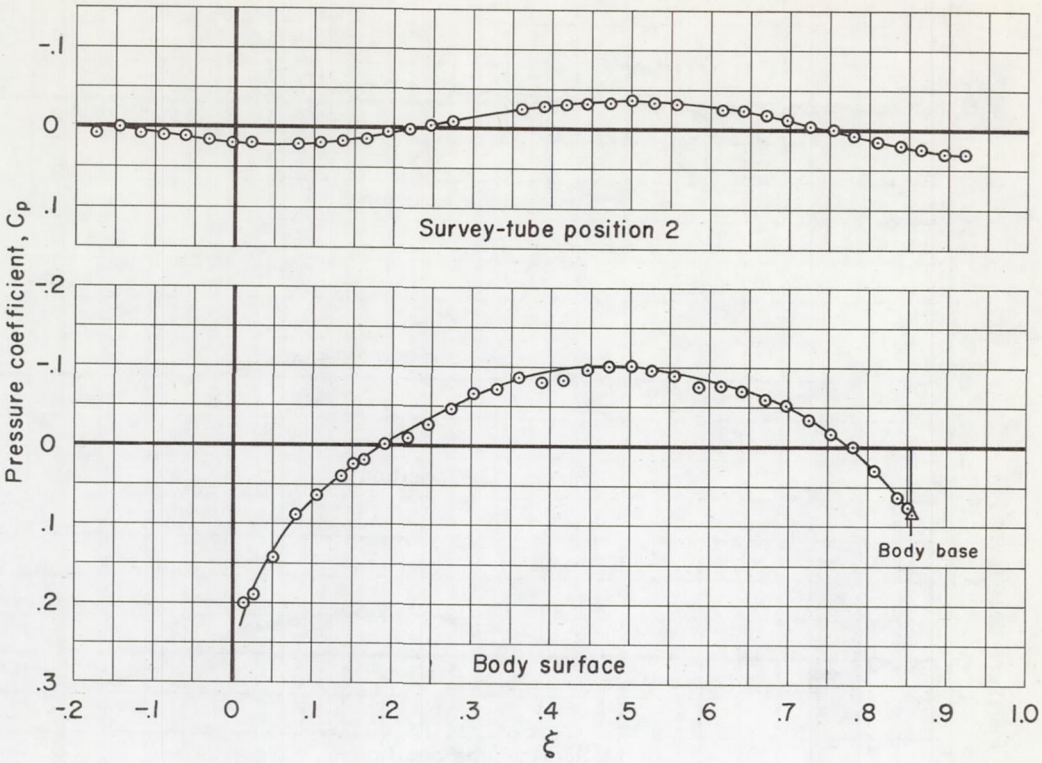

(b) $M_\infty = 0.85$, $f = 10$

Figure 6.- Continued.

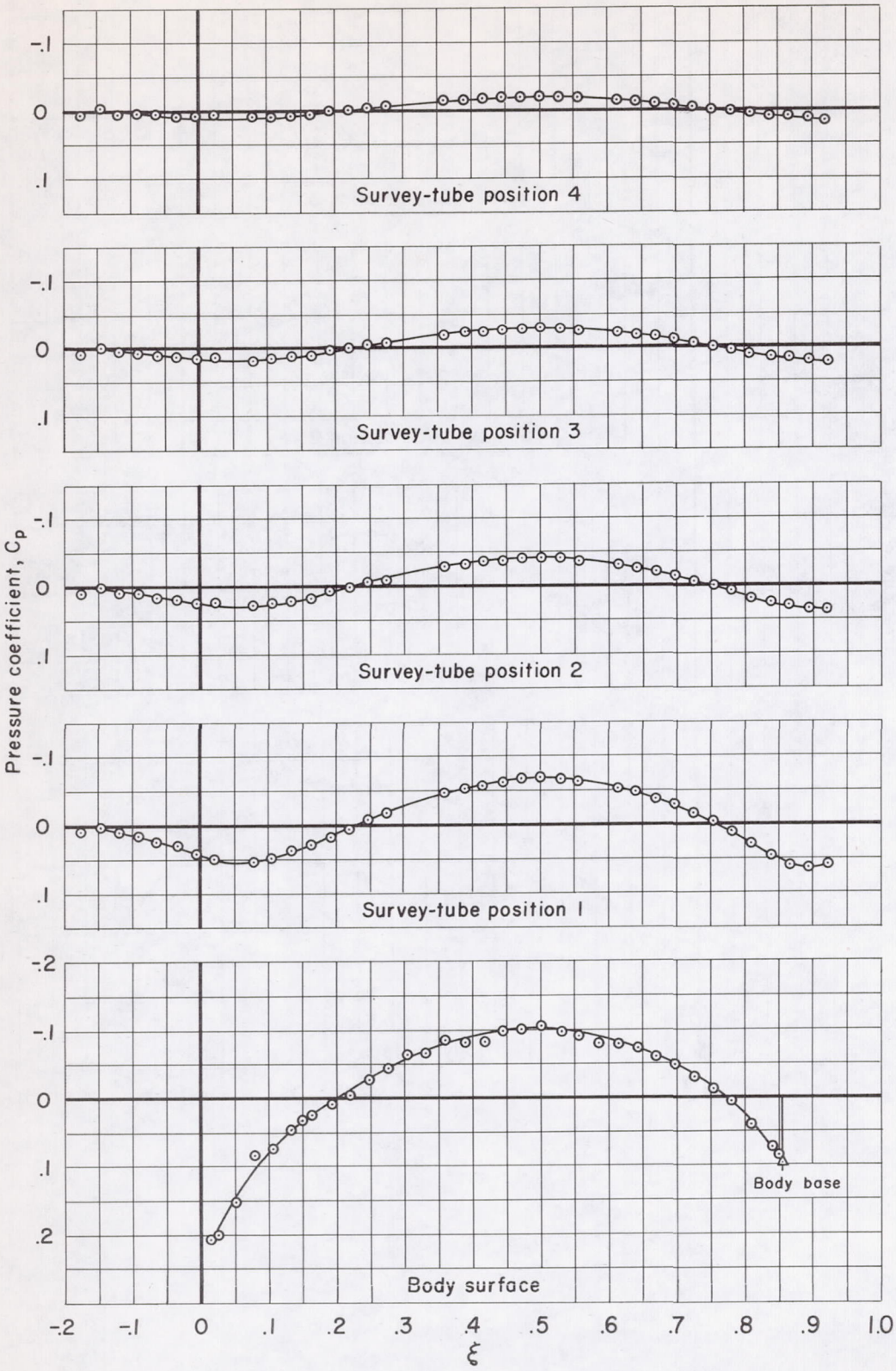

(c) $M_\infty = 0.90$, f = 10

Figure 6.- Continued.

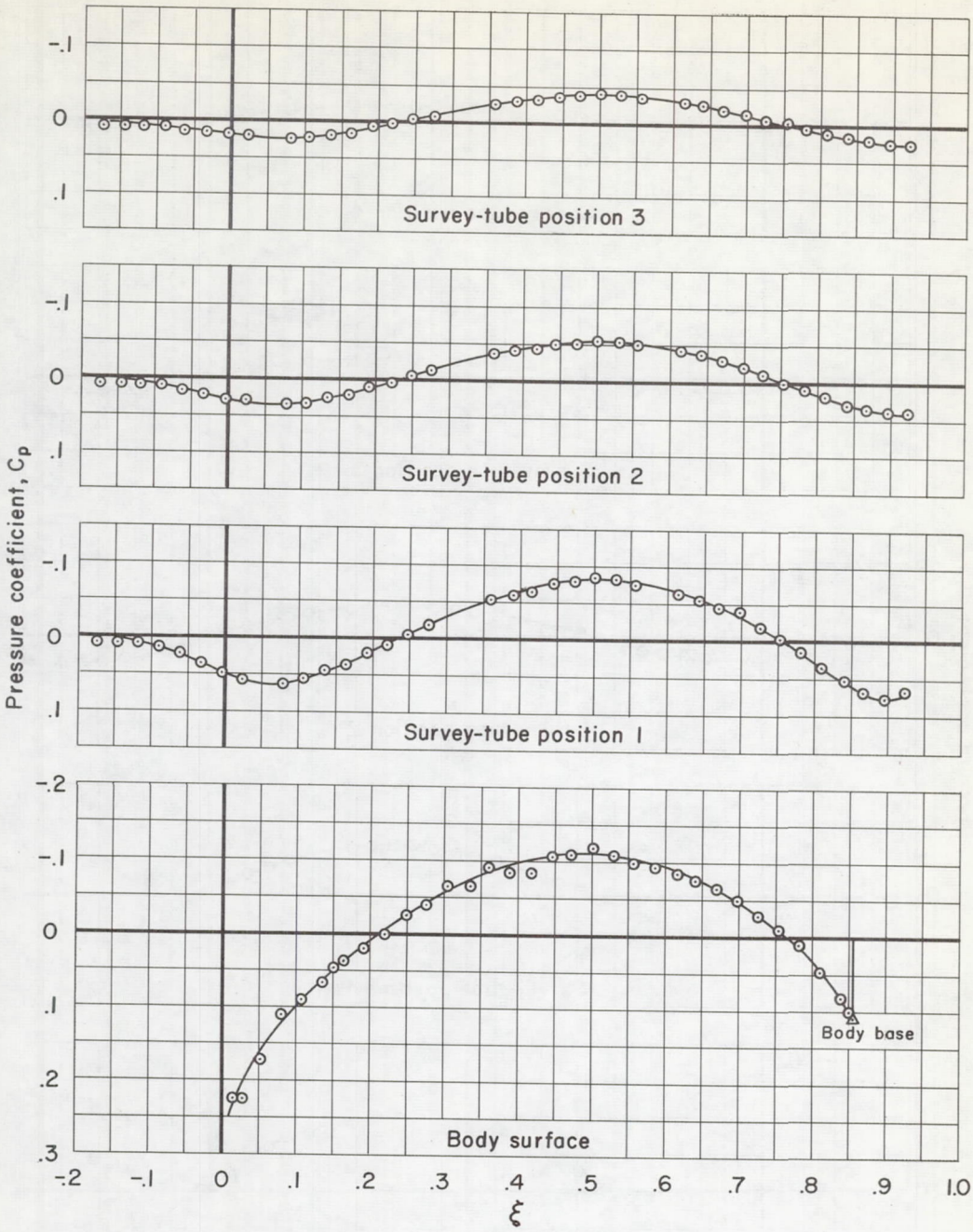

(d) $M_\infty = 0.95$, $f = 10$

Figure 6.- Continued.

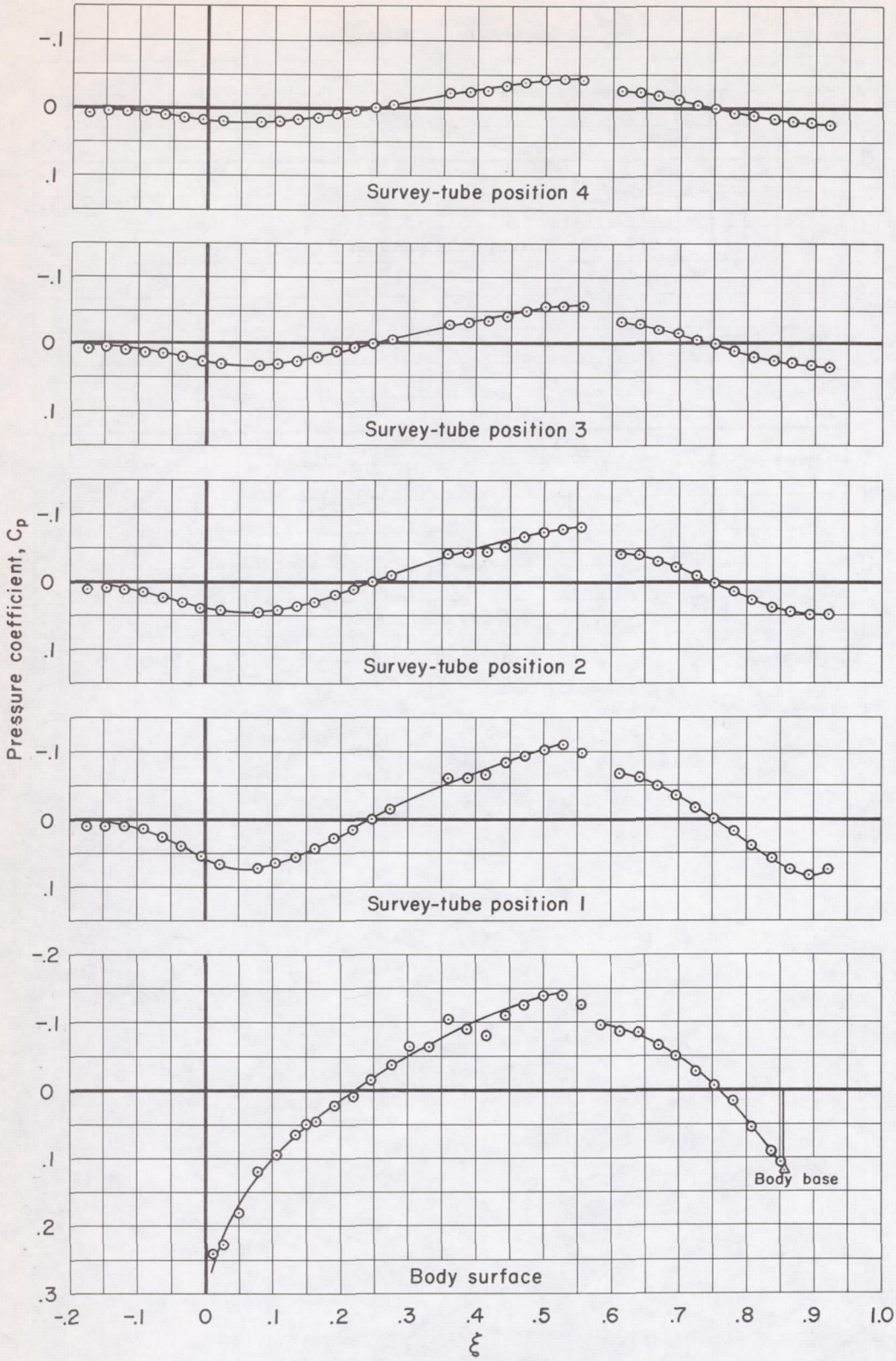

(e) $M_\infty = 0.975$, $f = 10$

Figure 6.- Continued.

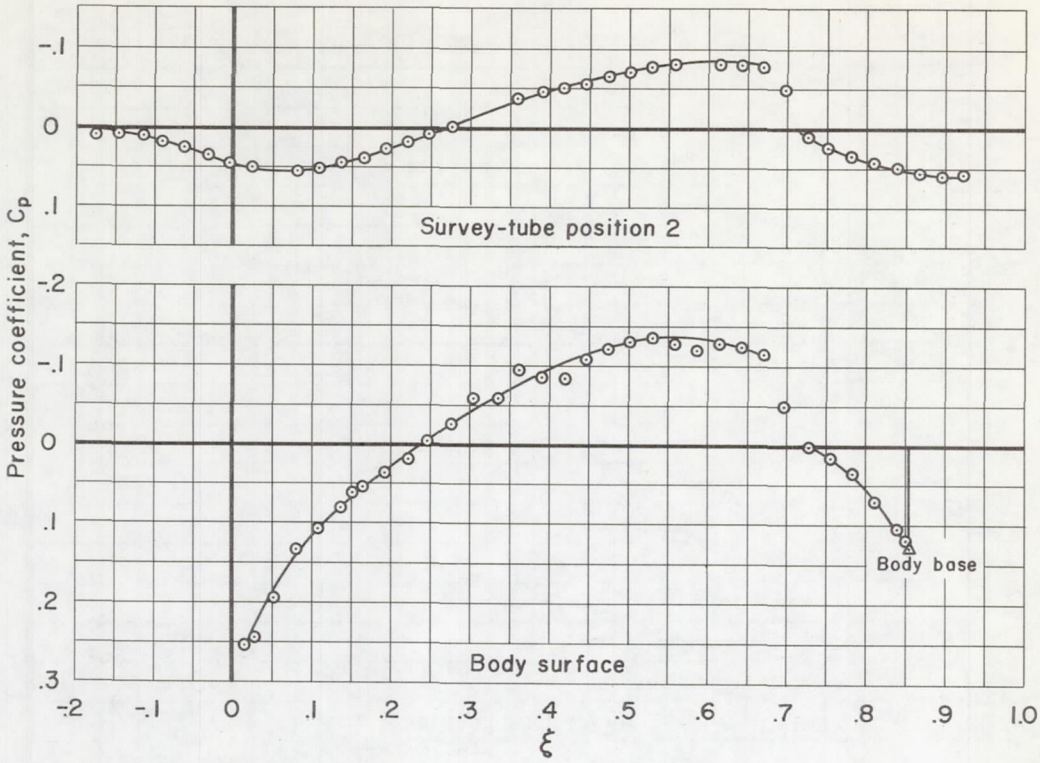

(f) $M_\infty = 0.99$, $f = 10$

Figure 6.- Continued.

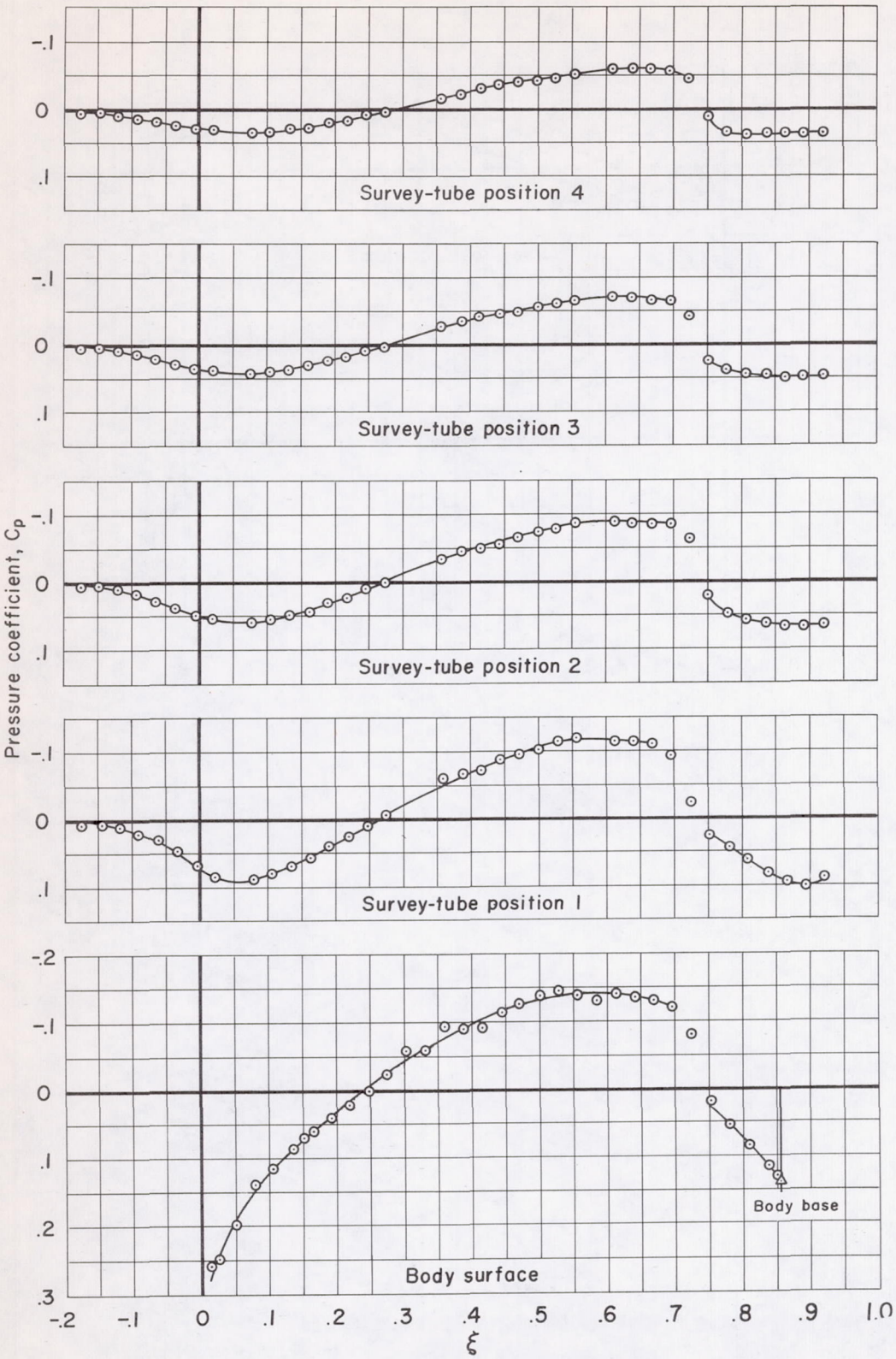

(g) $M_\infty = 1.0$, $f = 10$

Figure 6.- Continued.

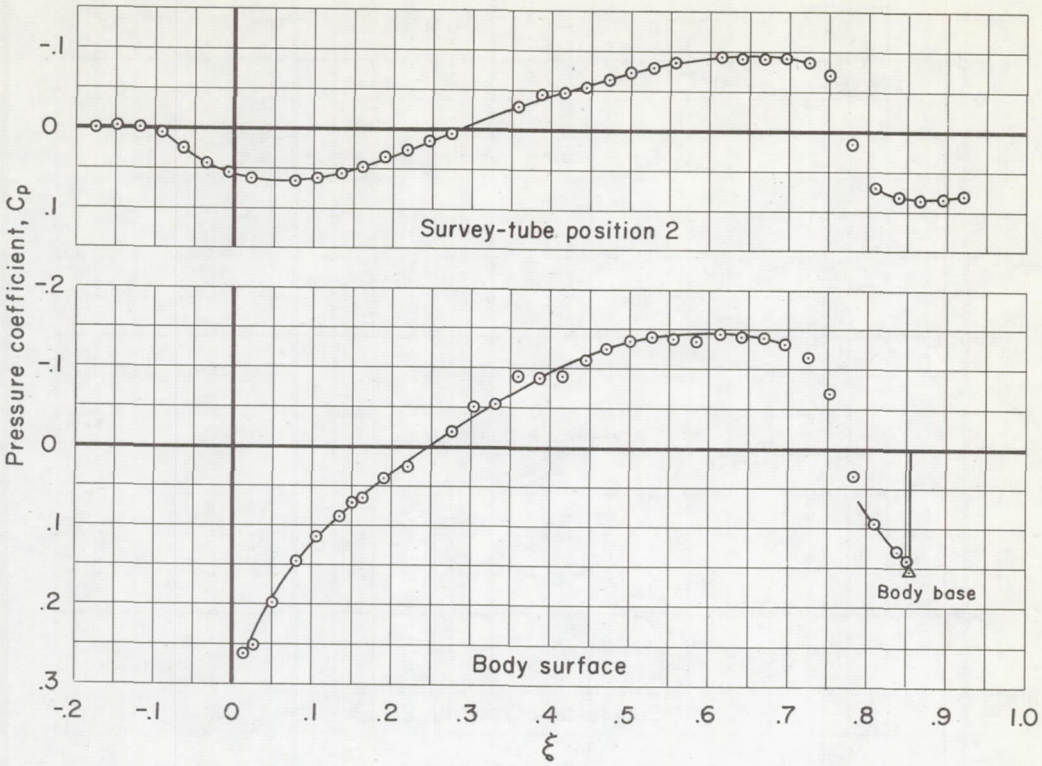

(h) $M_\infty = 1.01$, $f = 10$

Figure 6.- Continued.

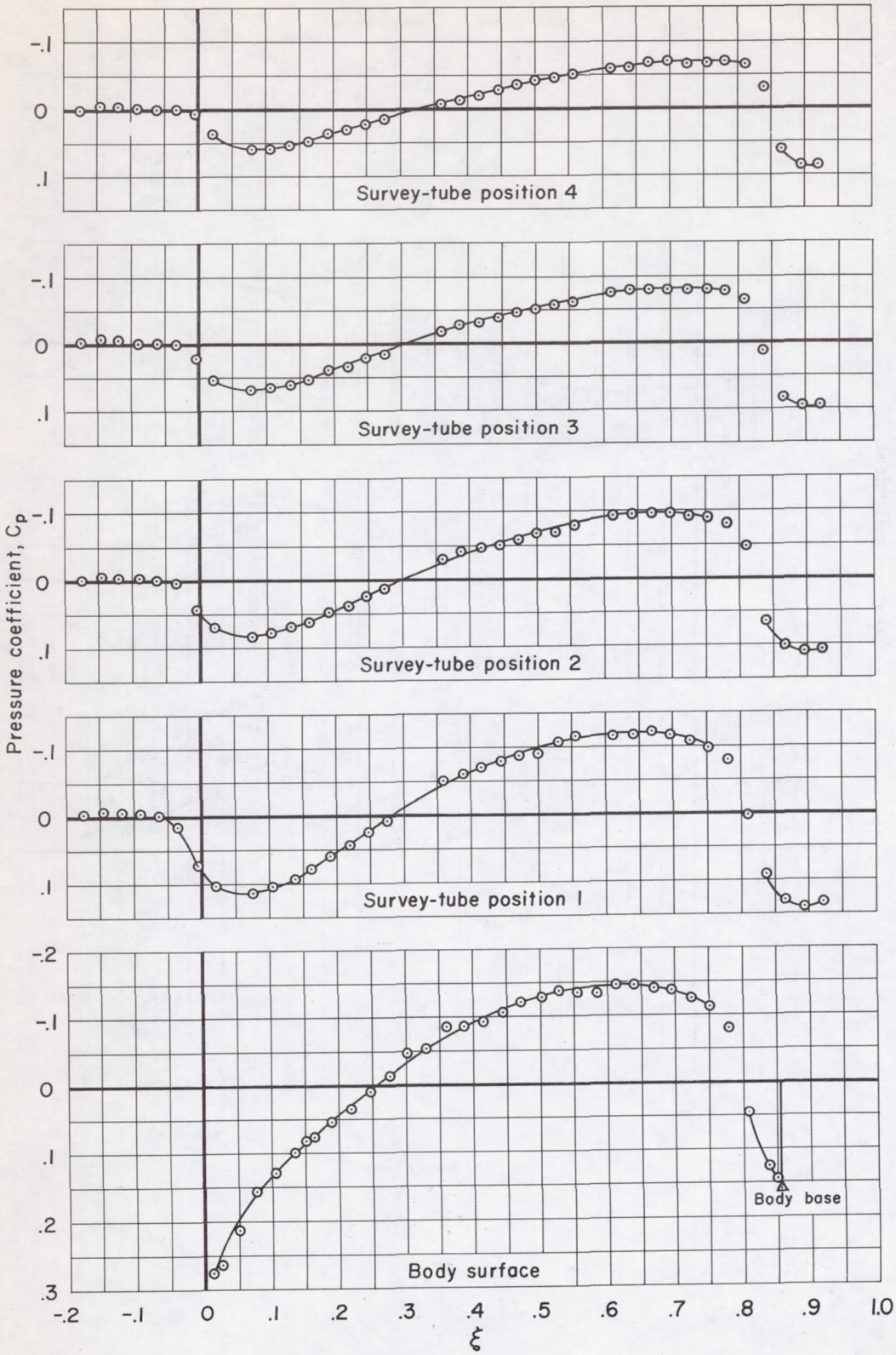

(i) $M_\infty = 1.025$, $f = 10$

Figure 6.- Continued.

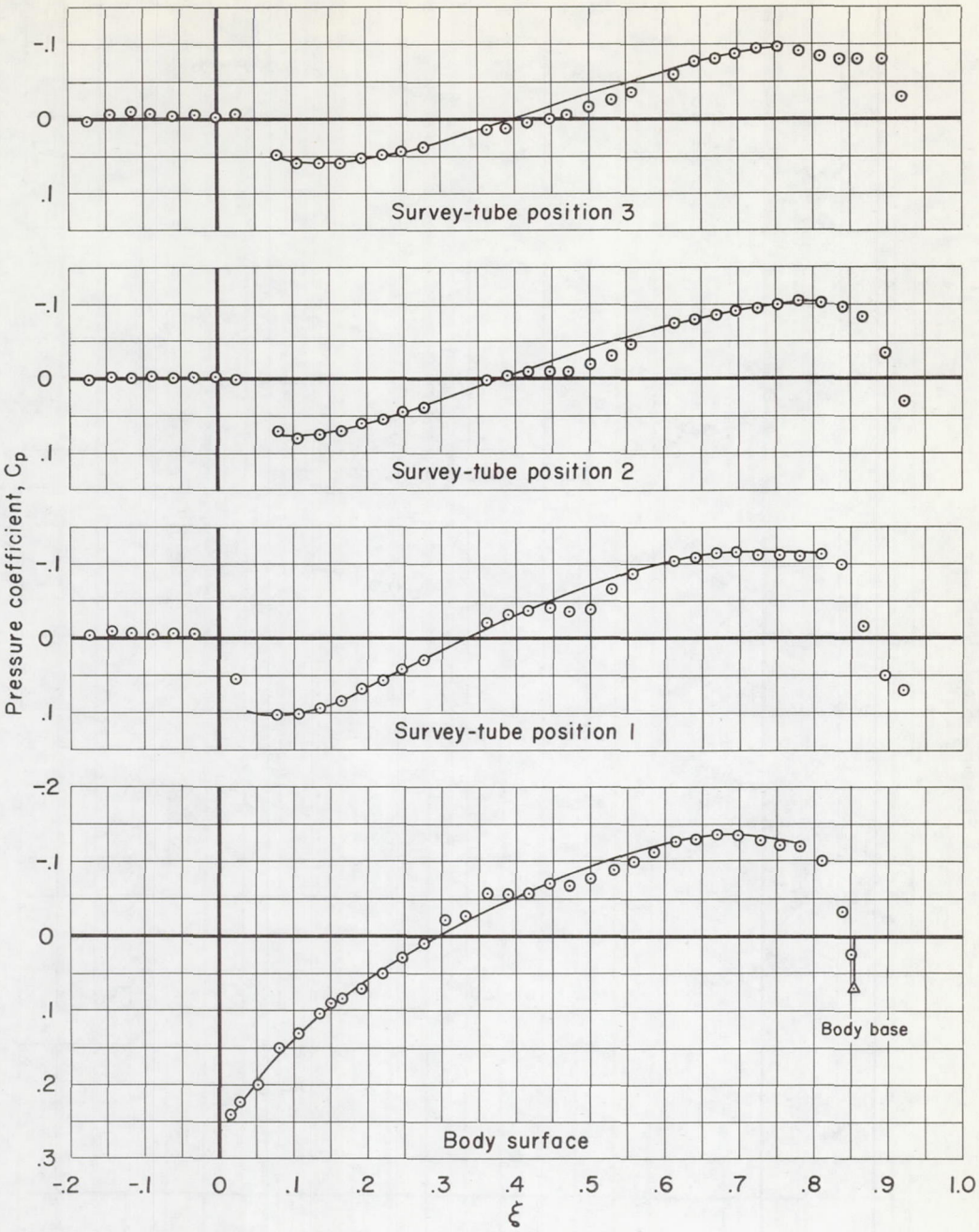

(j) $M_\infty = 1.05$, $f = 10$

Figure 6.- Continued.

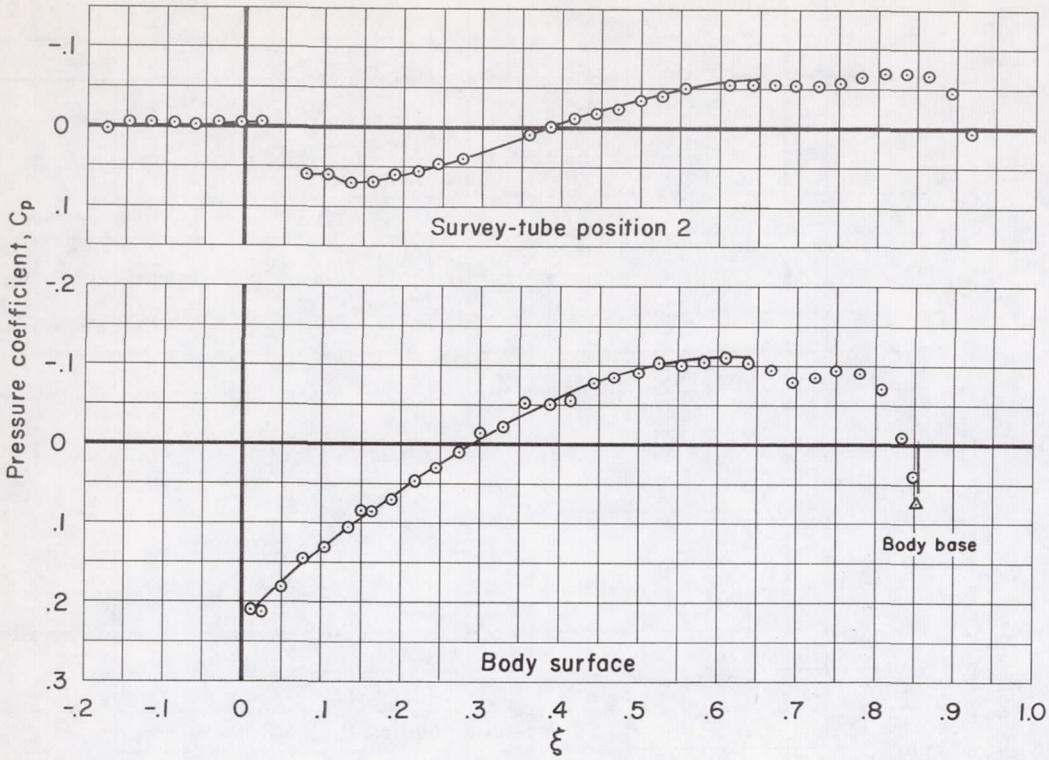

(k) $M_\infty = 1.075$, $f = 10$

Figure 6.- Continued.

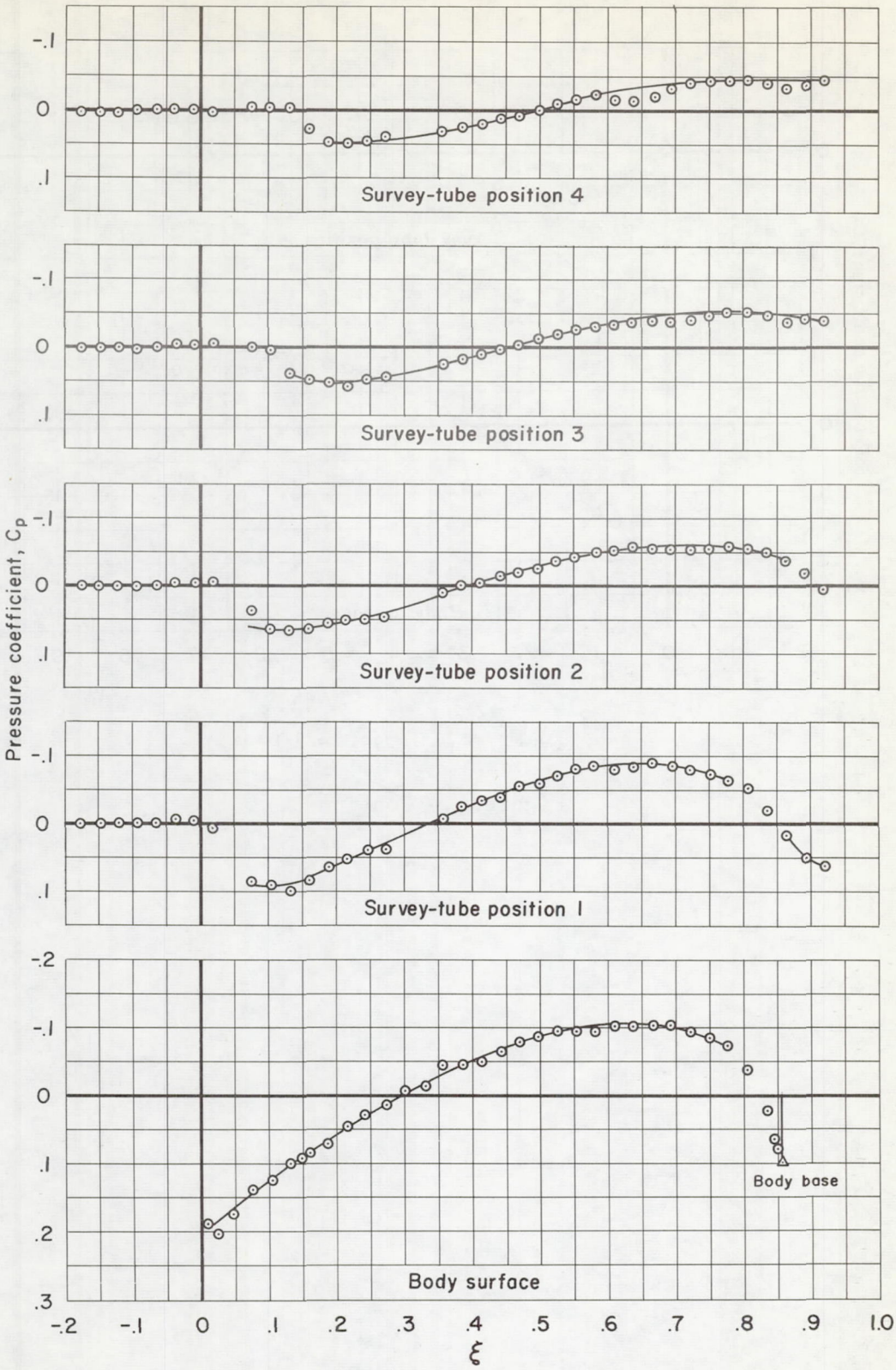

(l) $M_\infty = 1.10$, f = 10

Figure 6.- Continued.

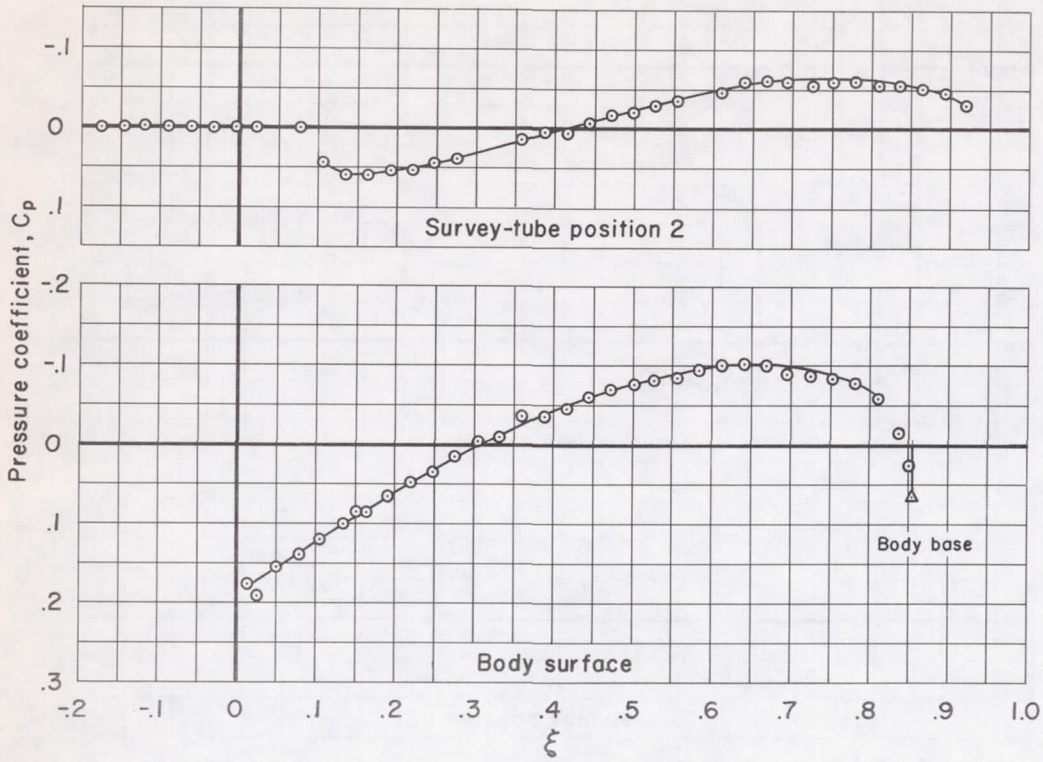

(m) $M_\infty = 1.15$, $f = 10$

Figure 6.- Continued.

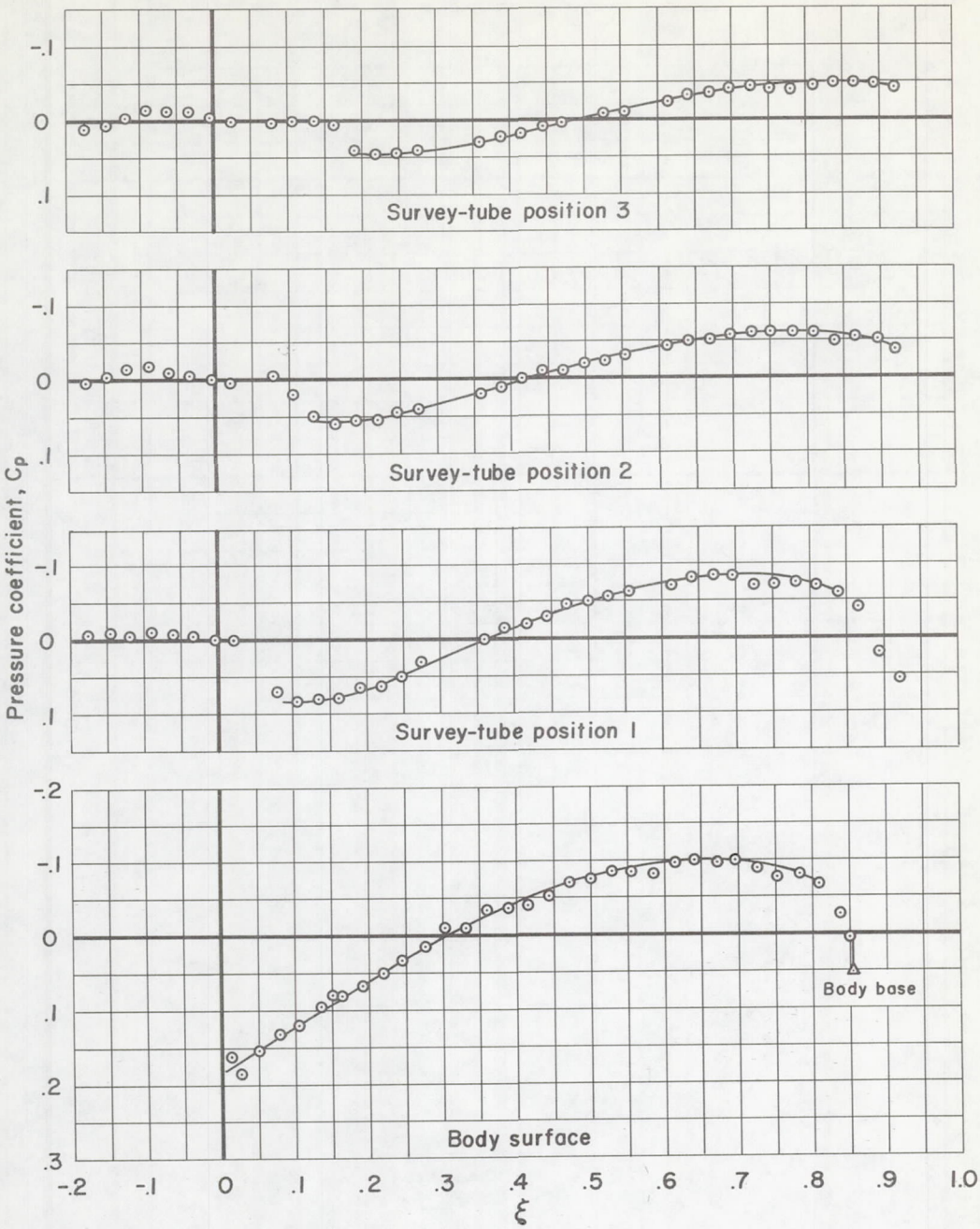

(n) $M_\infty = 1.20$, f = 10

Figure 6.- Concluded.

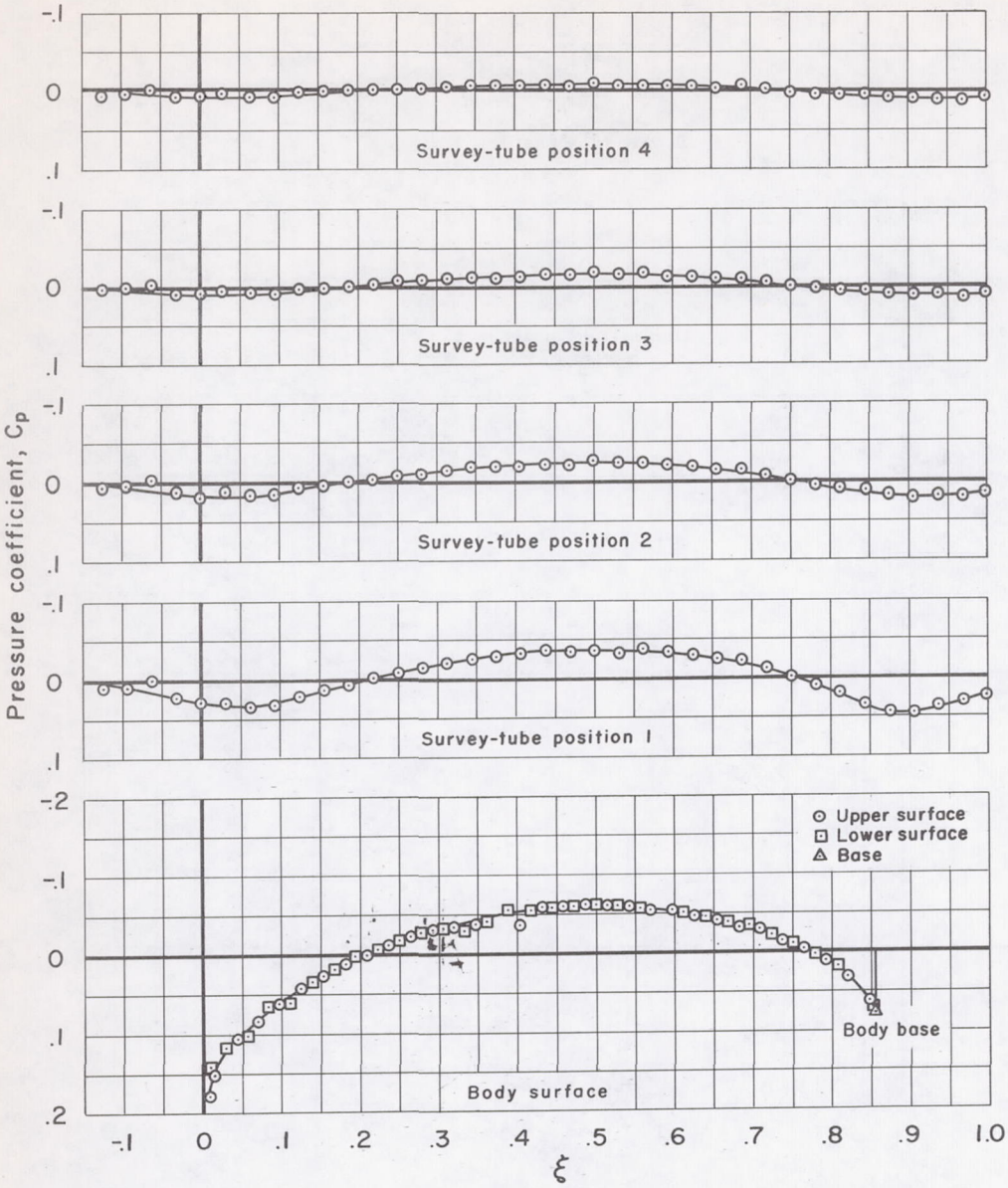

(a) $M_\infty = 0.80$, $f = 12$

Figure 7.- Measured pressure distributions for the body having a fineness ratio of 12.

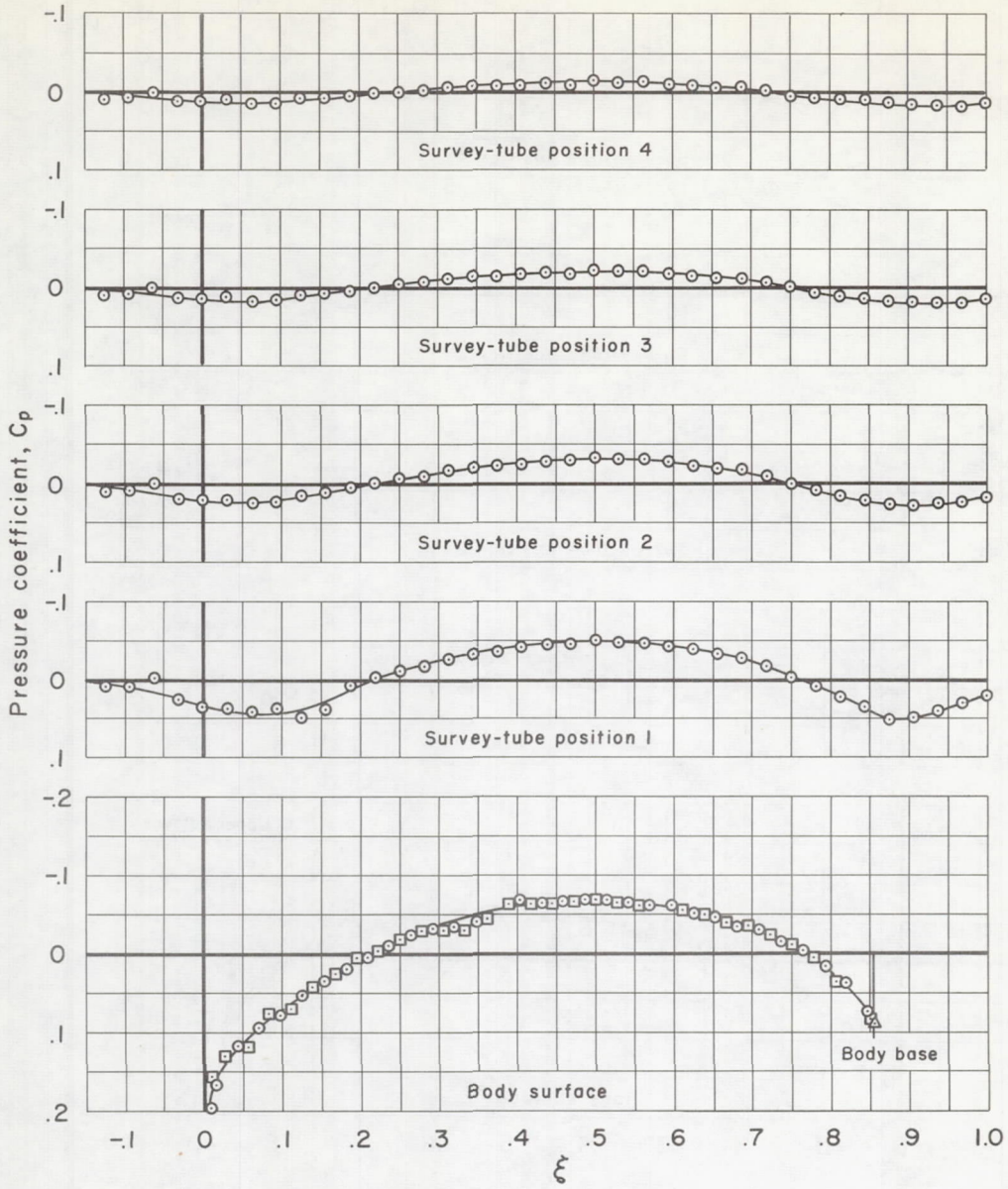

(b) $M_\infty = 0.90$, f = 12

Figure 7.- Continued.

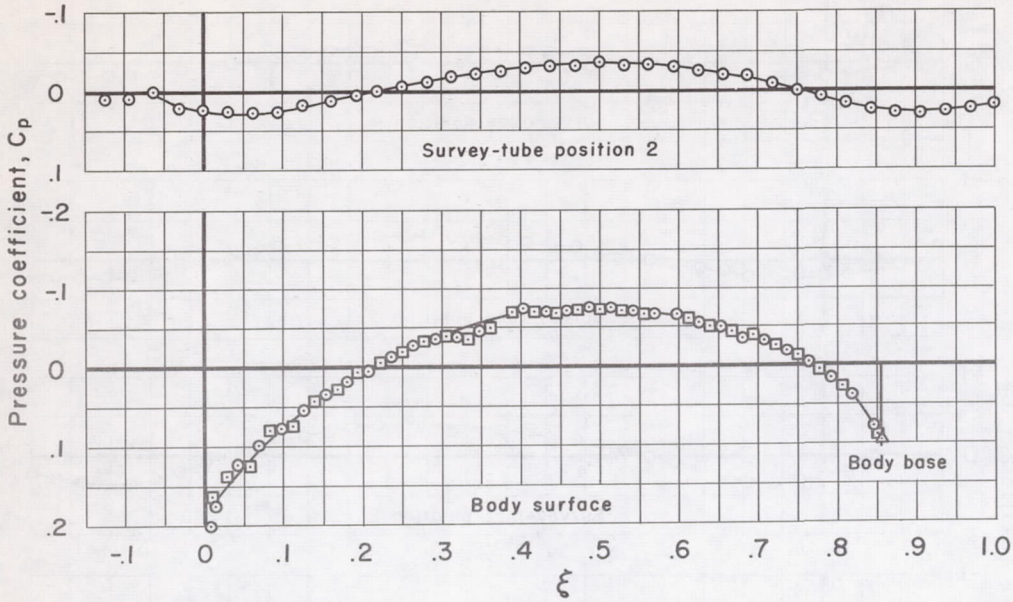

(c) $M_\infty = 0.925$, f = 12

Figure 7.- Continued.

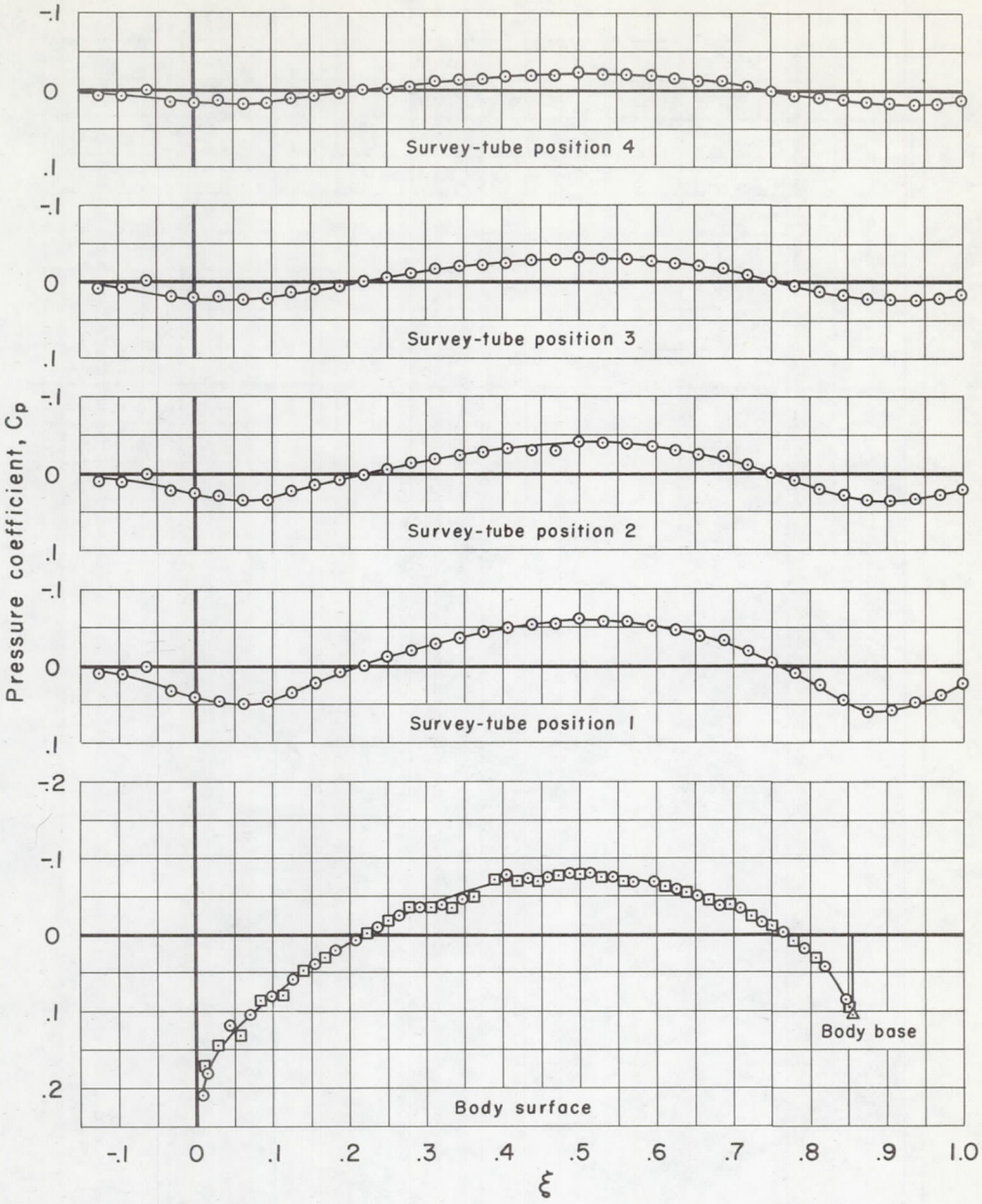

(d) $M_\infty = 0.95$, $f = 12$

Figure 7.- Continued.

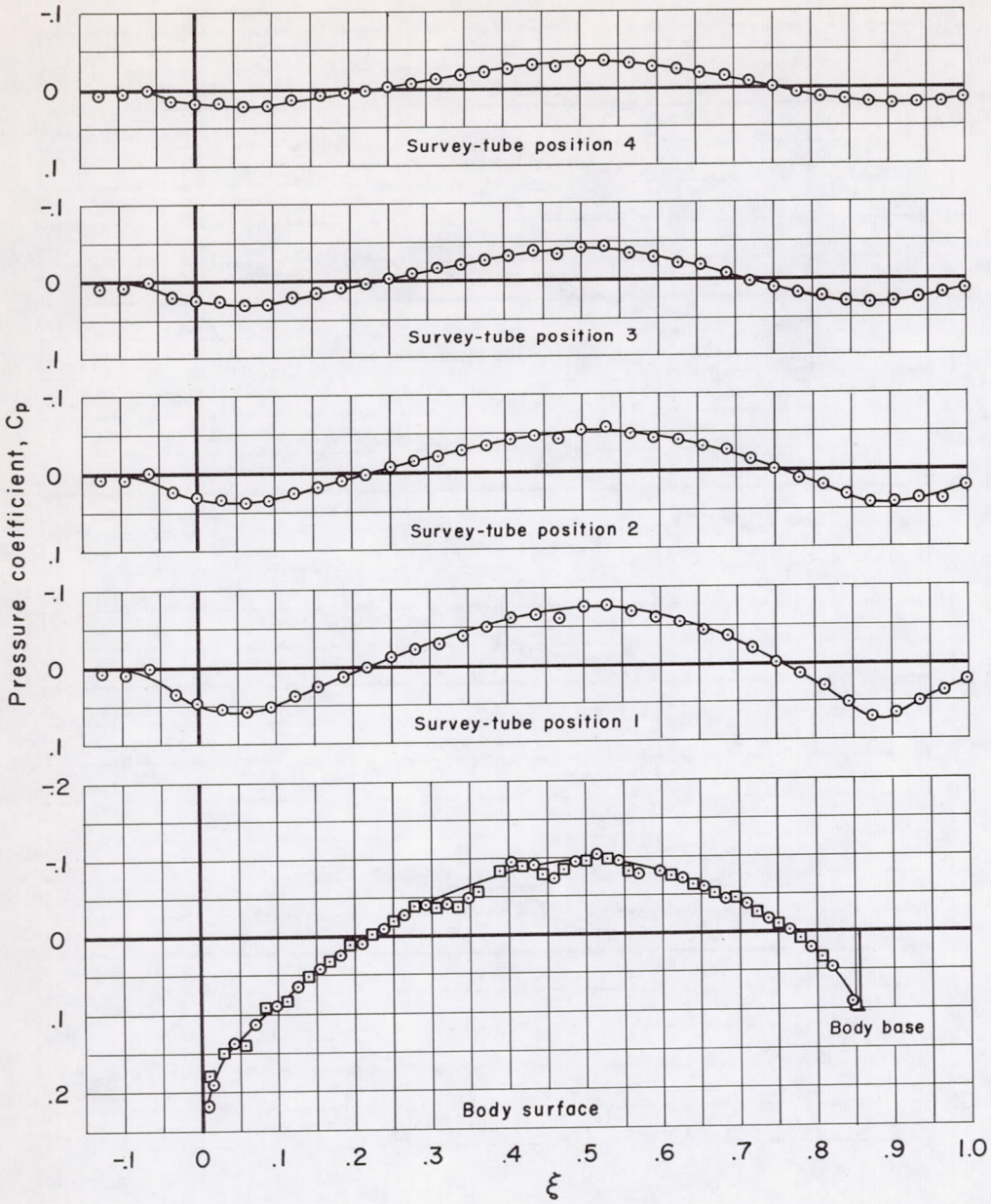

(e) $M_\infty = 0.975$, f = 12

Figure 7.- Continued.

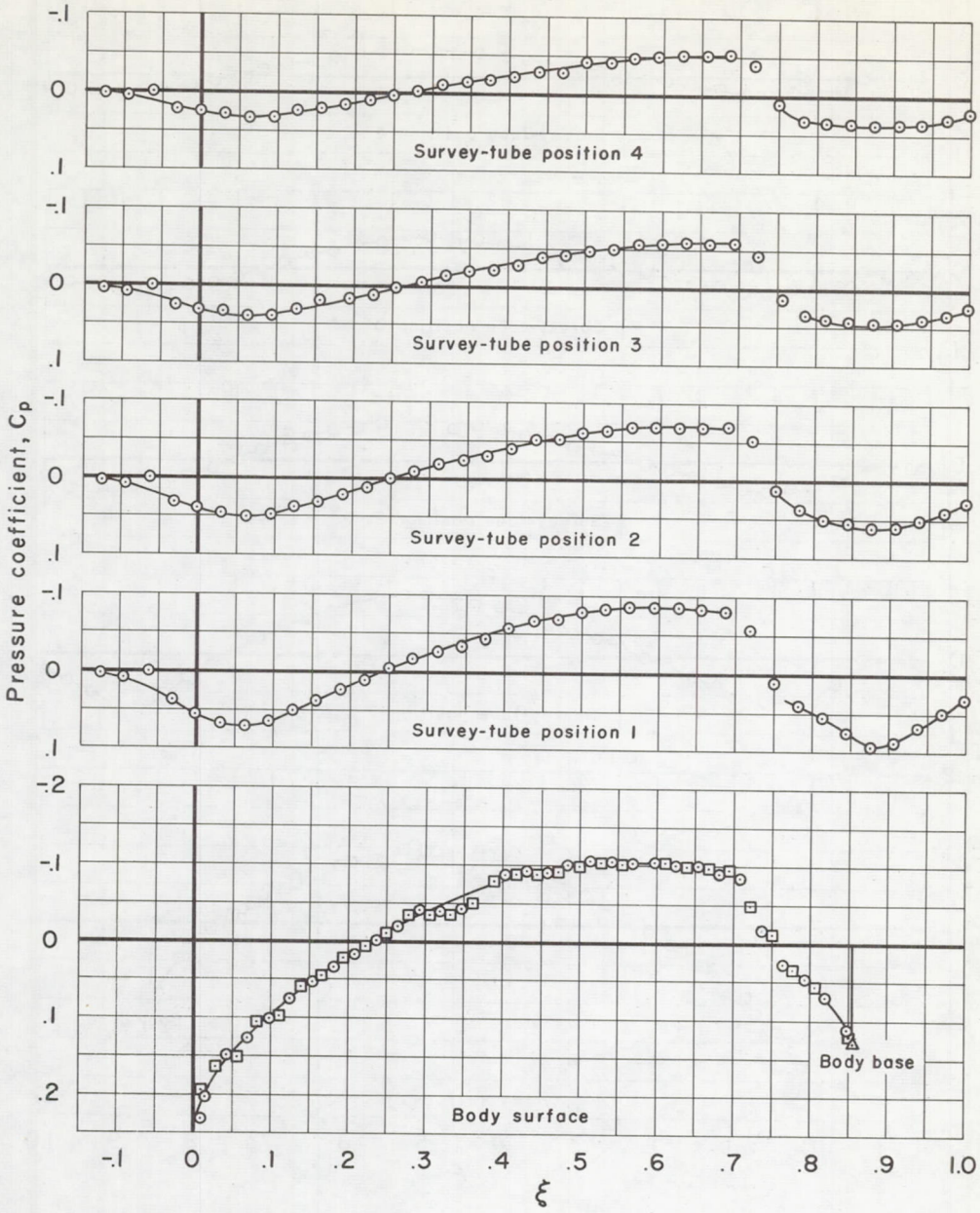

(f) $M_\infty = 1.00$, f = 12

Figure 7.- Continued.

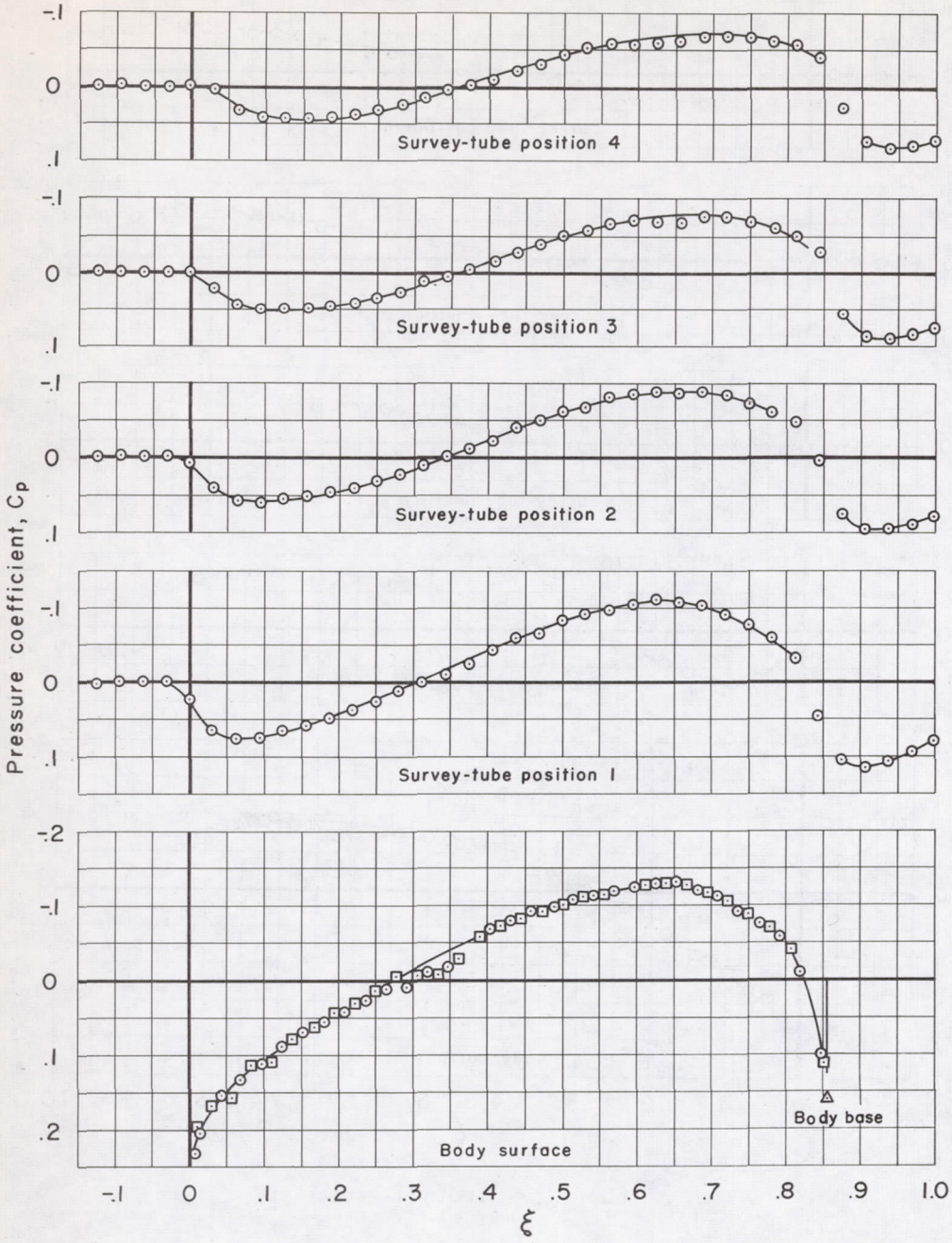

(g) $M_\infty = 1.025$, f = 12

Figure 7.- Continued.

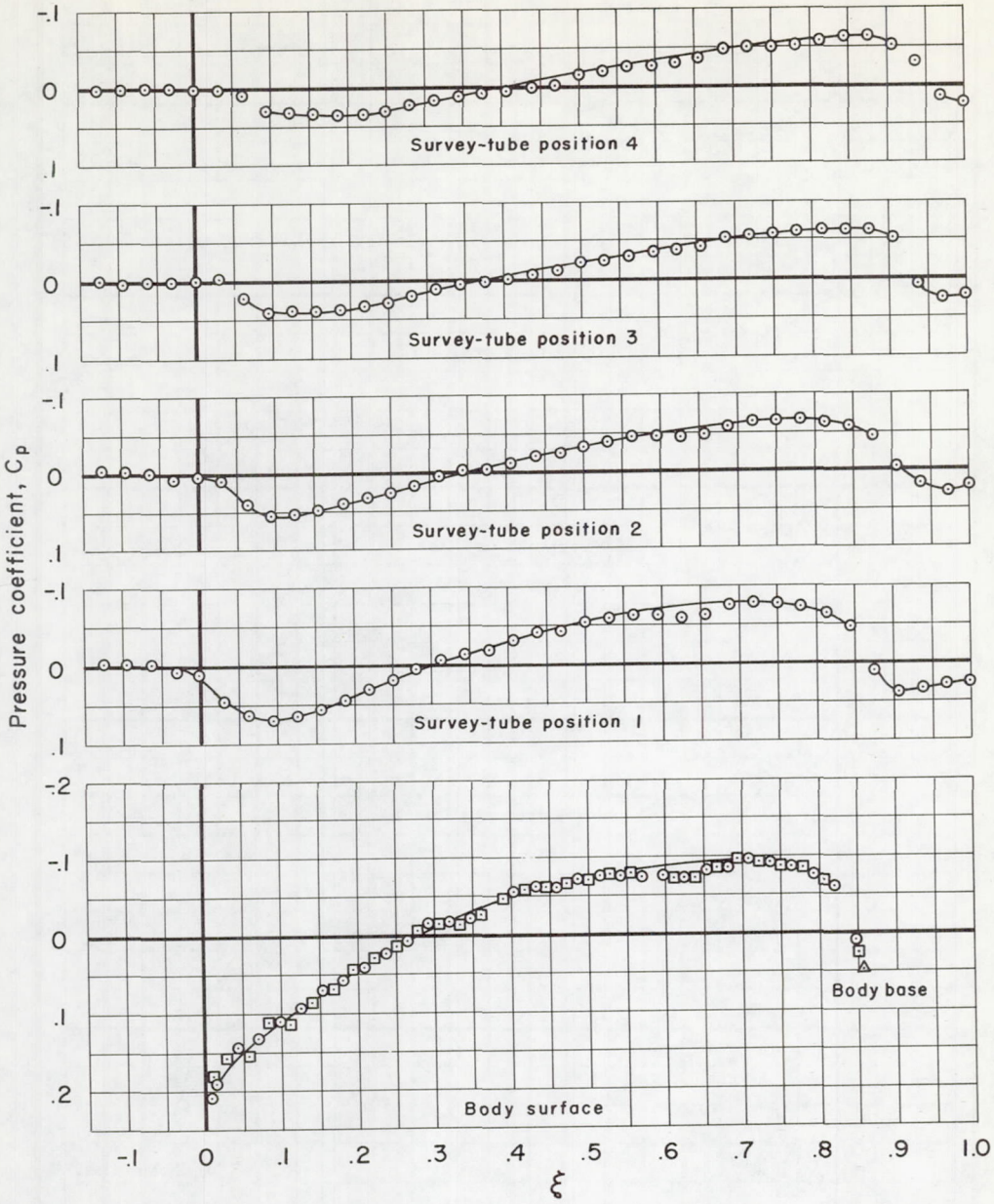

(h) $M_\infty = 1.05$, f = 12

Figure 7.- Continued.

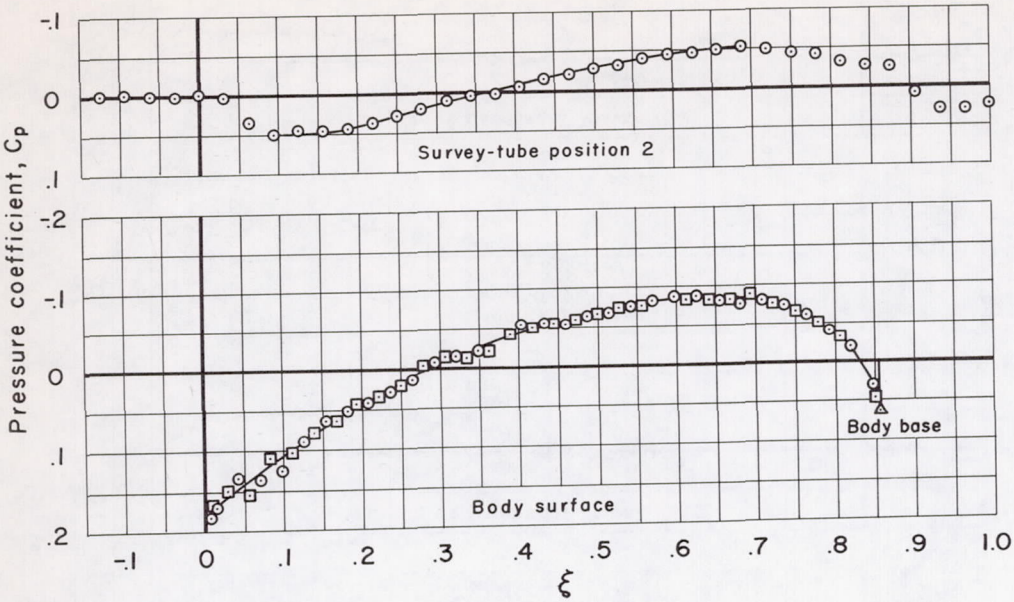

(i) $M_\infty = 1.075$, $f = 12$

Figure 7.- Continued.

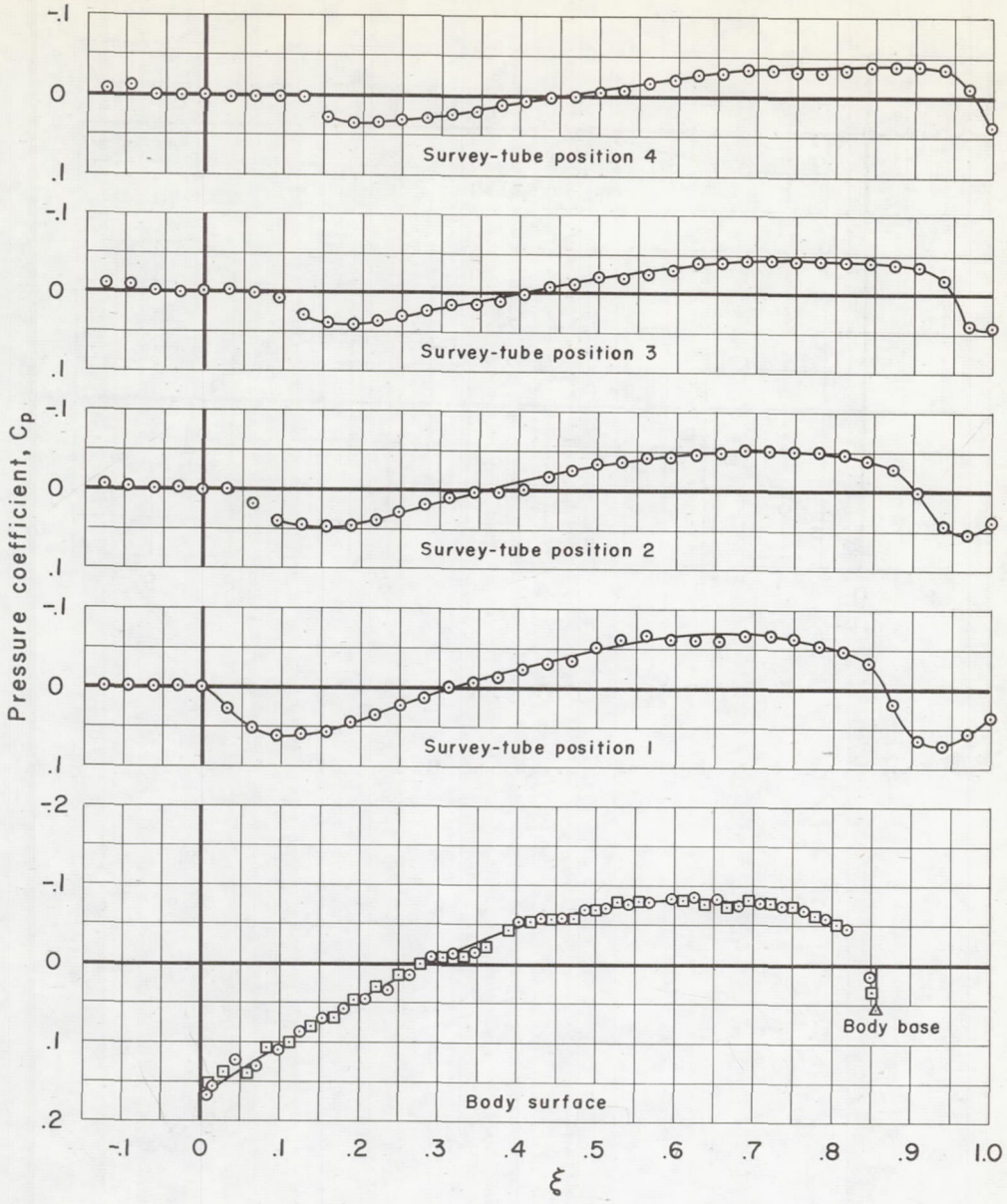

(j) $M_\infty = 1.10$, $f = 12$

Figure 7.- Continued.

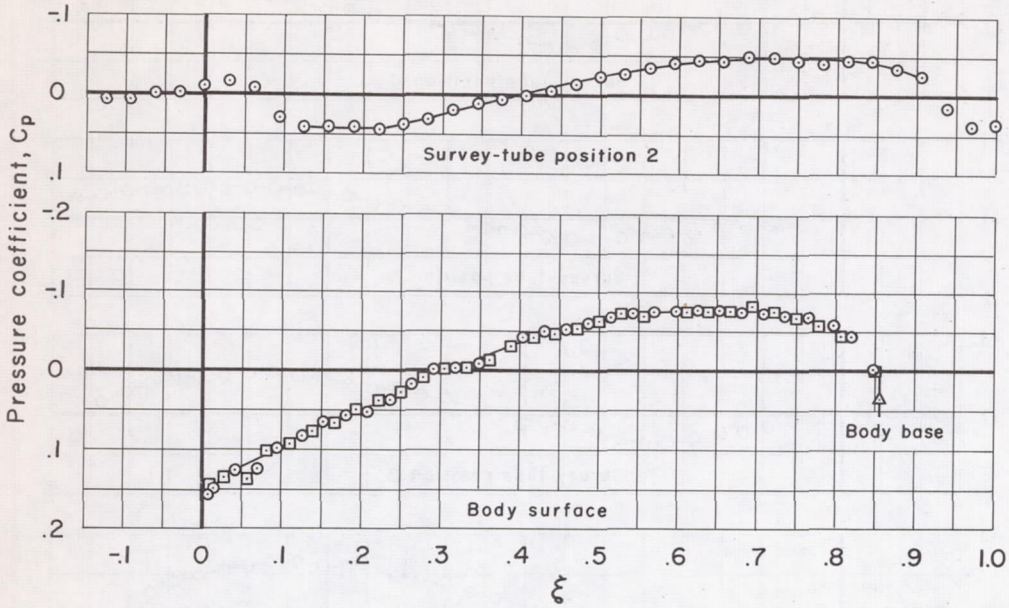

(k) $M_\infty = 1.15$, f = 12

Figure 7.- Continued.

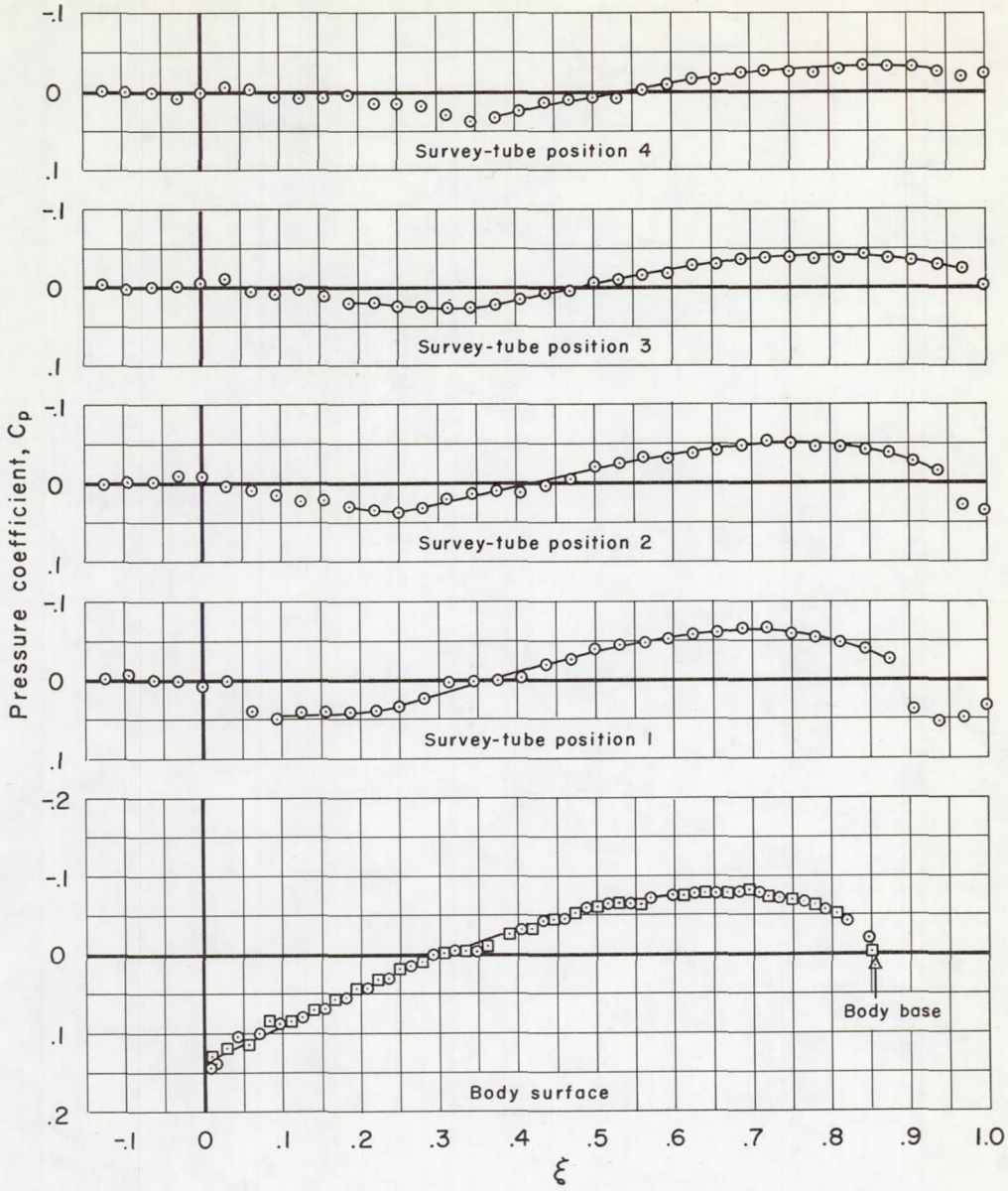

(*l*) $M_\infty = 1.20$, f = 12

Figure 7.- Concluded.

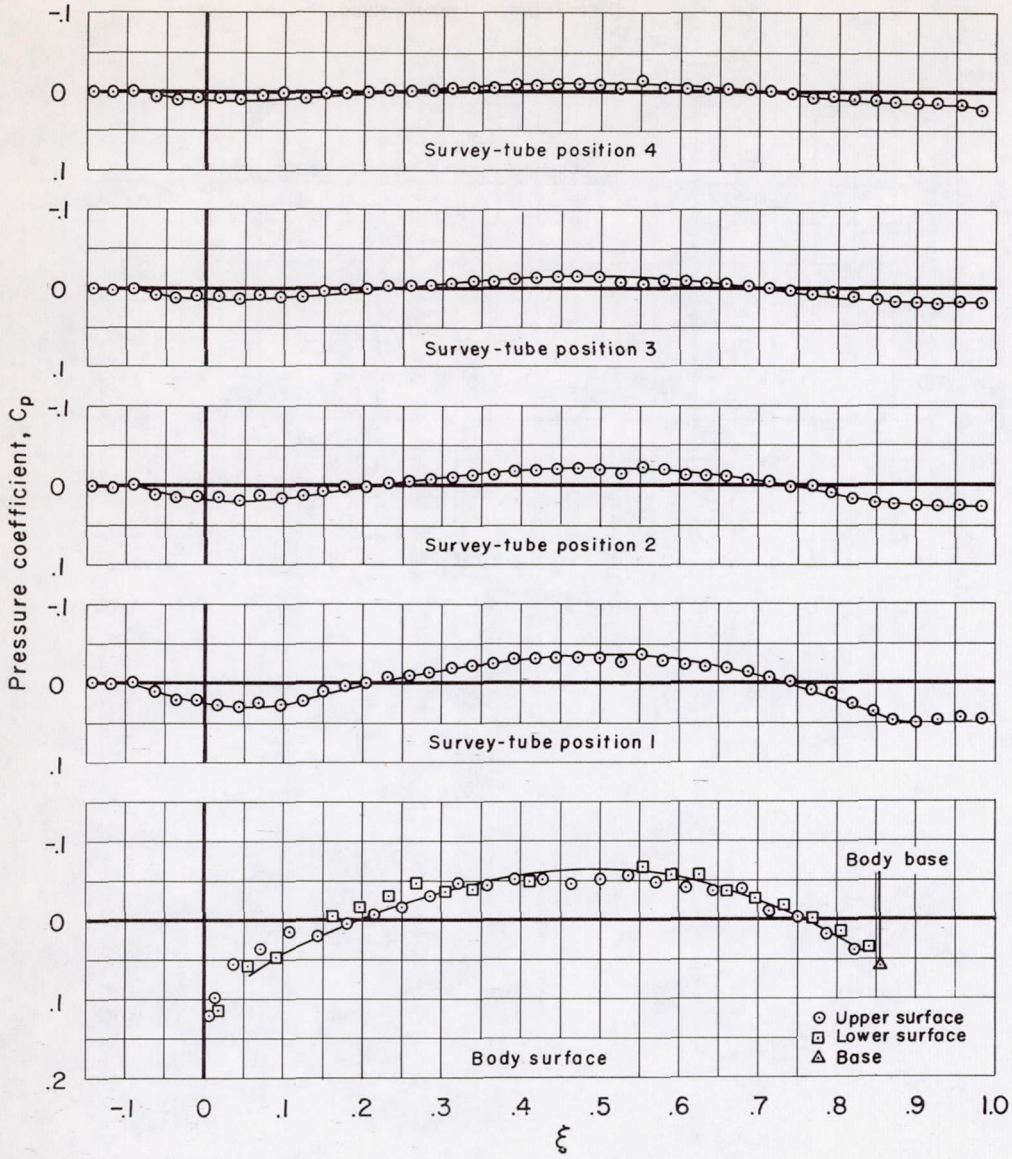

(a) $M_\infty = 0.80$, f = 14

Figure 8.- Measured pressure distributions for the body having a fineness ratio of 14.

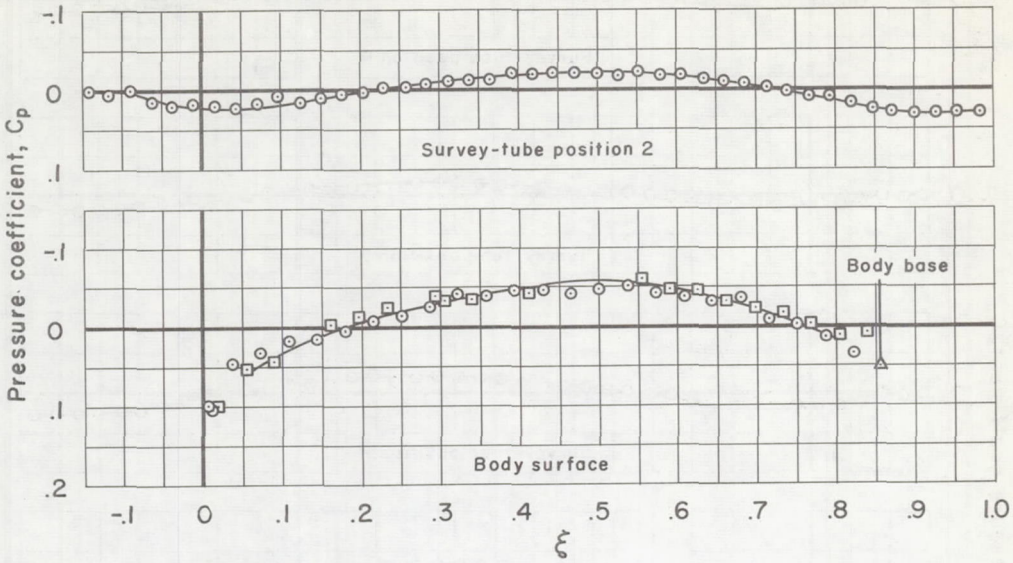

(b) $M_\infty = 0.85$, $f = 14$

Figure 8.- Continued.

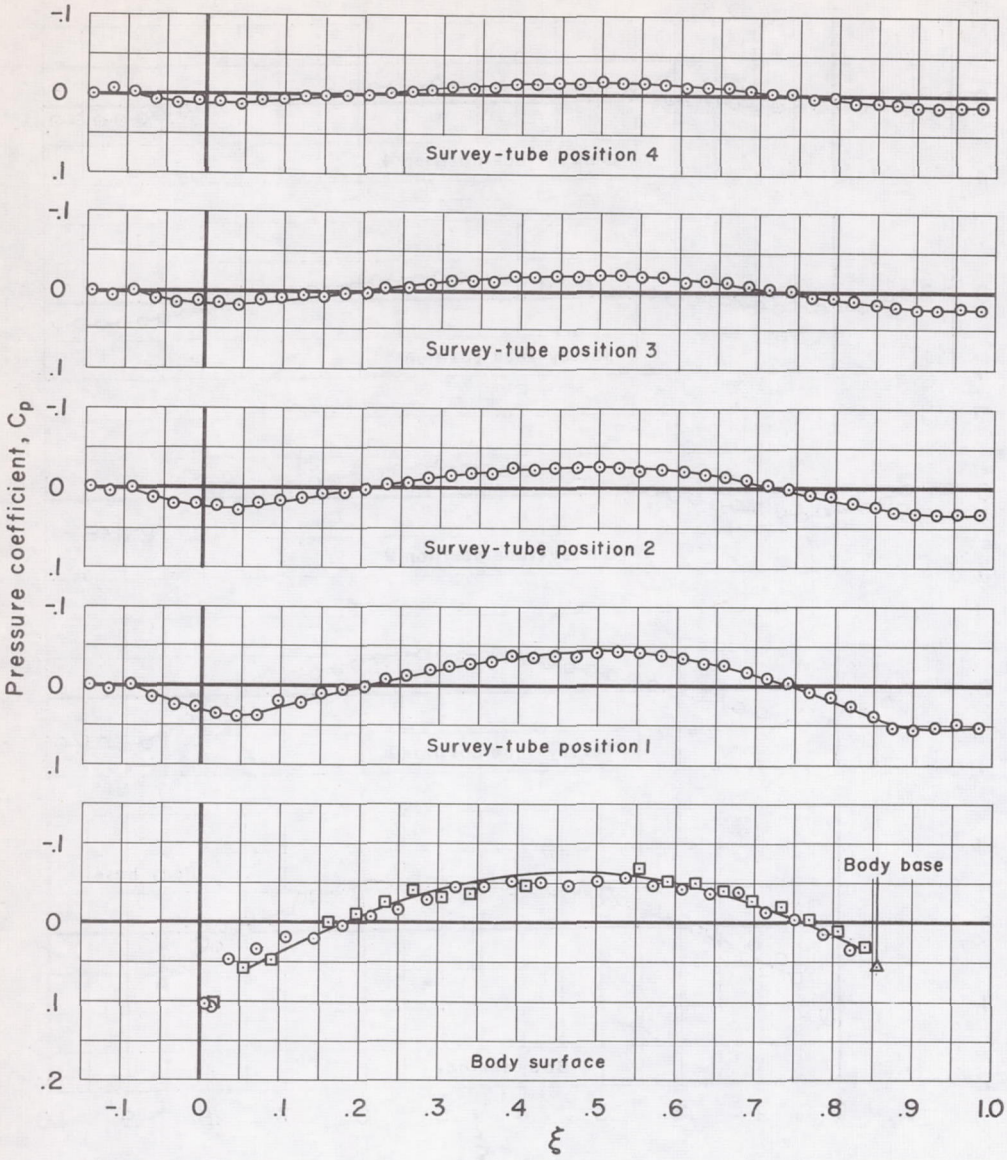

(c) $M_\infty = 0.90$, $f = 14$

Figure 8.- Continued.

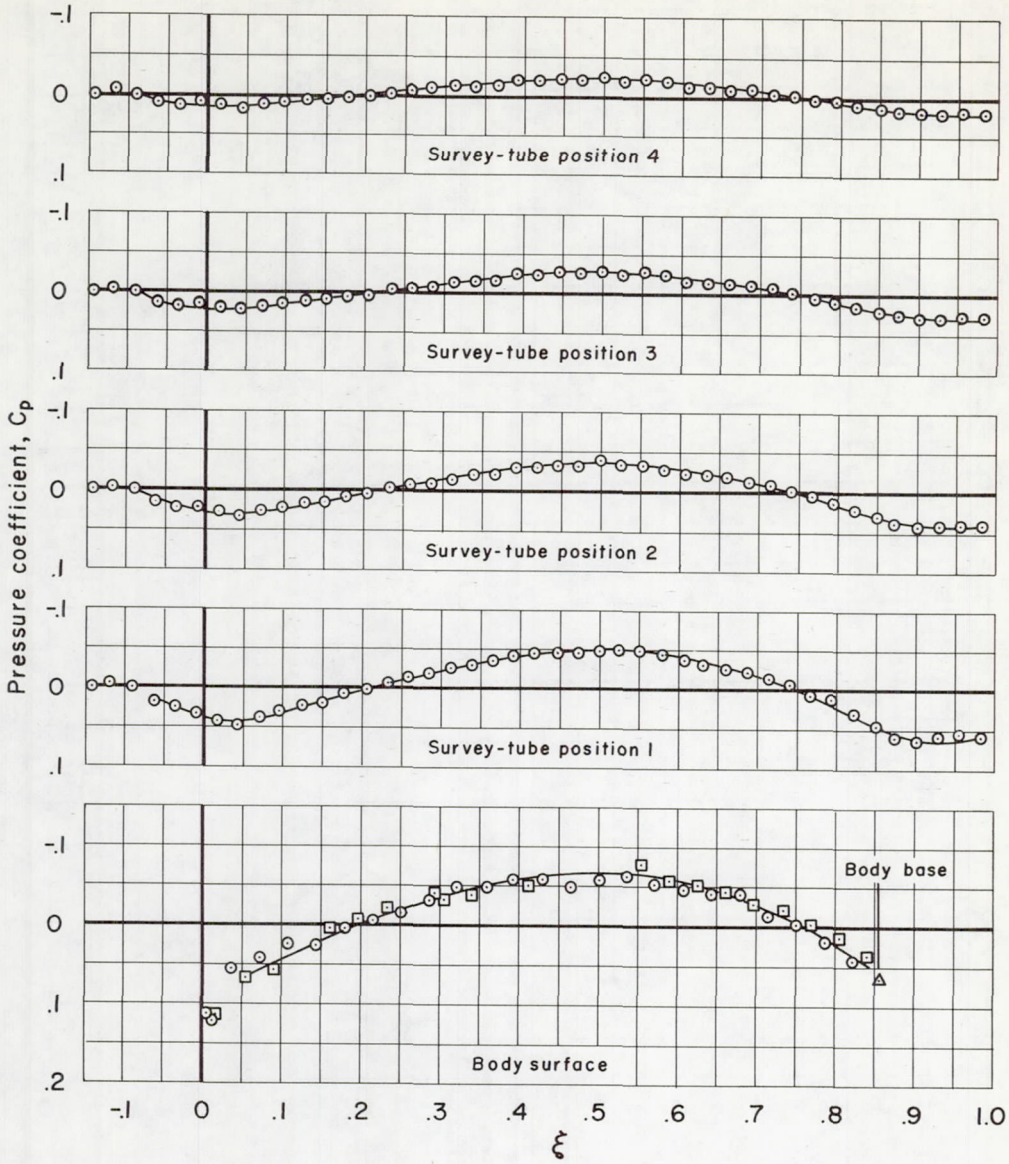

(d) $M_\infty = 0.95$, f = 14

Figure 8.- Continued.

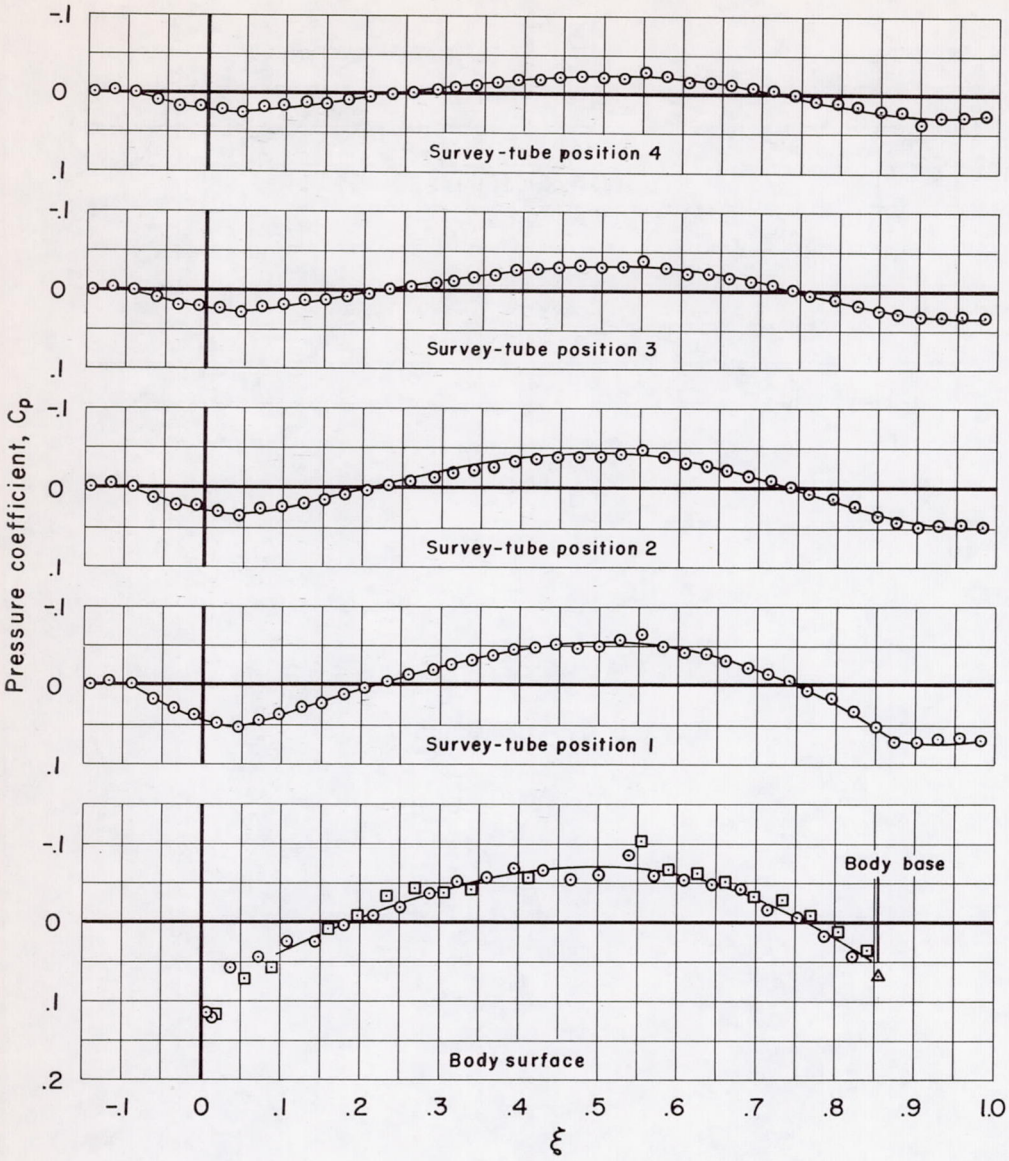

(e) $M_\infty = 0.975$, f = 14

Figure 8.- Continued.

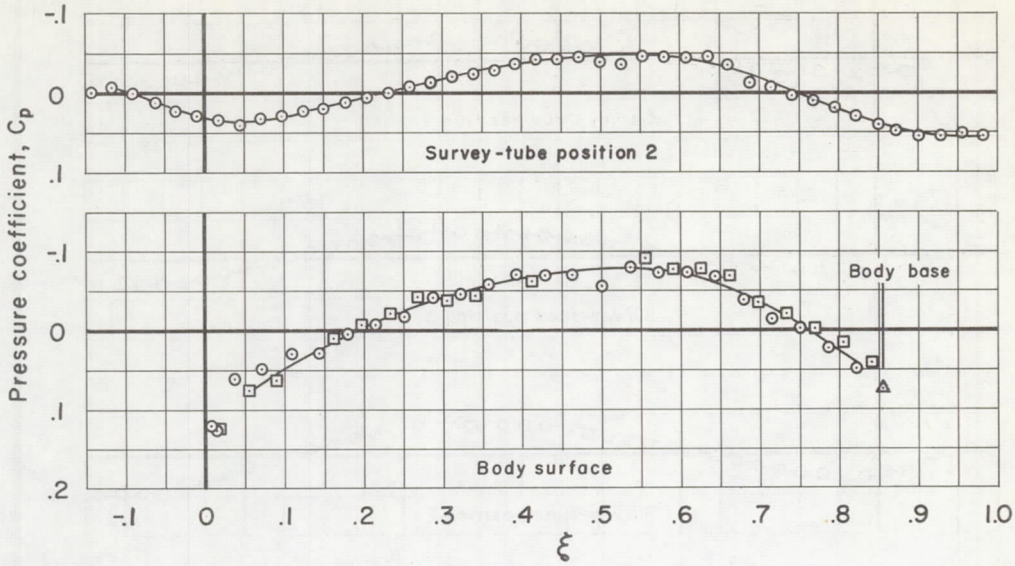

(f) $M_\infty = 0.99$, f = 14

Figure 8.- Continued.

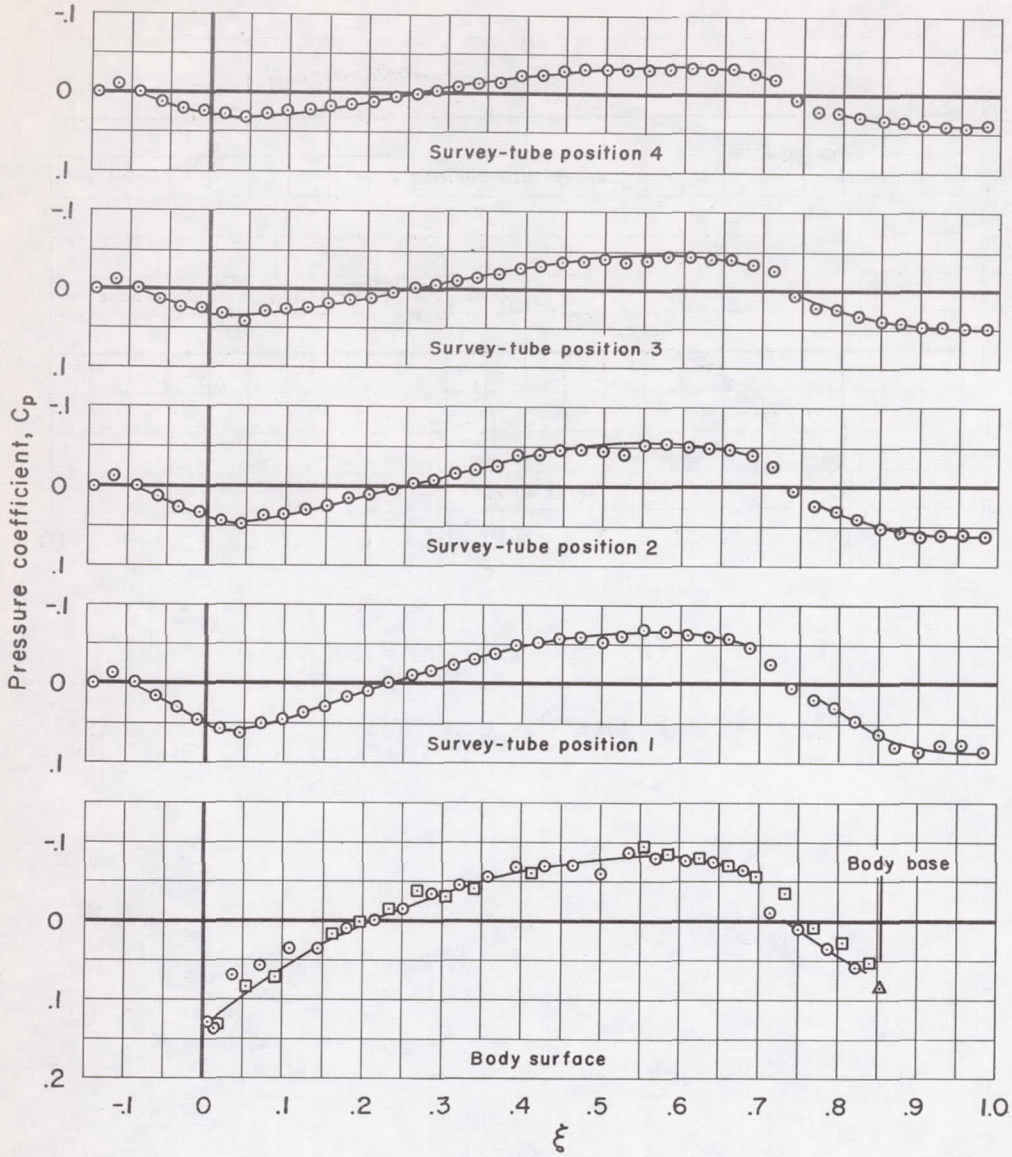

(g) $M_\infty = 1.00$, $f = 14$

Figure 8.- Continued.

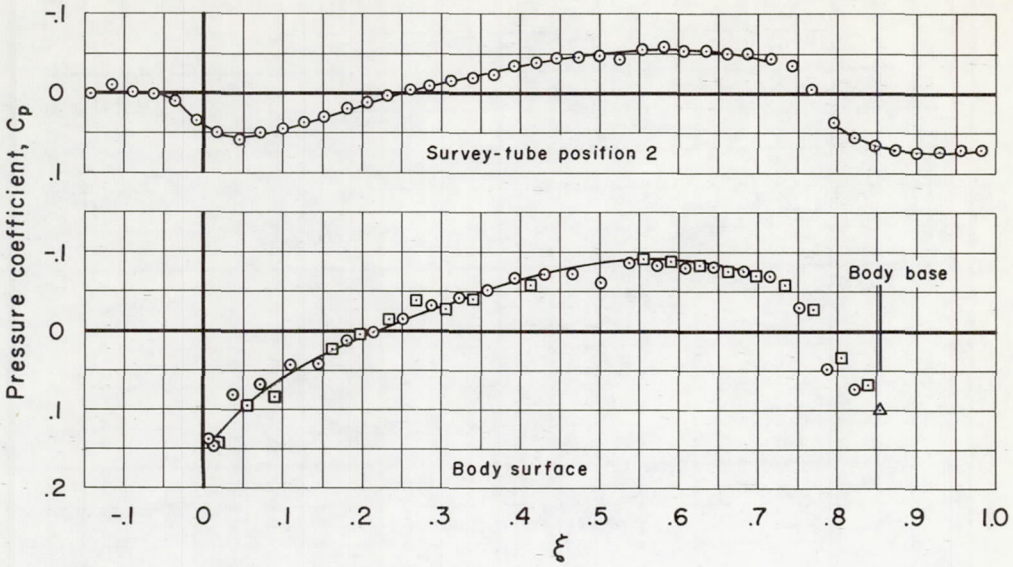

(h) $M_\infty = 1.01$, $f = 14$

Figure 8.- Continued.

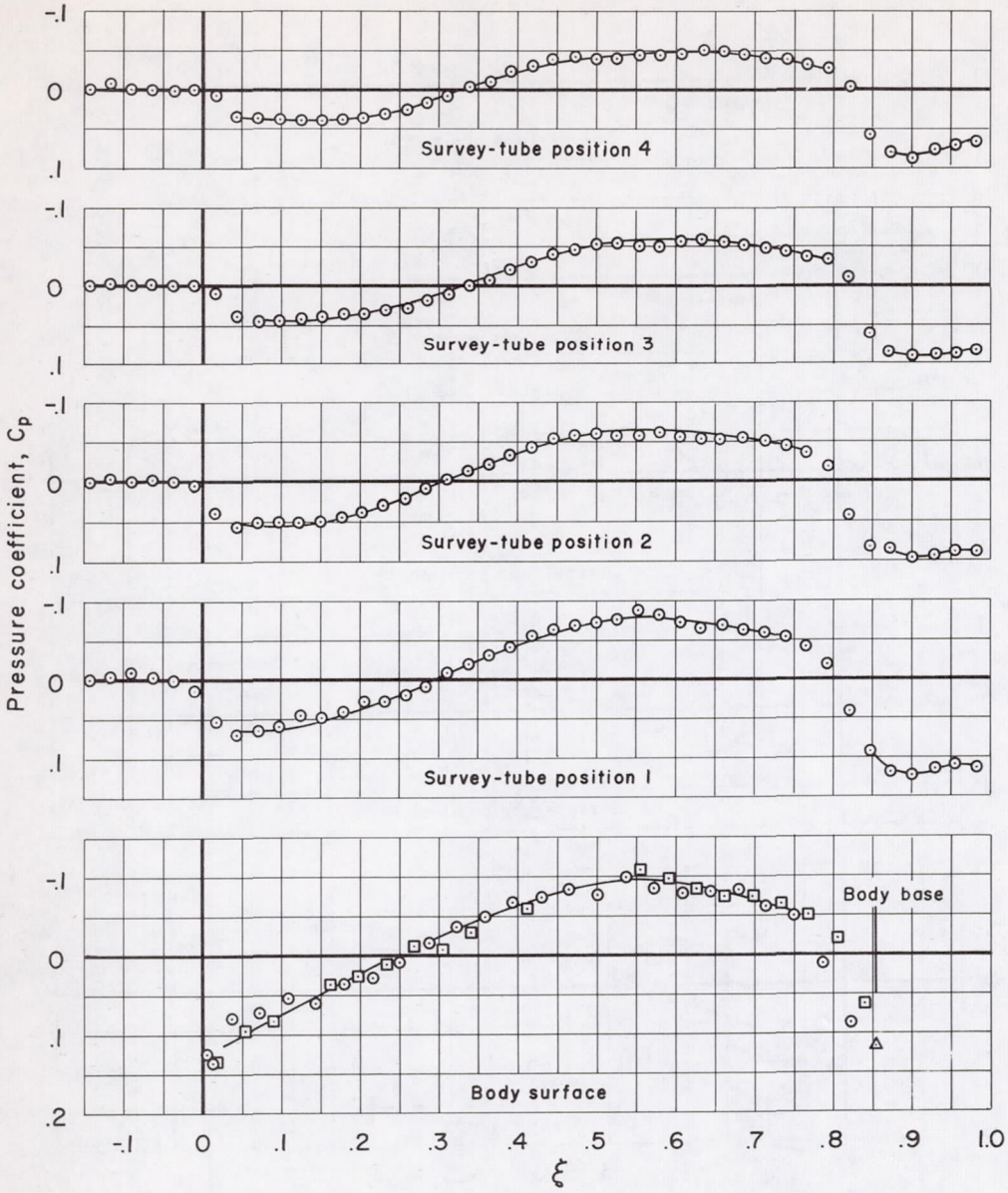

(i) $M_\infty = 1.025$, $f = 14$

Figure 8.- Continued.

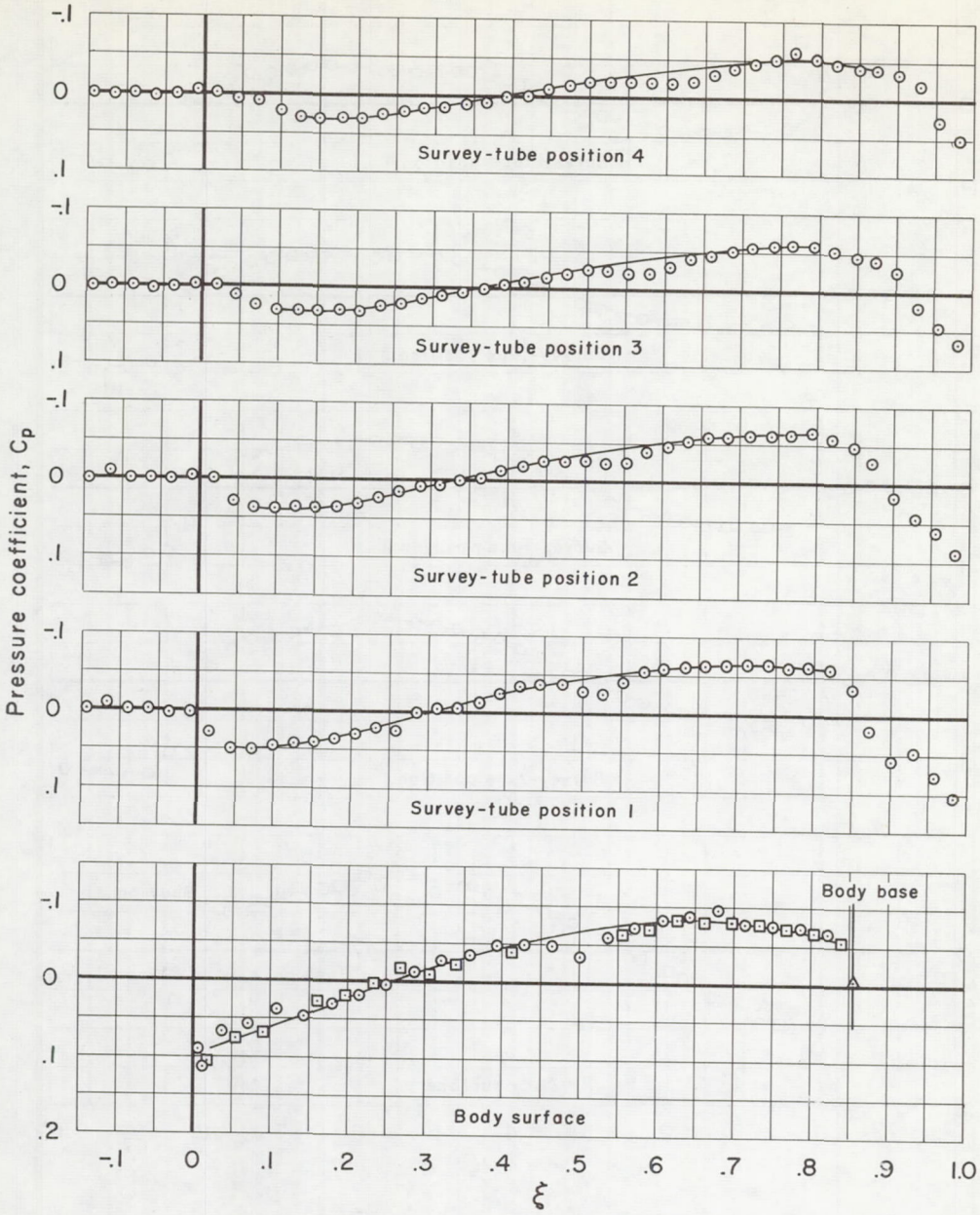

(j) $M_\infty = 1.05$, f = 14

Figure 8.- Continued.

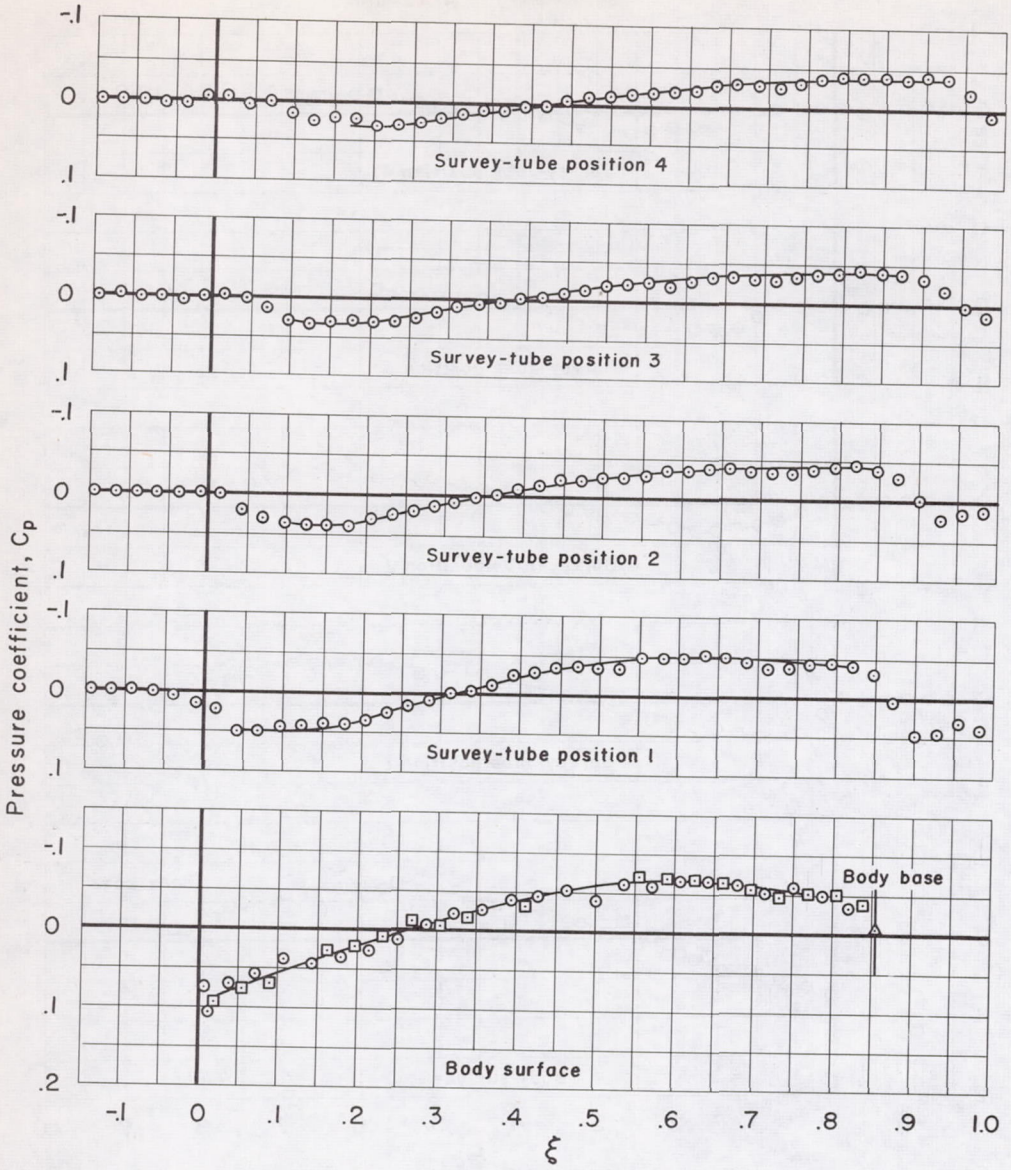

(k) $M_\infty = 1.075$, f = 14

Figure 8.- Continued.

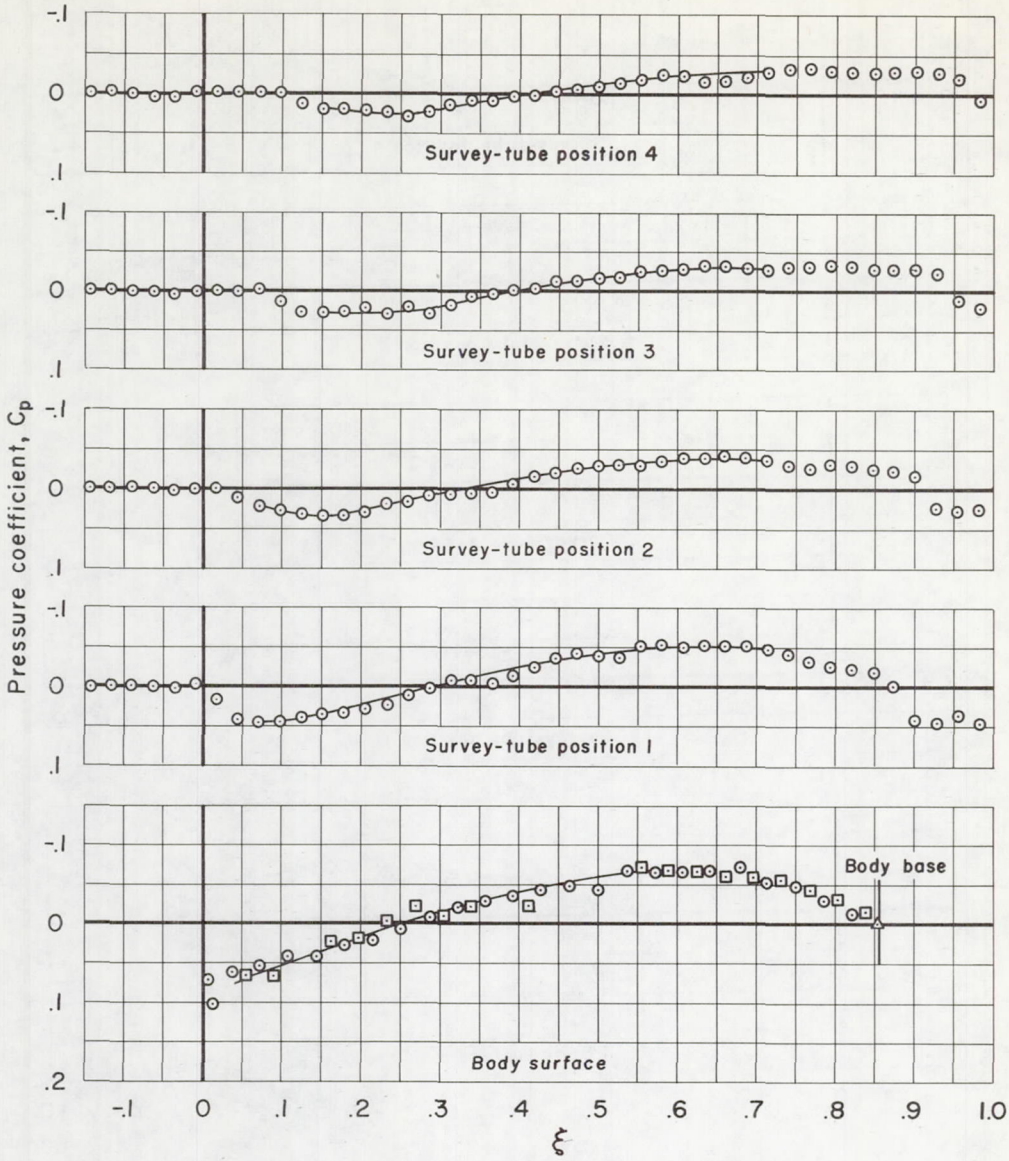

(*l*) $M_\infty = 1.10$, f = 14

Figure 8.- Continued.

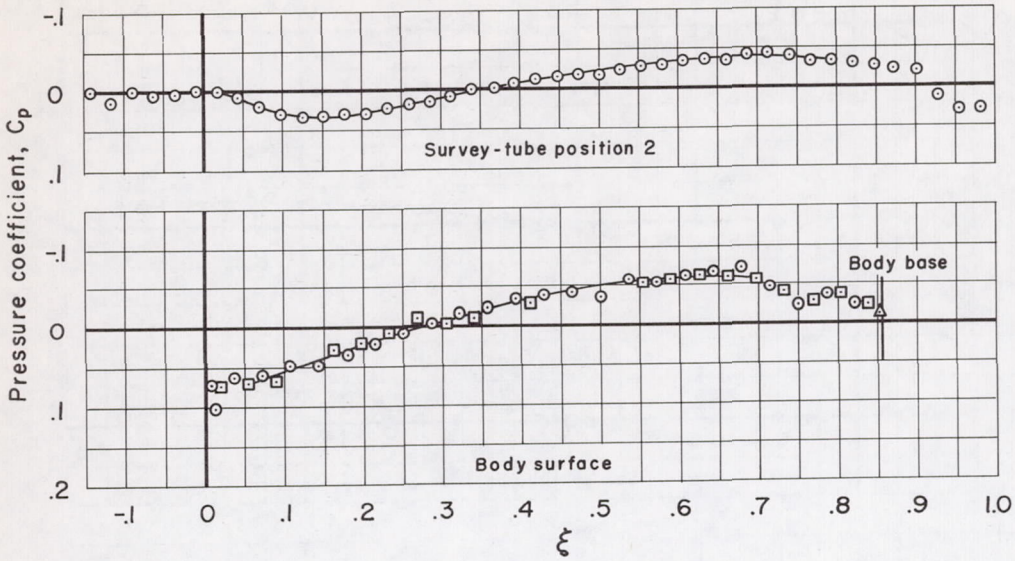

(m) $M_\infty = 1.15$, f = 14

Figure 8.- Continued.

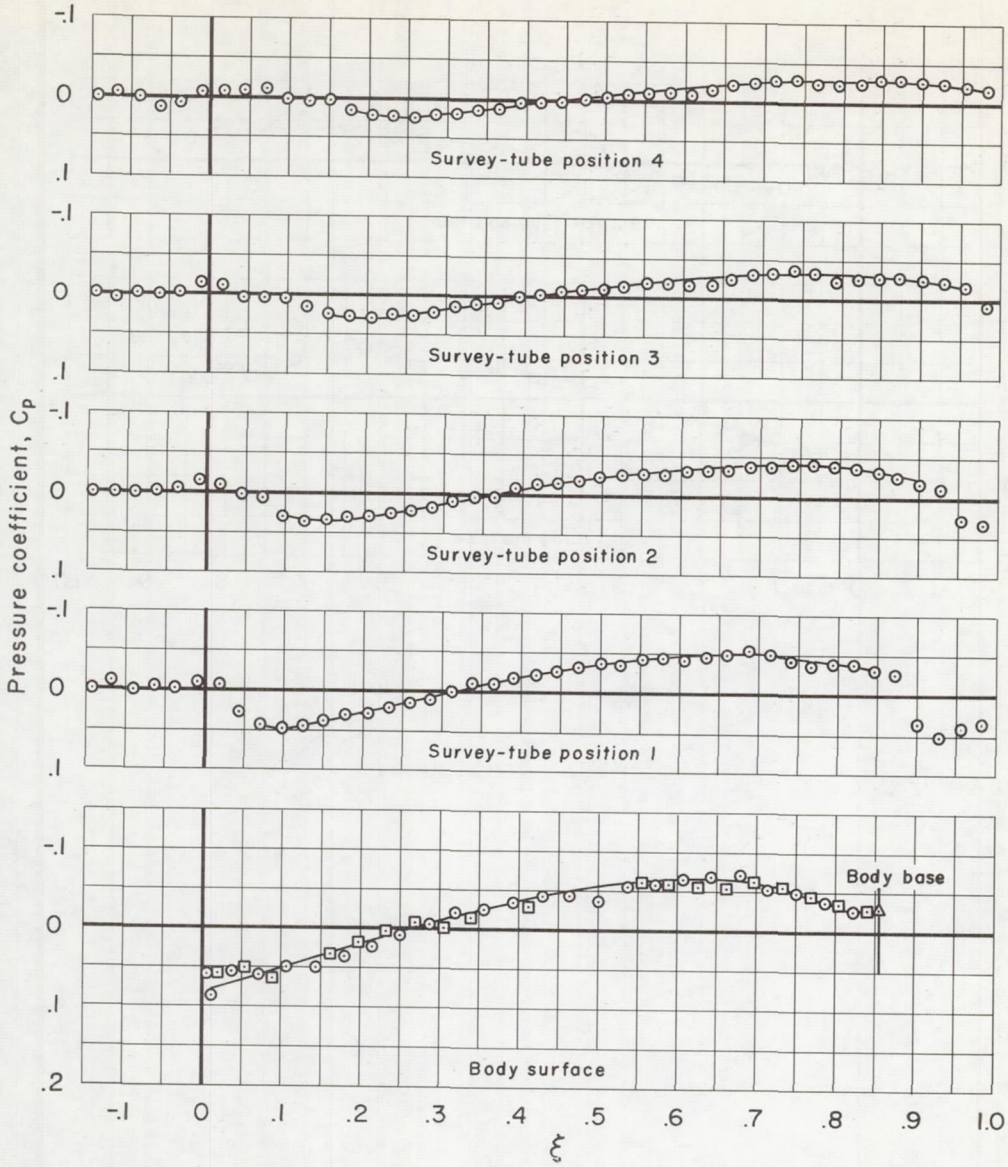

(n) $M_\infty = 1.20$, $f = 14$

Figure 8.- Concluded.

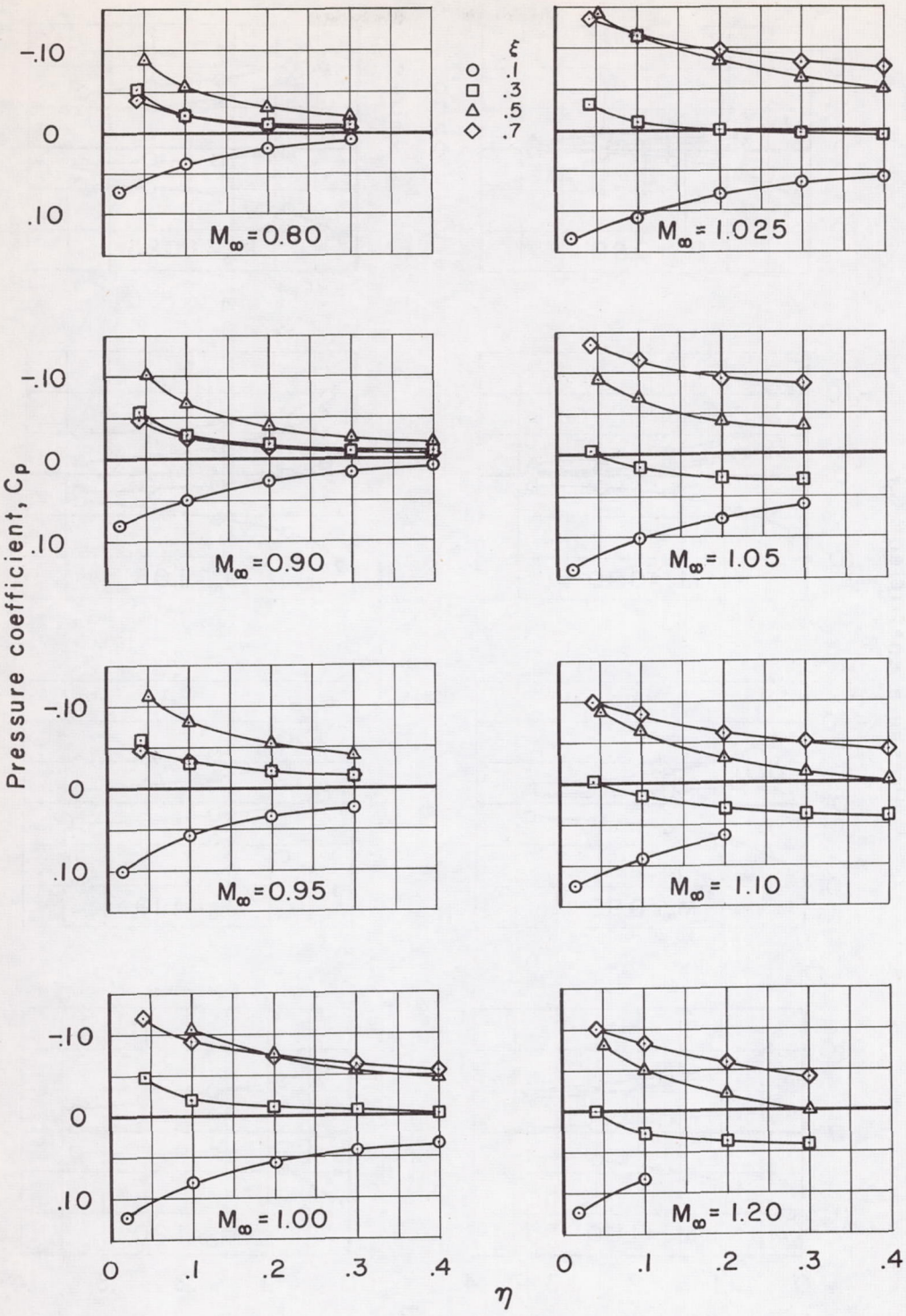

Figure 9.- Variation of pressure coefficient with radial distance, η, for the body having a fineness ratio of 10.

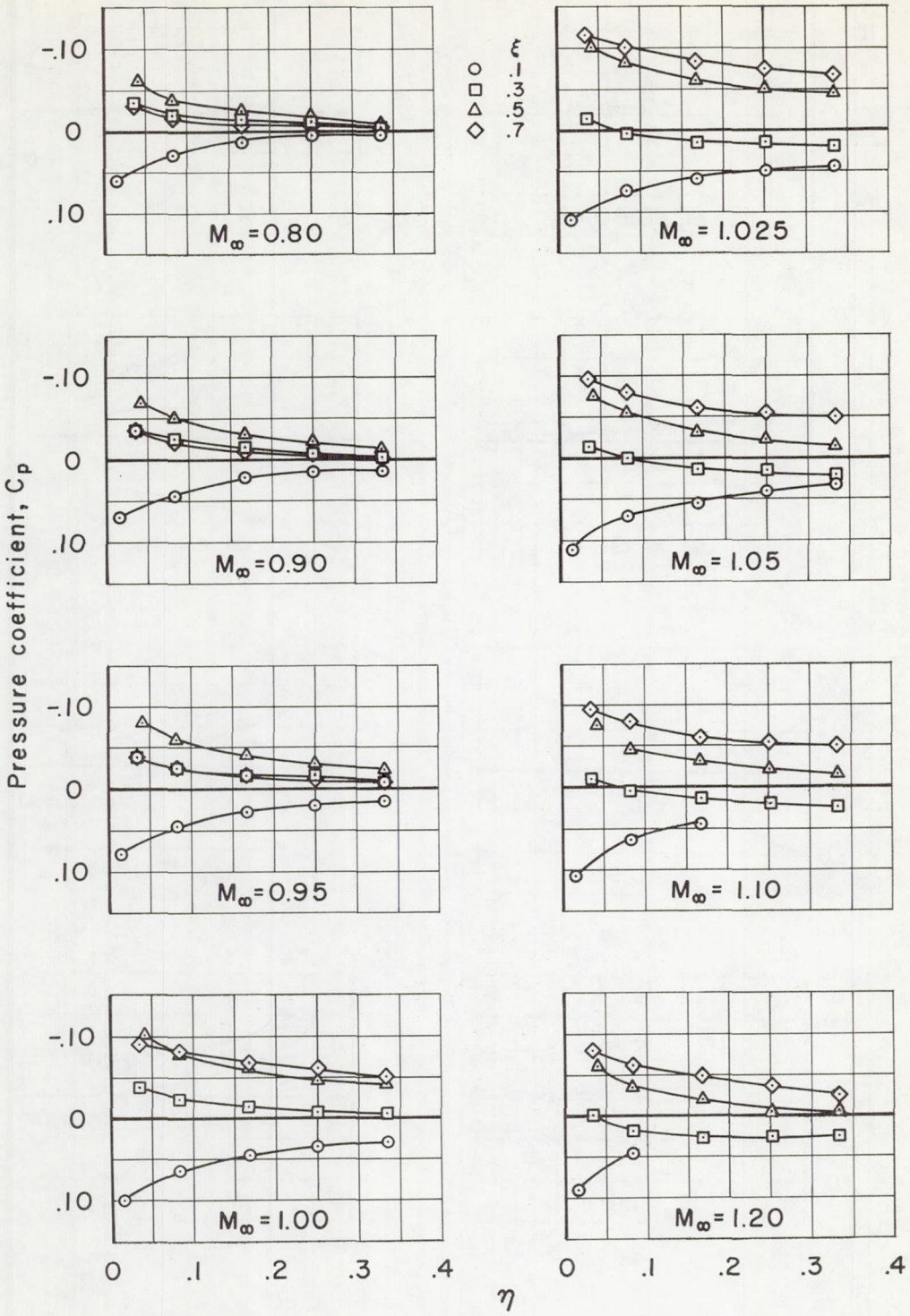

Figure 10.- Variation of pressure coefficient with radial distance, η, for the body having a fineness ratio of 12.

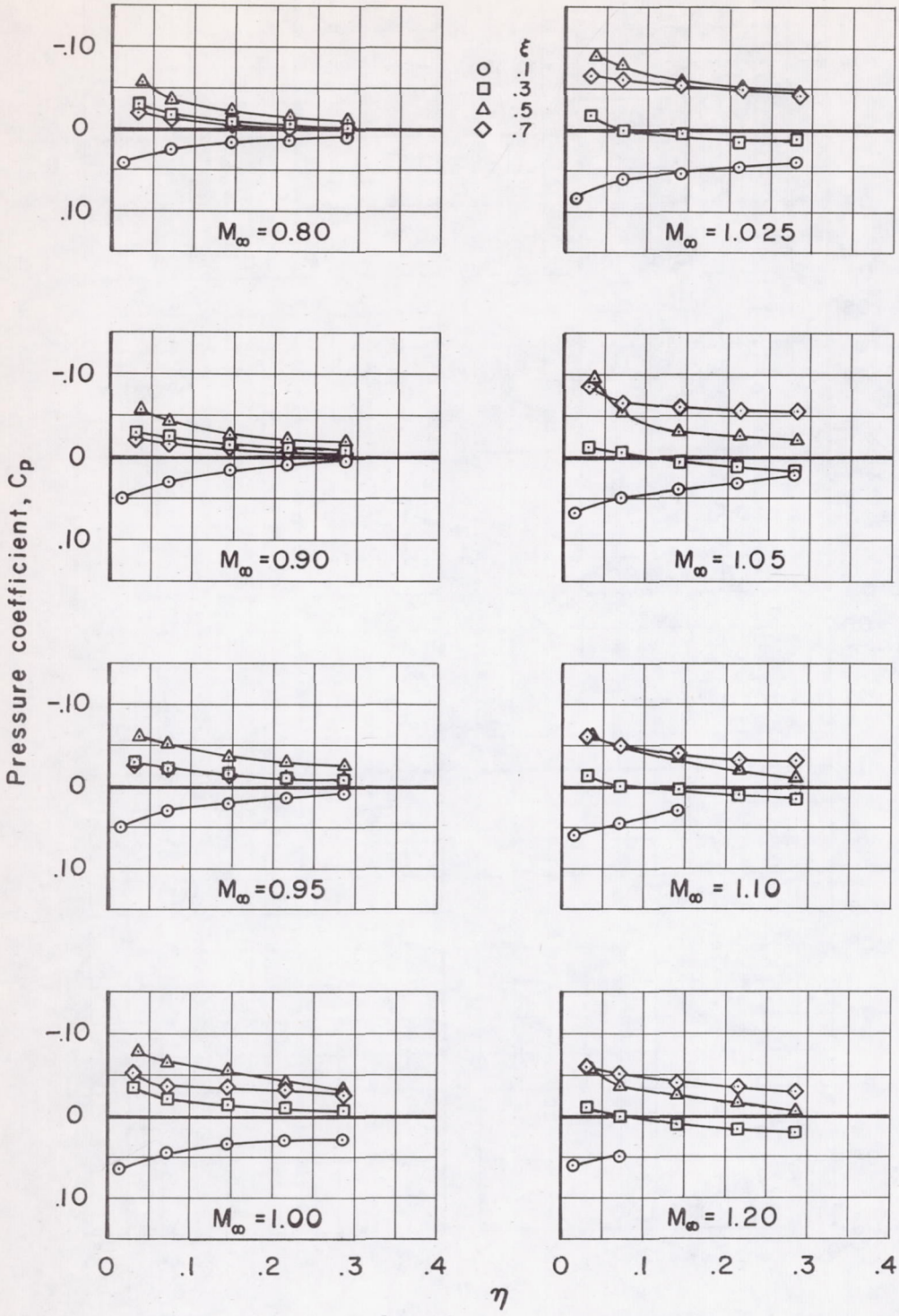

Figure 11.- Variation of pressure coefficient with radial distance, η, for the body having a fineness ratio of 14.

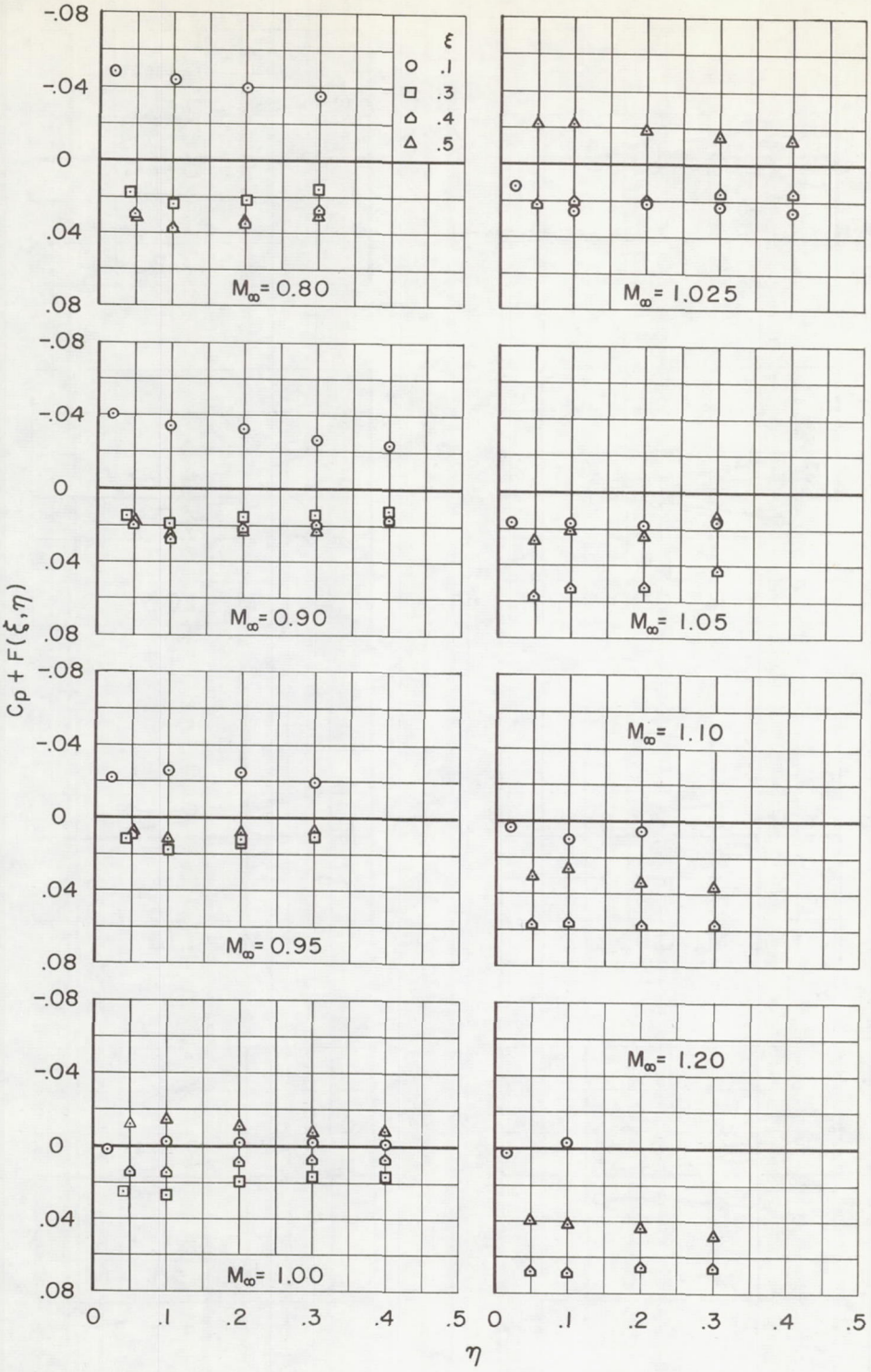

Figure 12.- Variation of $C_p + F(\xi,\eta)$ with radial distance, η, for the body having a fineness ratio of 10.

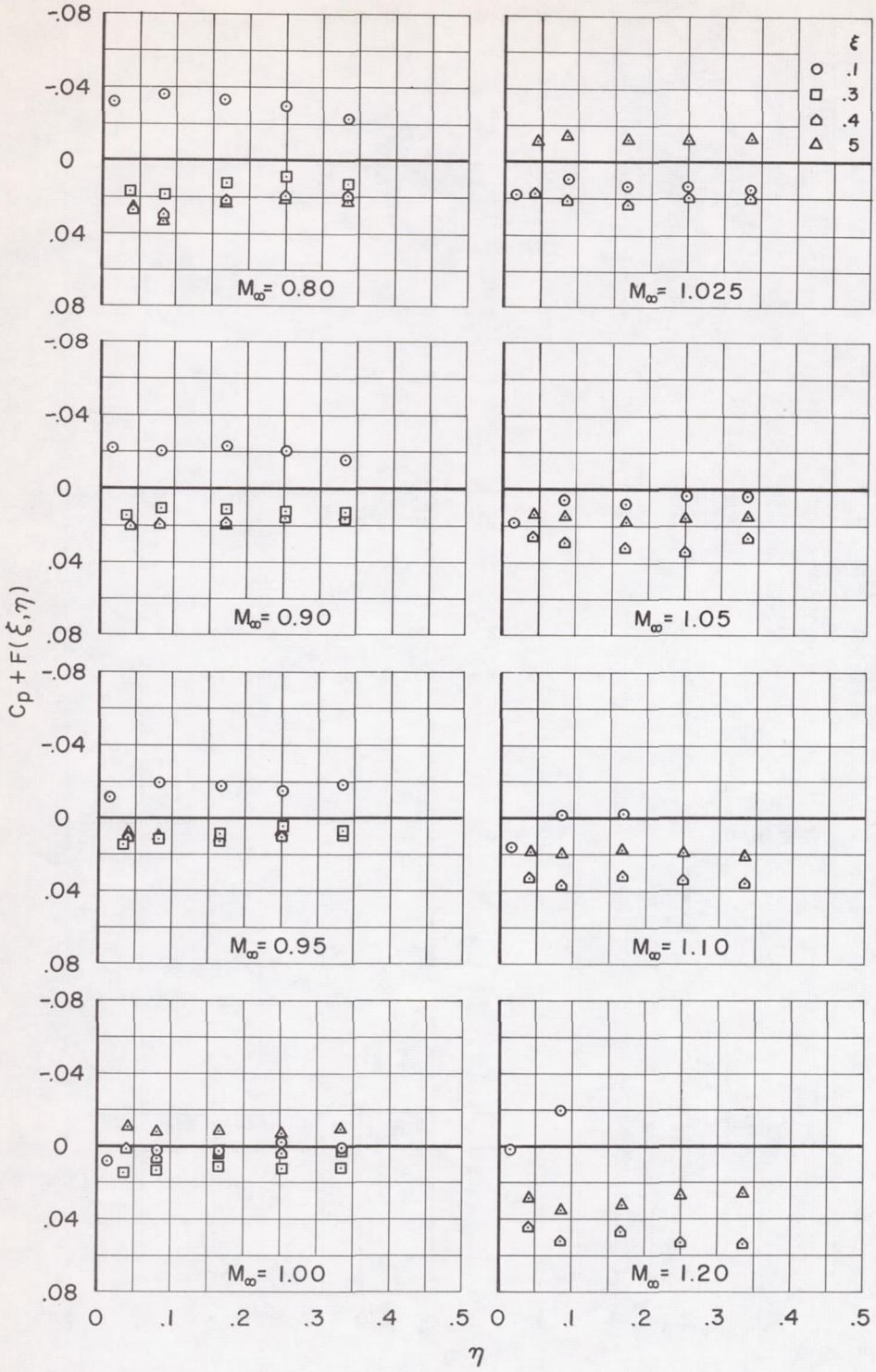

Figure 13.- Variation of $C_p + F(\xi,\eta)$ with radial distance, η, for the body having a fineness ratio of 12.

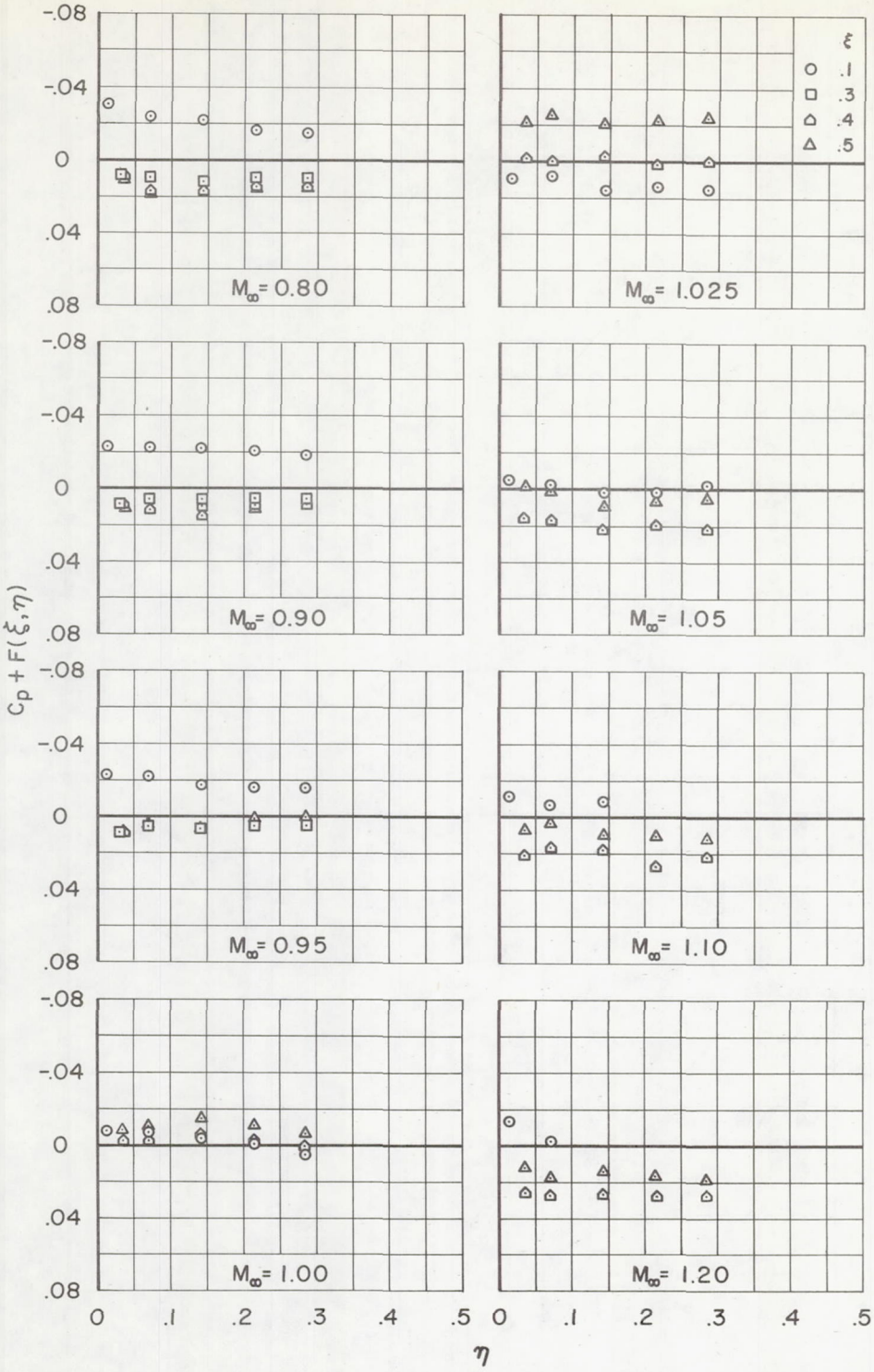

Figure 14.- Variation of $C_p + F(\xi,\eta)$ with radial distance, η, for the body having a fineness ratio of 14.

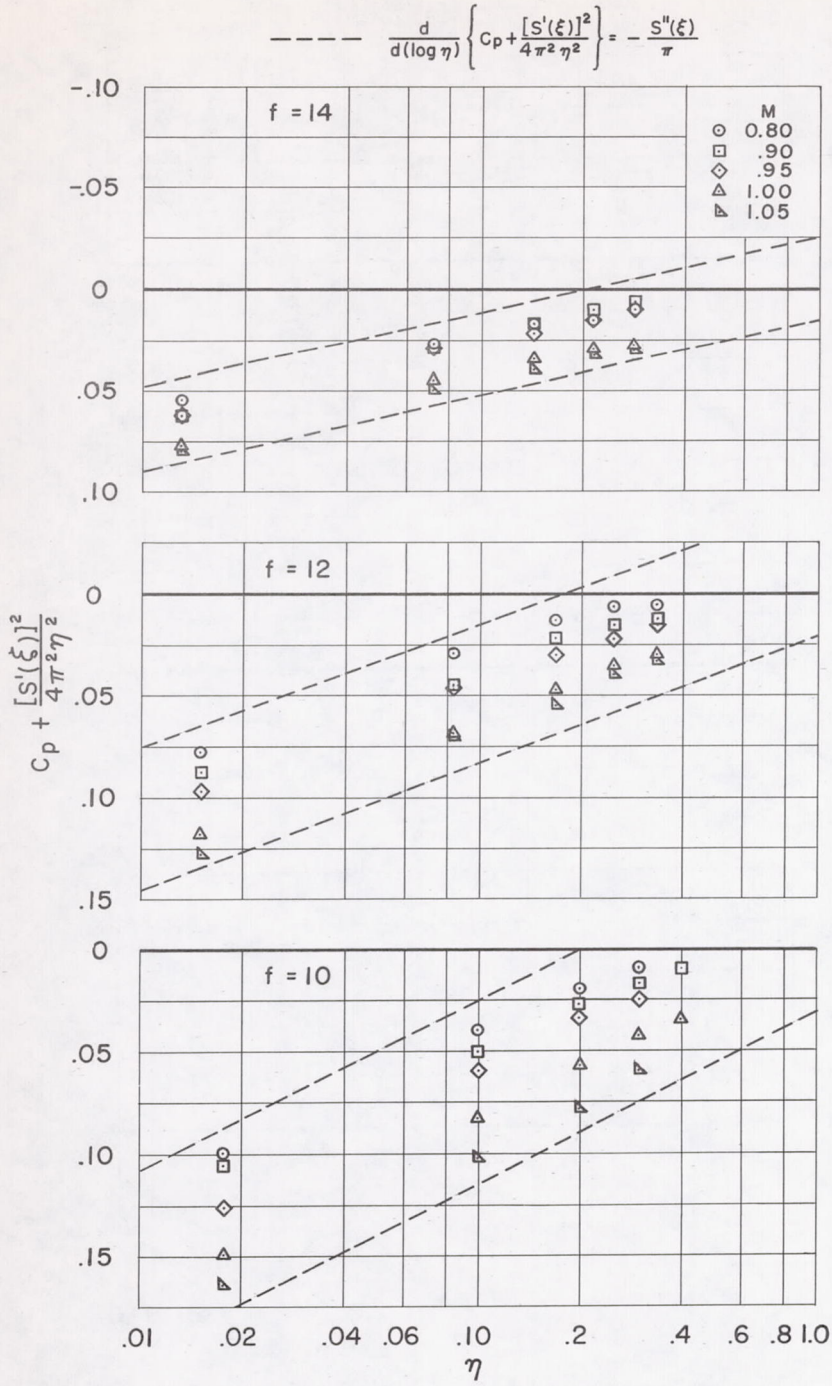

(a) $\xi = 0.10$

Figure 15.- Variation of $C_p + \frac{[S'(\xi)]^2}{4\pi^2\eta^2}$ with radial distance, η, for the bodies having fineness ratios of 10, 12, and 14.

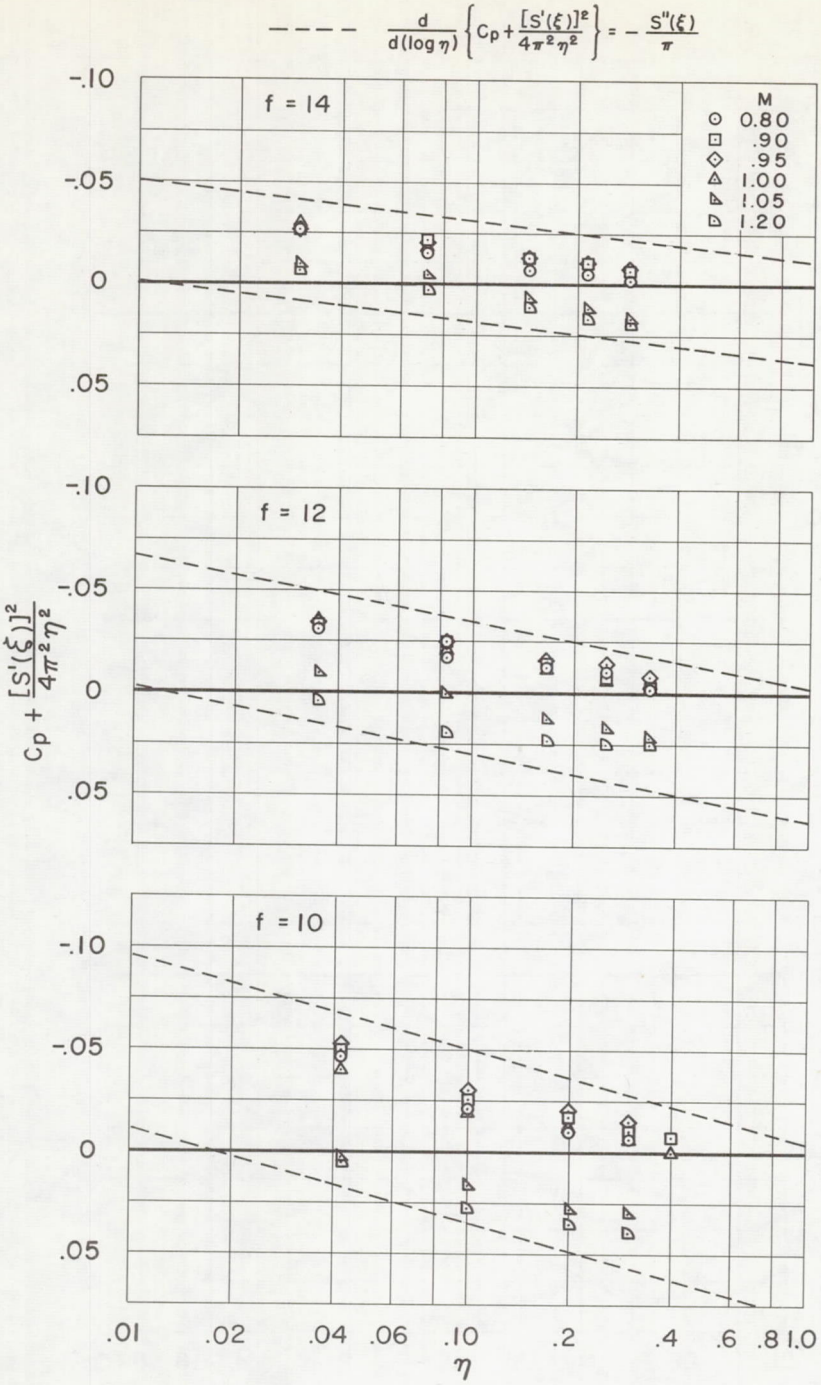

(b) $\xi = 0.30$

Figure 15.- Continued.

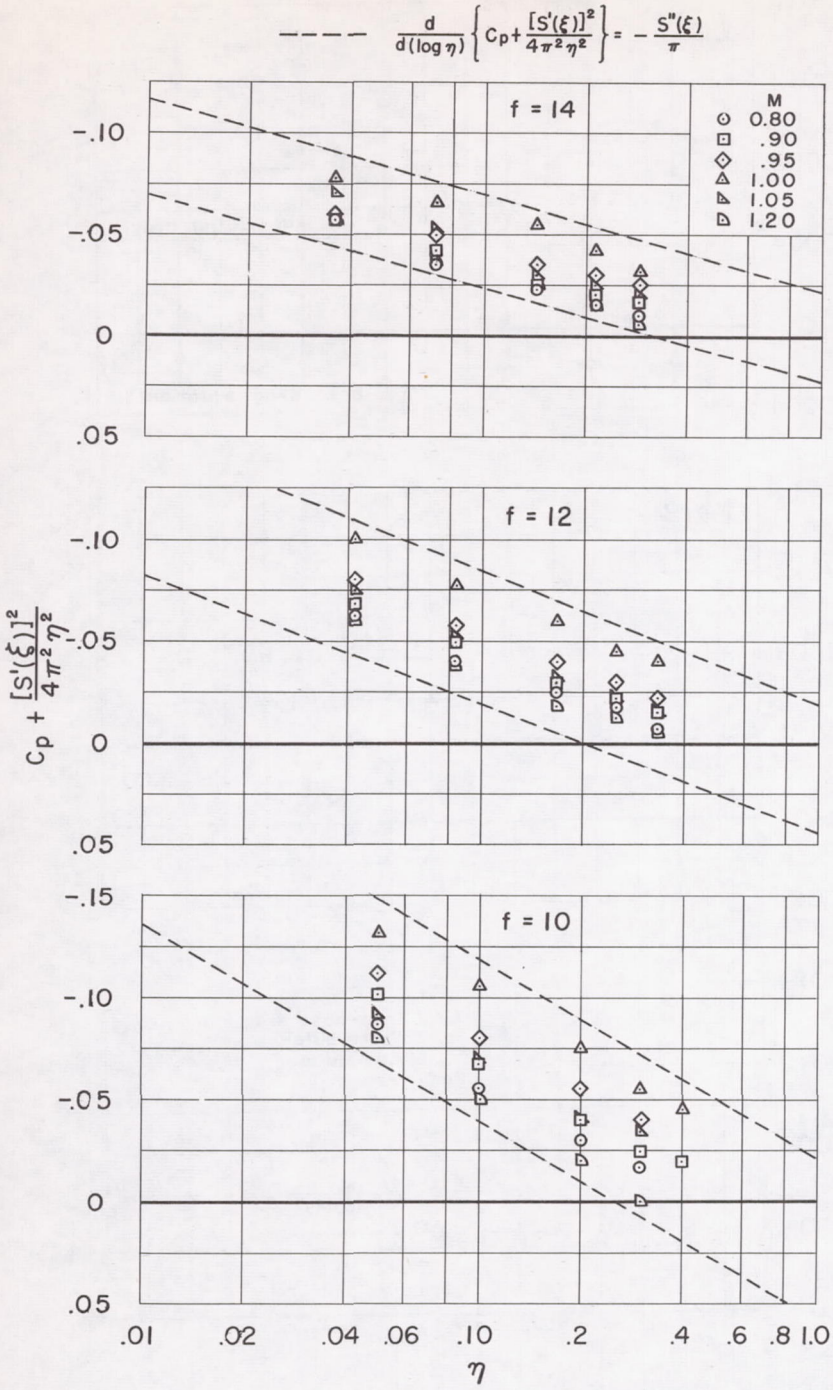

(c) $\xi = 0.50$

Figure 15.- Concluded.

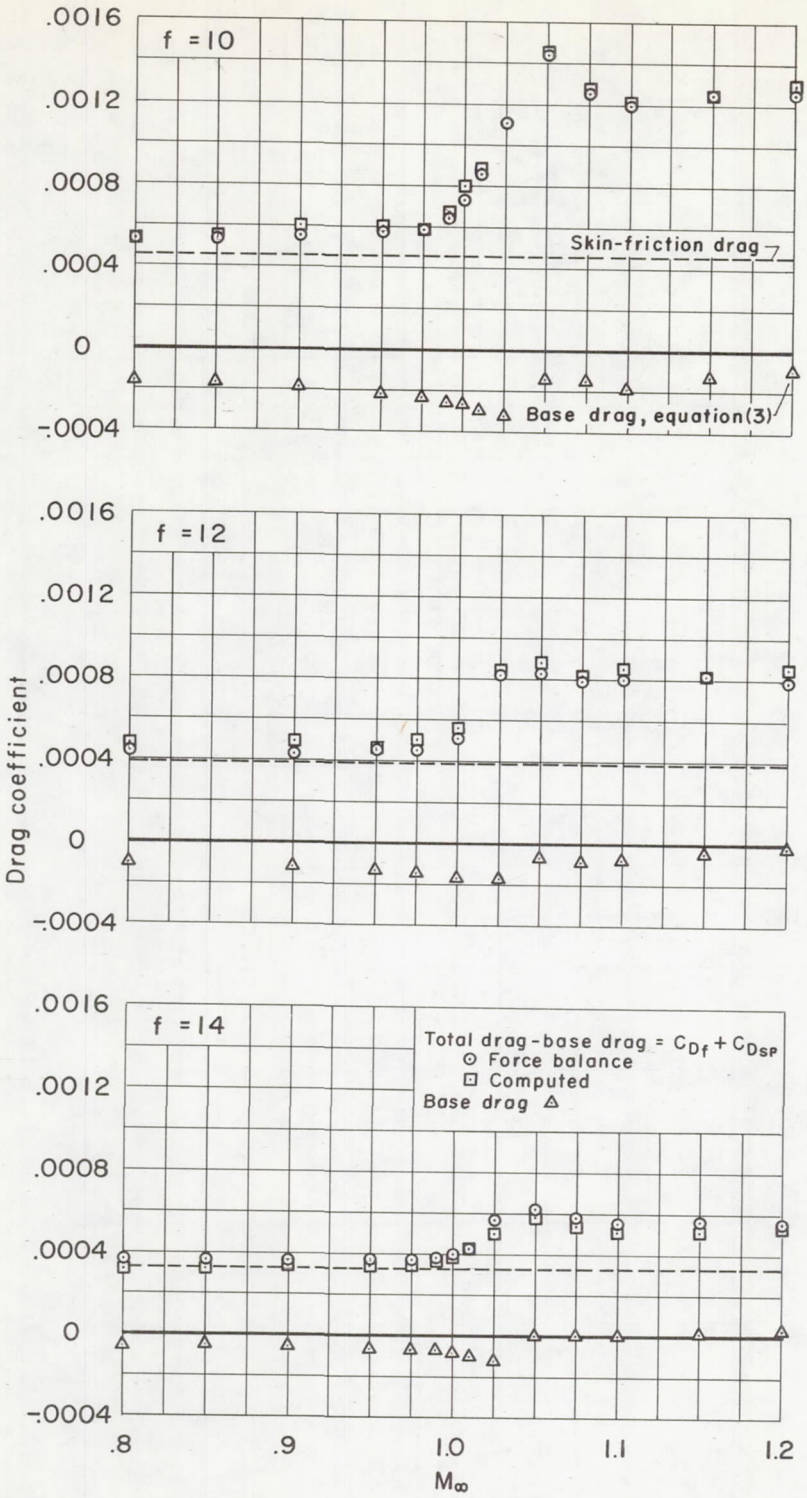

Figure 16.- Variation of drag coefficient with Mach number for the bodies having fineness ratios of 10, 12, and 14.

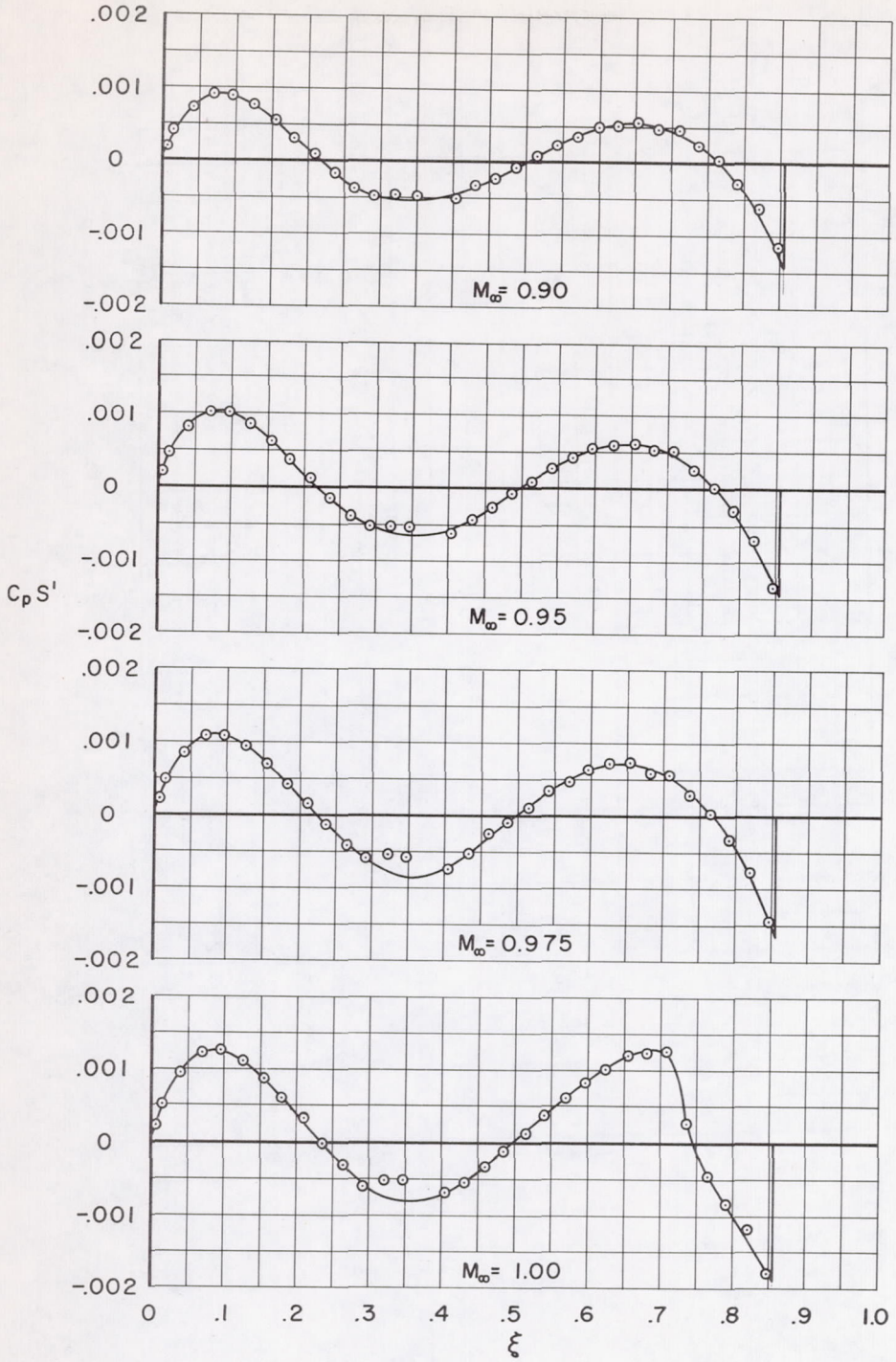

(a) M_∞ = 0.90, 0.95, 0.975, and 1.00

Figure 17.- Typical variations of C_pS' with body station, ξ, for the body having a fineness ratio of 12.

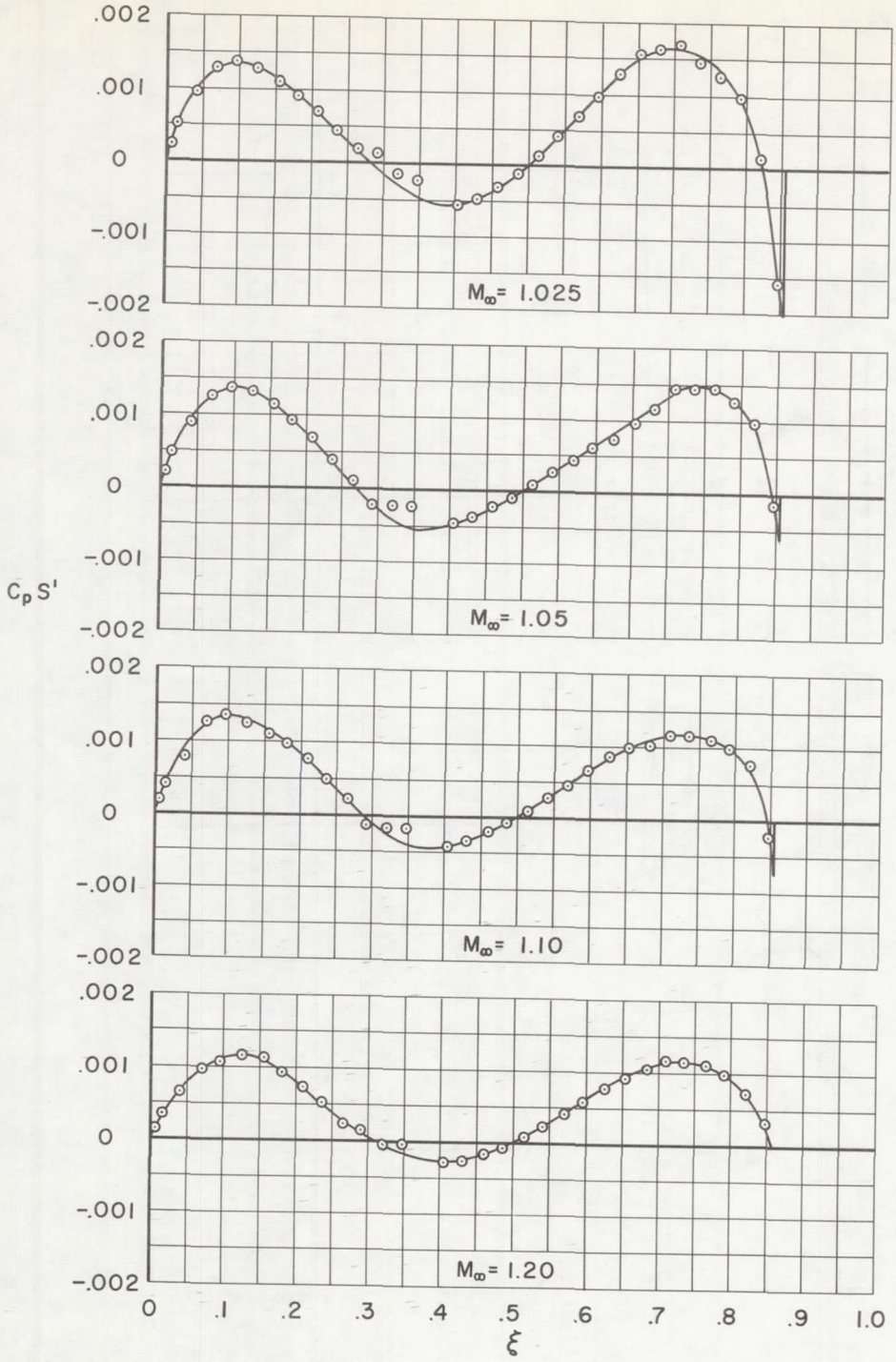

(b) M_∞ = 1.025, 1.05, 1.10, and 1.20

Figure 17.- Concluded.

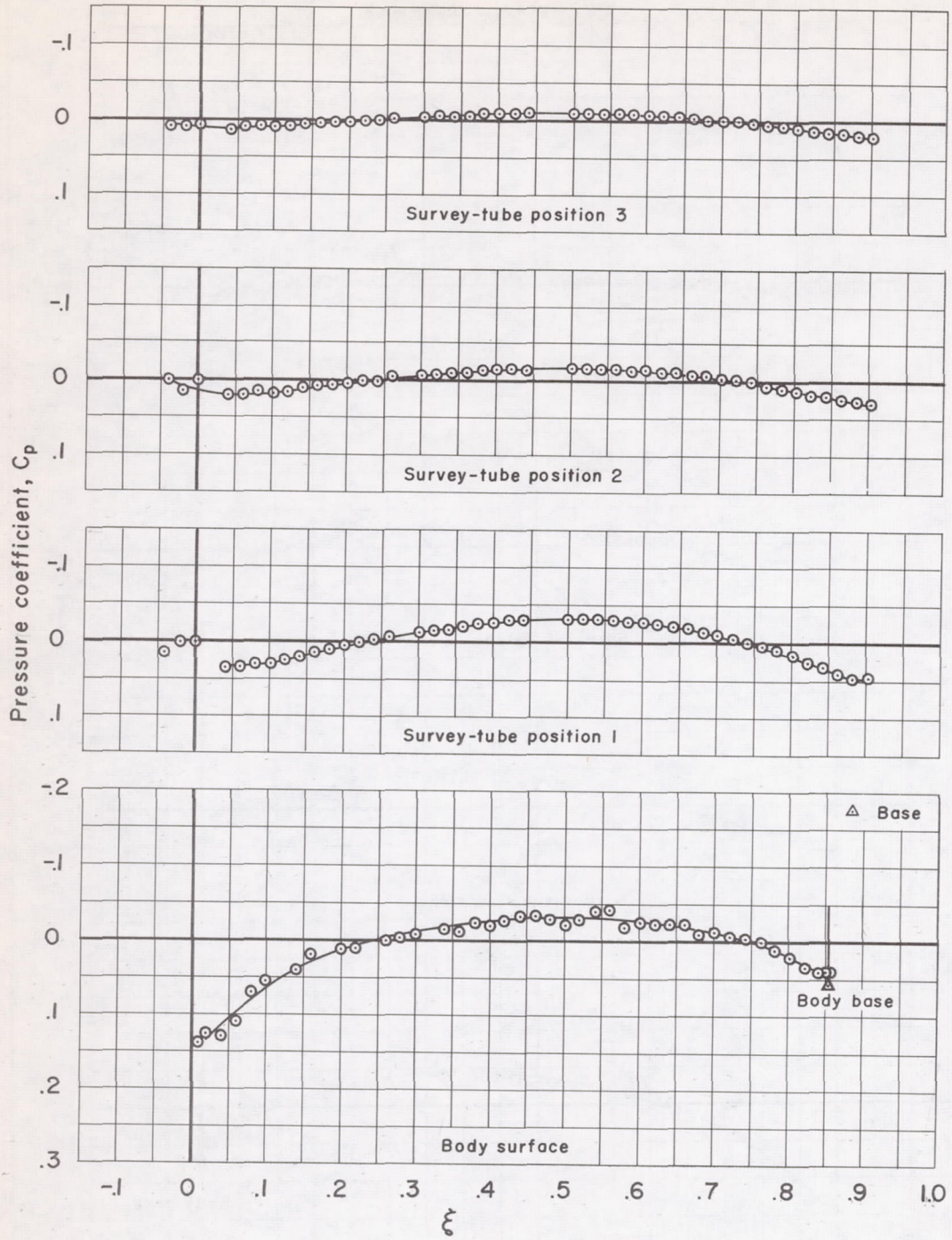

(a) $M_\infty = 0.80$, $f = 14$

Figure 18.- Measured pressure distributions for the large model having a fineness ratio of 14.

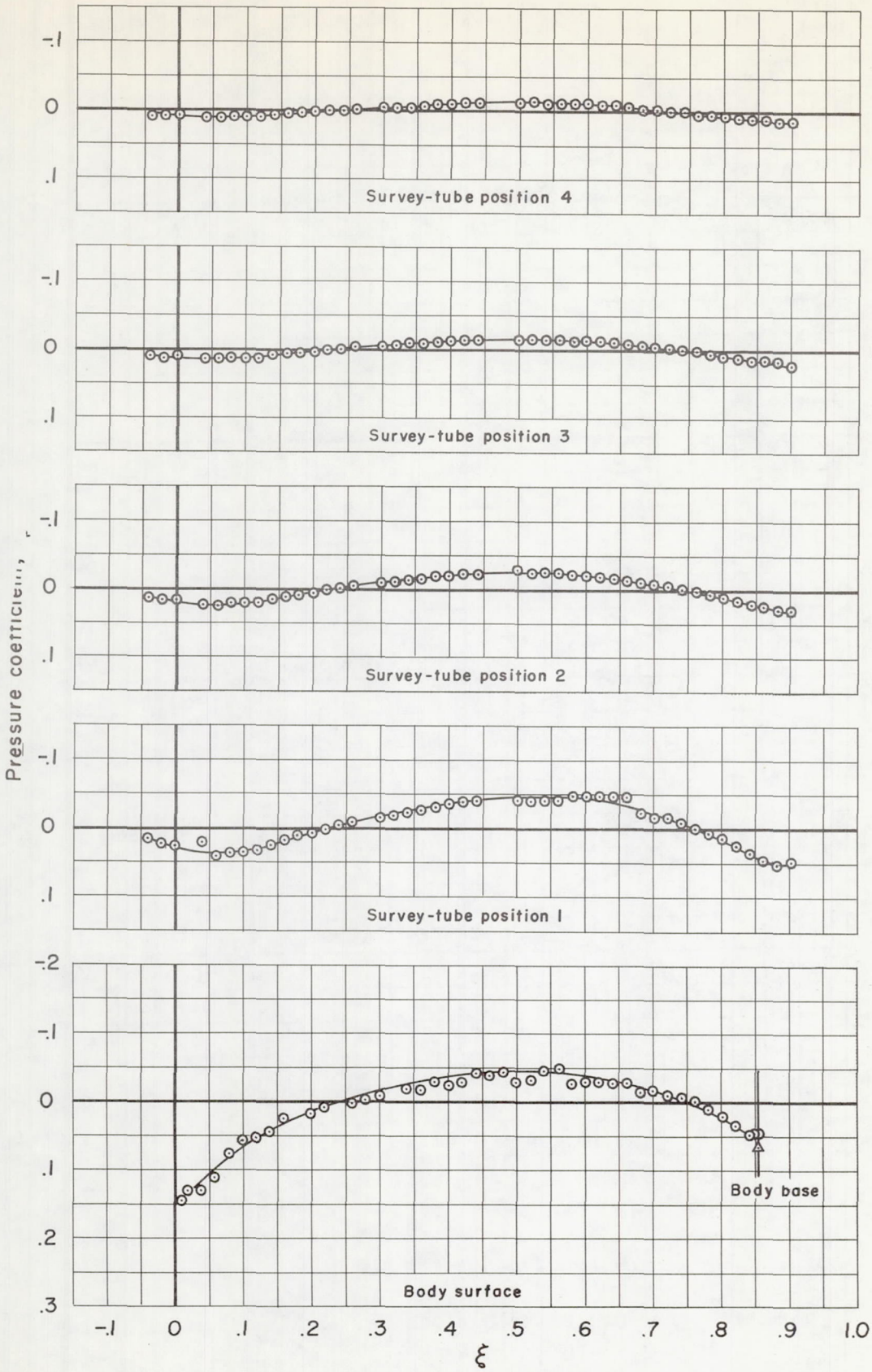

(b) $M_\infty = 0.90$, f = 14

Figure 18.- Continued.

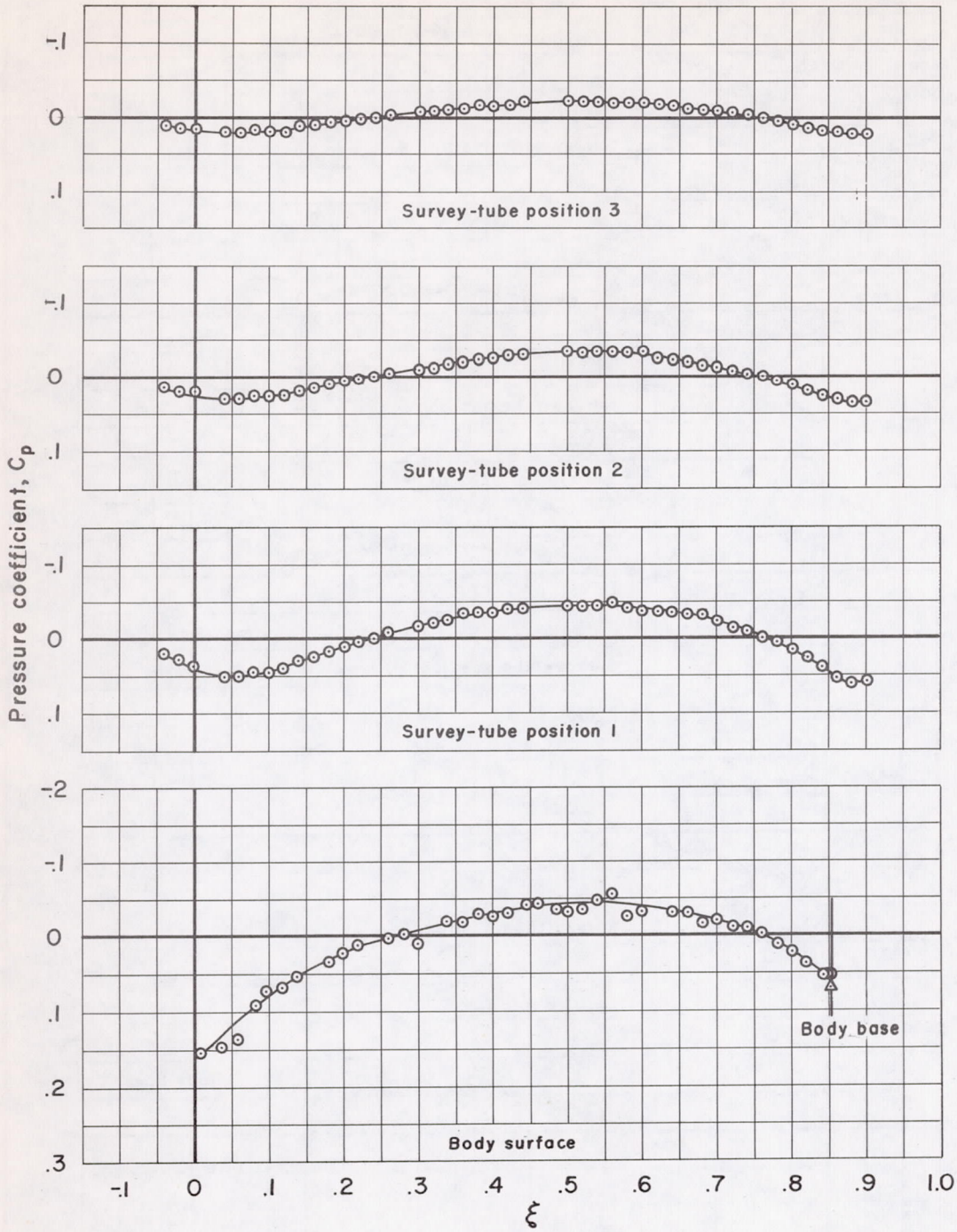

(c) $M_\infty = 0.95$, $f = 14$

Figure 18.- Continued.

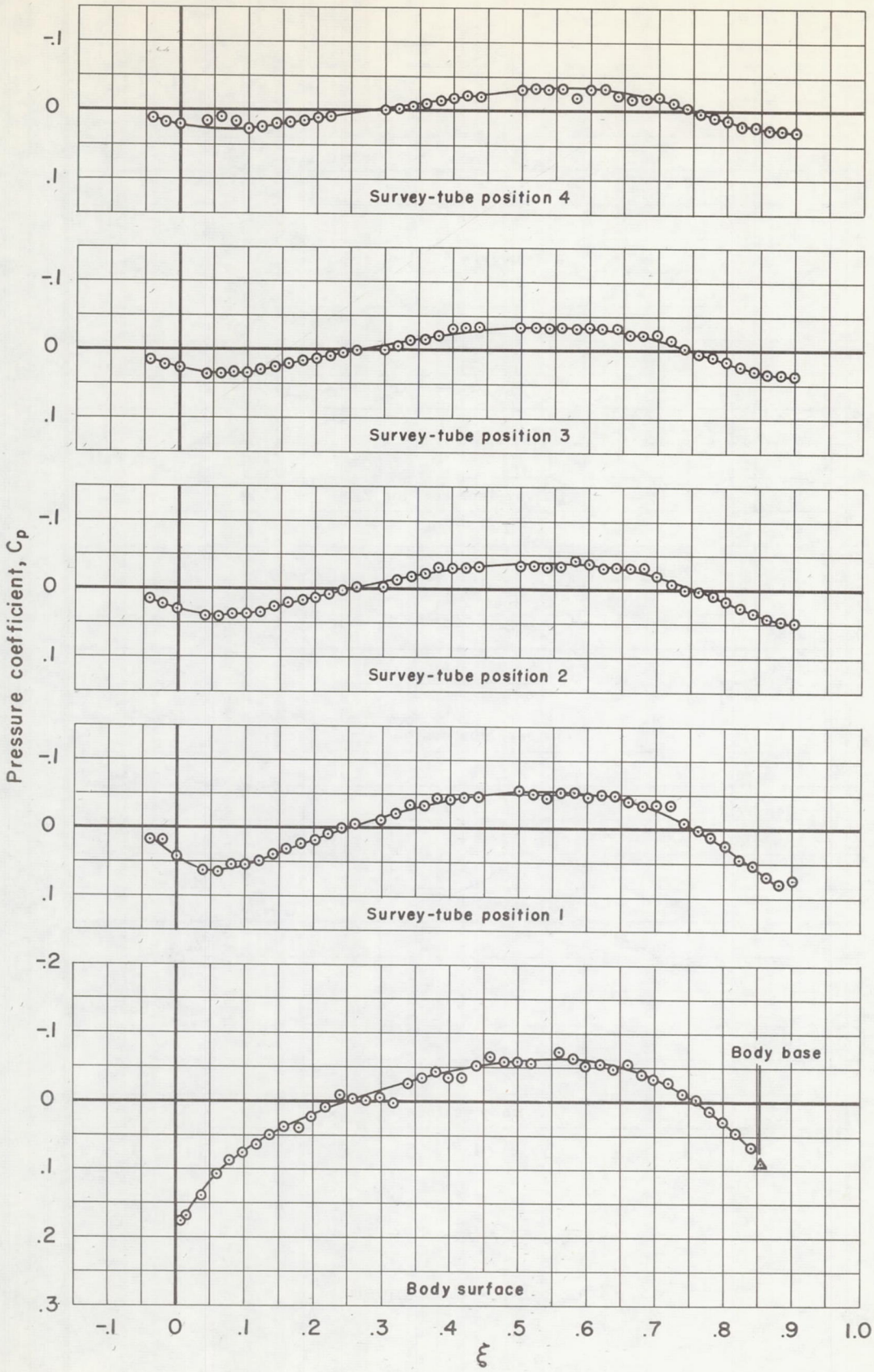

(d) $M_\infty = 1.00$, $f = 14$

Figure 18.- Continued.

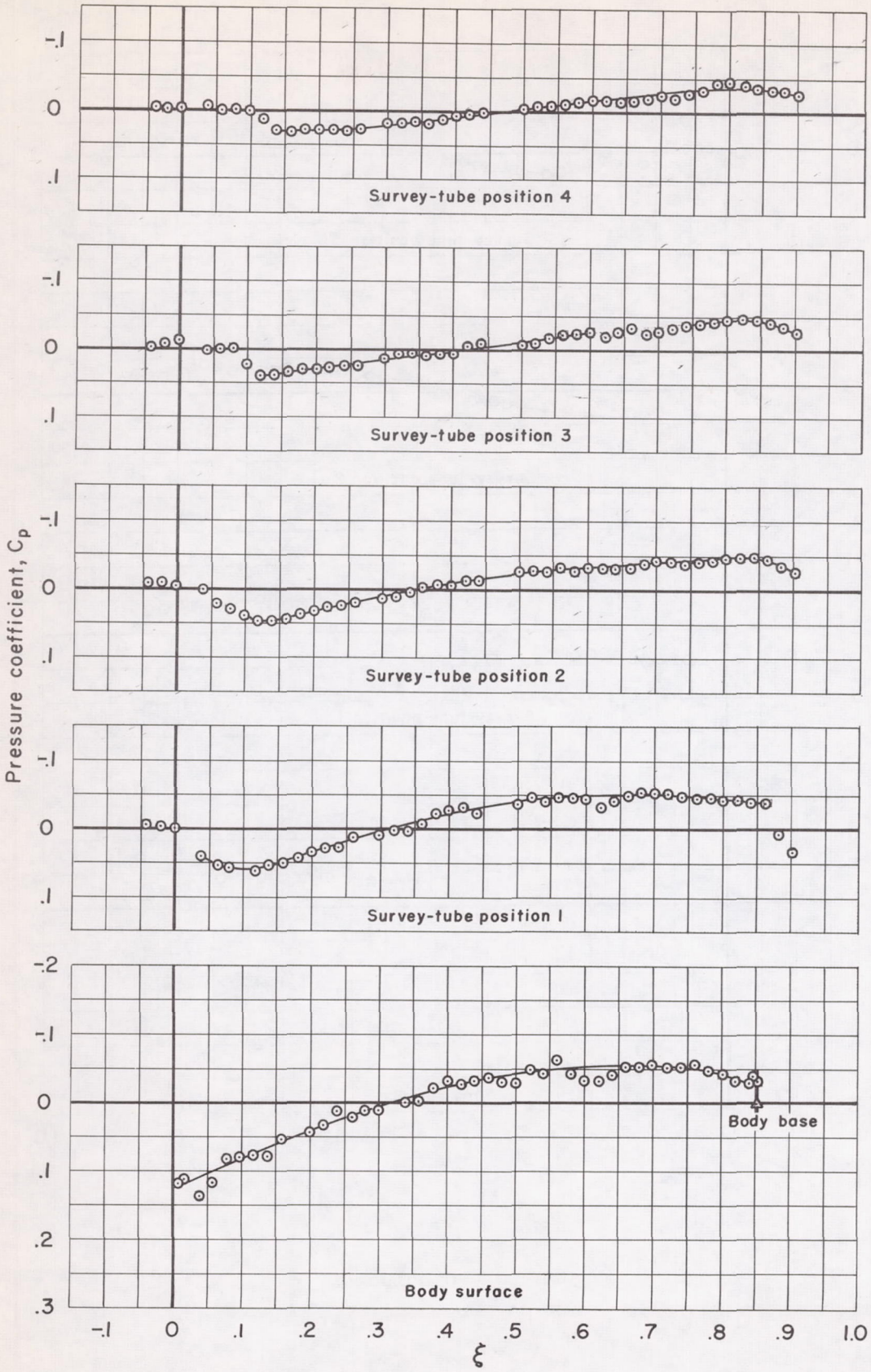

(e) $M_\infty = 1.10$, $f = 14$

Figure 18.- Continued.

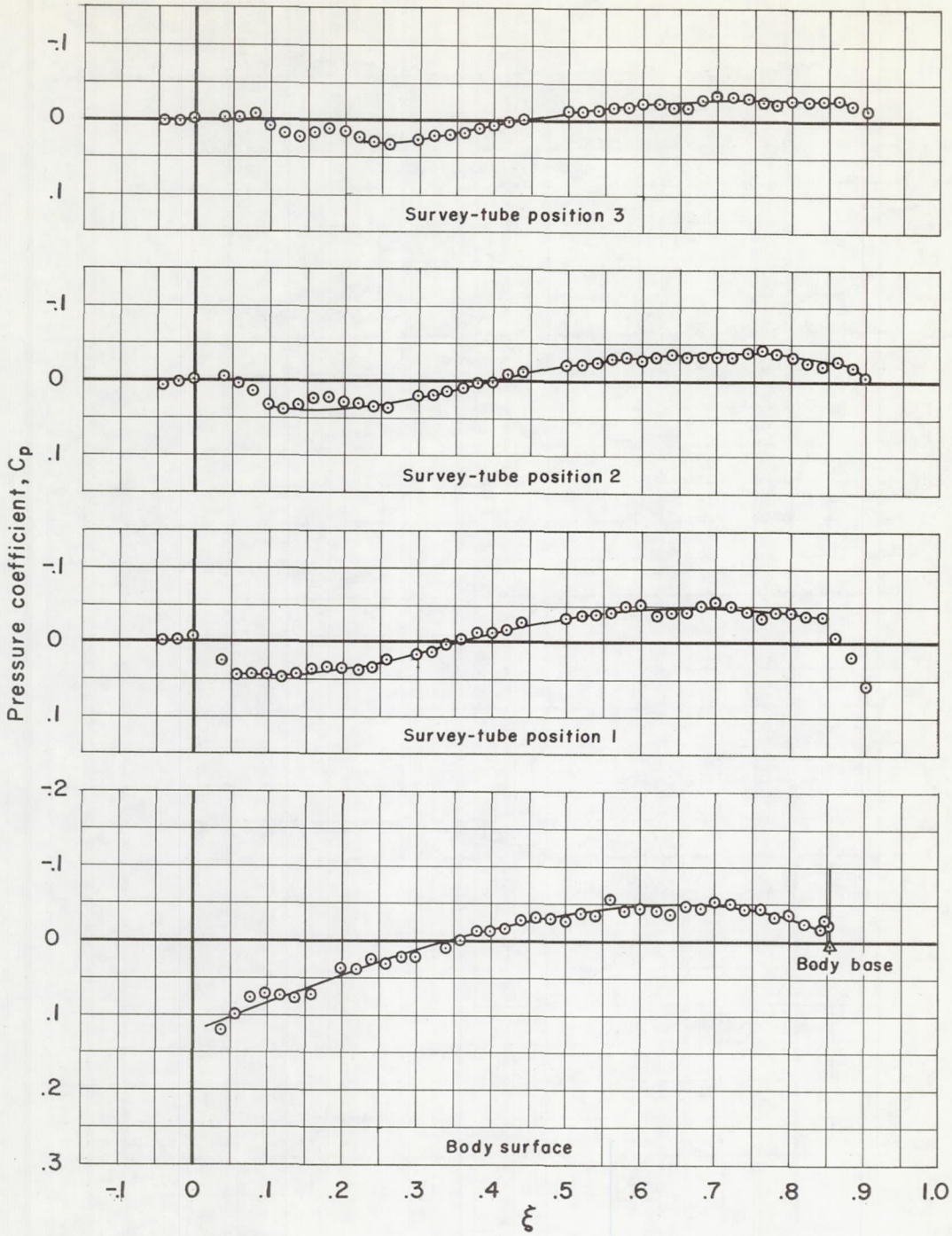

(f) $M_\infty = 1.20$, $f = 14$

Figure 18.- Concluded.